

RICE UNIVERSITY

**Plasmonic properties and applications of metallic  
nanostructures**

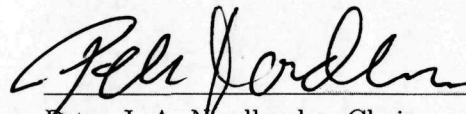
by

**Yurong Zhen**

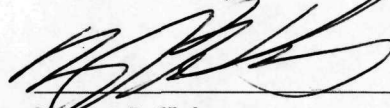
A THESIS SUBMITTED  
IN PARTIAL FULFILLMENT OF THE  
REQUIREMENTS FOR THE DEGREE

**Doctor of Philosophy**

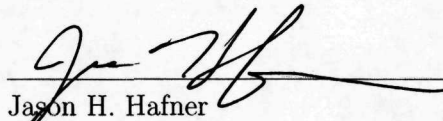
APPROVED, THESIS COMMITTEE:



Peter J. A. Nordlander, Chair  
Professor of Physics and Astronomy



Naomi J. Halas  
Stanley C. Moore Professor of Electrical  
and Computer Engineering



Jason H. Hafner  
Associate Professor of Physics and  
Astronomy

Houston, Texas

March, 2013

## ABSTRACT

Plasmonic properties and applications of metallic nanostructures

by

Yurong Zhen

Plasmonic properties and the related novel applications are studied on various types of metallic nano-structures in one, two, or three dimensions. For 1D nanostructure, the motion of free electrons in a metal-film with nanoscale thickness is confined in its normal dimension and free in the other two. Describing the free-electron motion at metal-dielectric surfaces, surface plasmon polariton (SPP) is an elementary excitation of such motions and is well known. When further perforated with periodic array of holes, periodicity will introduce degeneracy, incur energy-level splitting, and facilitate the coupling between free-space photon and SPP. We applied this concept to achieve a plasmonic perfect absorber. The experimentally observed reflection dip splitting is qualitatively explained by a perturbation theory based on the above concept. If confined in 2D, the nanostructures become nanowires that intrigue a broad range of research interests. We performed various studies on the resonance and propagation of metal nanowires with different materials, cross-sectional shapes and form factors, in passive or active medium, in support of corresponding experimental works. Finite-Difference Time-Domain (FDTD) simulations show that simulated results agrees well with experiments and makes fundamental mode analysis possible. Confined in 3D, the electron motions in a single metal nanoparticle (NP) leads to localized surface plasmon resonance (LSPR) that enables another novel and important application:

plasmon-heating. By exciting the LSPR of a gold particle embedded in liquid, the excited plasmon will decay into heat in the particle and will heat up the surrounding liquid eventually. With sufficient exciting optical intensity, the heat transfer from NP to liquid will undergo an explosive process and make a vapor envelop: nanobubble. We characterized the size, pressure and temperature of the nanobubble by a simple model relying on Mie calculations and continuous medium assumption. A novel effective medium method is also developed to replace the role of Mie calculations. The characterized temperature is in excellent agreement with that by Raman scattering. If fabricated in an ordered cluster, NPs exhibit double-resonance features and the double Fano-resonant structure is demonstrated to most enhance the four-wave mixing efficiency.

# Acknowledgments

First and foremost, thanks to my wife, Ting Li. You are the most important person in the world to me. Without the help from you to take care of the family, I would not have been able to focus on my PhD studies and meet the requirement within four years.

Thanks to my parents and parents-in-law, you have been sacrificing your time and energy a lot in helping my family.

I would like to acknowledge Professor Peter Nordlander for his great support and the role as my advisor, as well as the chair of my committee. His has given me a lot of freedom in research and his support and patience throughout this period have been invaluable.

I would also like to acknowledge Professor Naomi Halas and Professor Jason Hafner, not only for the co-authorship and the role as committee members, but also for their insightful advice during my studies, and the unparalleled research opportunities provided in tight theory-experiment collaboration.

This dissertation would not have been possible without the hard work and support of my other co-authors, as well as the funding agencies. Thank you all.

Parts of this dissertation are based on papers co-authored with my collaborators:

- Chapter 2 is based on "Tunable wide-angle plasmonic perfect absorber at visible frequencies", by Zheyu Fang, Yu-Rong Zhen, Linran Fan, Xing Zhu, and Peter Nordlander, as it appears in [1].
- Section 3.1 is based on "A Tunable Plasmon Resonance in Gold Nanobelts", by Lindsey J. E. Anderson, Courtney M. Payne, Yu-Rong Zhen, Peter Nordlander, and Jason H. Hafner, as it appears in [2].

- Section 3.2 is being prepared for submission for publication by Lindsey J. E. Anderson, Yu-Rong Zhen, Courtney M. Payne, Peter Nordlander, and Jason H. Hafner.
- Section 3.3 is being prepared for submission for publication by Aniruddha Paul, Yu-Rong Zhen, Yi Wang, Younan Xia, Peter Nordlander, and Stephan Link.
- Section 4.1 has been accepted by Nano Letters for publication [3], and was prepared by Zheyu Fang, Yu-Rong Zhen, Oara Neumann, Albert Polman, Javier Garca de Abajo, Peter Nordlander, and Naomi J. Halas.
- Section 4.2 is being prepared for submission for publication by Yu-Rong Zhen, Zheyu Fang, Javier Garca de Abajo, Naomi Halas and Peter Nordlander.
- Chapter 5 has been submitted to Proc. Nat. Acad. Sci. for review, and was prepared by Yu Zhang, Fangfang Wen, Yu-Rong Zhen, Peter Nordlander, and Naomi J. Halas

Special thanks to my group members and former group members, including but not limited to, Kui Bao, Yang Li, Ke Zhao, Nicolas Large, Jorge Zuloaga, Heidar Sobhani, Vikram Kulkarni, Yumin Wang, Tamer Ali, Feng Hao, Fei Le, Yanpeng Wu, Lifei Liu, Yang Cao, Chizuko Dutta, Manvir Singh, etc.

Special thanks to the members in Halas group, Hafner group and Link group who have shared ideas and exchanged opinions together.

Special thanks to my friends both inside and outside Rice, who gave me their unwavering support (and, in some cases, the use of their couch).

Lastly, special thanks to my children, Xinyi Zhen and Lijia Zhen. I am profoundly blessed to have all of you in my life.

# Contents

Abstract	ii
Acknowledgments	iv
List of Figures	ix
<b>1 Introduction</b>	<b>1</b>
1.1 Planar nanostructure . . . . .	2
1.2 Nanowire . . . . .	2
1.3 Nanoparticle . . . . .	5
1.3.1 Single nanoparticle and nanobubble . . . . .	7
1.3.2 Nanocluster . . . . .	10
1.4 Outline . . . . .	10
<b>2 Nanofilm based perfect absorber</b>	<b>15</b>
2.1 Motivation . . . . .	15
2.2 Experimental measurements . . . . .	17
2.3 Theoretical description . . . . .	20
2.3.1 Coupling mechanism . . . . .	20
2.3.2 A perturbative approach . . . . .	21
2.4 Conclusion . . . . .	29
<b>3 Plasmonic properties of nanowires</b>	<b>31</b>
3.1 Surface plasmon resonance of nanobelt . . . . .	31
3.1.1 Introduction . . . . .	31
3.1.2 Sharp resonance . . . . .	33

3.1.3	Simulation . . . . .	34
3.1.4	Discussion . . . . .	36
3.1.5	Conclusion . . . . .	40
3.2	Propagation and electromagnetic confinement in nanobelt . . . . .	40
3.2.1	Introduction . . . . .	40
3.2.2	Propagation length measurements . . . . .	43
3.2.3	Simulated properties of propagating modes . . . . .	47
3.2.4	Conclusion . . . . .	53
3.3	Stimulated emission of SPP in nanowire: dye-assisted propagation length enhancement . . . . .	54
3.3.1	Introduction . . . . .	54
3.3.2	Experiment . . . . .	56
3.3.3	Simulation . . . . .	60
3.3.4	Conclusion . . . . .	63
<b>4</b>	<b>Plasmon-heated bubble generation</b>	<b>64</b>
4.1	Experimental characterization . . . . .	64
4.1.1	Motivation . . . . .	64
4.1.2	Experimental evidences of formed nanobubble . . . . .	67
4.1.3	Theoretical analysis . . . . .	73
4.1.4	From nanobubble to microbubble . . . . .	77
4.2	Local field weighted effective medium method . . . . .	81
4.2.1	Introduction . . . . .	81
4.2.2	Results and discussion . . . . .	83
4.2.3	Benchmark test . . . . .	90
4.2.4	Methods . . . . .	93
4.3	Determination of bubble pressure and temperature . . . . .	96
4.4	Analysis of nanosphere surface temperature . . . . .	97

4.5	Conclusion . . . . .	99
<b>5</b>	<b>Four-wave mixing in nanocluster</b>	<b>101</b>
5.1	Introduction . . . . .	101
5.2	Double Fano-resonance structure . . . . .	104
5.3	FWM measurements . . . . .	105
5.4	FDTD-assisted modelling . . . . .	108
5.5	Control experiments . . . . .	110
5.6	Conclusion . . . . .	111
<b>6</b>	<b>Conclusions</b>	<b>113</b>
	<b>Bibliography</b>	<b>117</b>



## List of Figures

2.1	Schematic of the experimental configuration of the perfect absorber . . .	18
2.2	Experimental reflectance for varied hole radius . . . . .	19
2.3	Coupling mechanism from incident photons into the SPP and the SPP's lateral profile . . . . .	21
2.4	Dispersion relation diagram of the hybridized surface plasmon polariton in the unperturbed heterostructure . . . . .	23
2.5	Three unperturbed eigenstates and the radius-dependent peak splitting	28
3.1	Dark field micrographs and corresponding single nanobelt spectra . . .	33
3.2	Gold nanobelt simulation geometry, spectra and charge distributions for TE illumination . . . . .	35
3.3	Calculated charge distribution of the zig-zag mode by TM illumination.	37
3.4	The dependence of the plasmon resonance peak on cross-sectional aspect ratio . . . . .	38
3.5	Gold nanobelts deposited on a substrate and imaged by dark-field optical microscopy and by scanning electron microscopy . . . . .	44
3.6	Two gold nanobelts imaged with epi-bright field illumination and focused illumination to display propagation . . . . .	45
3.7	Measured plasmon propagation lengths of gold nanobelts and silver nanowires . . . . .	46
3.8	Dark-field image and simulated properties of propagating modes . . .	49

3.9	Experimentally verified cross-over of the propagating mode intensities with parallel and perpendicular polarization . . . . .	50
3.10	Cross-sections of normalized field and heat intensity in a 125 × 40 nm gold nanobelt . . . . .	51
3.11	Schematic description of the gain experiment . . . . .	58
3.12	A representative gain experiment . . . . .	59
3.13	FDTD simulation of SPP gain for a silver NW lying on top of a dielectric/gain layer . . . . .	62
4.1	Light-induced generation of a nanobubble at a single nanoparticle surface . . . . .	68
4.2	Temperature at the Au nanoparticle surface during the steam generation process . . . . .	71
4.3	Nanobubble theoretical modeling . . . . .	75
4.4	Coalescence of nanobubbles into micron-sized bubbles . . . . .	78
4.5	Experimental optical spectra for a gold nanosphere (NS) and the effect of water temperature . . . . .	85
4.6	Schematics and simulated scattered electric field intensity ( $ E_{sc} ^2$ ) of a plasmon-heated nanobubble around a gold nanosphere and its ambience. . . . .	87
4.7	Calculated bubble radius as a function of peak shift ratio with different methods . . . . .	91
5.1	FWM configuration and characterization of the double Fano resonant plasmonic nanocluster . . . . .	103
5.2	FWM Experiments by individual nanoclusters . . . . .	106
5.3	FDTD calculated near-field maps of the nanocluster . . . . .	109
5.4	FWM control experiments . . . . .	112

# Chapter 1

## Introduction

Plasmon, an elementary excitation of free-electron oscillation in metals, has been a hot research topic [4, 5, 6, 7, 8] over the past decades and has attracted huge interest in plasmon-related novel applications, such as biomedical treatment [9, 10, 11, 12, 13], perfect transmitter [5, 6, 14, 15, 16] and absorber [17, 18, 19, 20, 21, 22, 23, 24, 25, 26, 27, 1], bubble-generation [10, 28, 29, 30, 31, 32], metallic nanowires [2, 33, 34, 35, 36, 37, 38, 39, 40, 41], hot-electron harvesting [8, 42, 43, 44], etc. Basically, three classes of metallic nanostructure can be fabricated. The first one consists of film-based planar metallic structures embedded in dielectric materials. In such structures, the electron is confined in the normal dimension of the film. The second refers to a nanowire (NW) where the electron is confined in two dimensions and the third to nanoparticle(s) (NPs) in which electron is confined in the all three spacial dimensions and encompassed by the metal-dielectric surface in all possible directions. For simplicity, any nanostructure discussed in this thesis are metallic, other than explicitly stated.

## 1.1 Planar nanostructure

The excitation of electron oscillations at the planar metal-dielectric surface, are dictated by Maxwell equations which are the root equations for generic electromagnetic (EM) problems, as well as the material properties of the metal and dielectrics. This type of oscillation at the surface of a semi-finite metal-dielectric system is characterized by surface plasmon polariton (SPP) [45, 46, 47]. Further, the plasmonic properties of a metal film with finite thickness, originating from the interaction between the SPPs on the two surfaces, are also well known [45, 46, 47]. However, because the dispersion relations for SPPs are below the light-line (the reader is encouraged to refer to Ref. [47] for a recent review of the progress of SPPs), the conservation of momentum has limited the direct coupling between a free space radiation and a SPP. Compared with smooth planar metal-dielectric surface, a grating or perforation on the film introduces discrete translational symmetry which facilitates the coupling between free-photon and the SPP through lattice momentum addition [6]. Hence, the grating or periodic perforation has allowed for quite a lot new findings and applications based on the planar metallic nanostructures, for example, extraordinary unity transmission [5], perfect absorption [17, 18, 19, 20, 21, 22, 23, 24, 25, 26, 27, 1], etc.

## 1.2 Nanowire

For a metallic nanowire, a 2D confined nanostructure, the planar metal-dielectric surface no longer exists, so does the planar SPP which has a simple analytical description

[45, 46, 47]. For some special cases with rotational symmetry, for instances, nanowires with cylindrical shapes, one can still derive analytical solution to the Maxwell equations because the rotational symmetry explicitly allows a simple description of the boundary conditions on the metal-dielectric surface. On the other hand, when applying the transform optics on metallic nanowires with a limited number of cross-sectional shapes [48, 49, 50, 51], one can also obtain the analytical descriptions for these wire structures. However, generally speaking, there is no analytical solutions for nanowire with arbitrary cross-sectional shape other than some special cases. Instead, we must seek help from numerical simulations.

In nature, a nanowire is a waveguide that is able to transport energy and signal. One of the advantages of using metallic nanowire as a waveguide is that the guiding mechanism is achieved by the excitation of the propagating wire SPP mode, a surface wave propagating along the wire axis, just similar to the planar SPP. The excited surface wave due to collective electron oscillation allows the transported energy to be confined in a narrow cross-sectional area. Therefore, a metallic nanowire is a promising building block for optical signal processing and energy transporting at nanoscale. There has been a lot of studies on the plasmonic properties of nanowire and the derivative novel applications. For example, controllable optical router has been accomplished by using branched silver nanowires [33].

In the sense of energy transportation, one always favors a small cross-sectional form factor and a propagation as far as possible. Unfortunately, the non-radiation

(intrinsic) damping of the metal, mainly due to electron-electron scattering, dictates that an infinite propagation on a metallic NW is impossible. Because of damping (either radiation or non-radiation), the excited wire SPP experiences an exponential decay along the wire axis. And a propagation length (PL), defined as the length at which the magnitude of axially transported energy drops to  $1/e$ , is used to characterize how far a metallic NW can transport energy. Experimental and numerical techniques have been developed to measure and calculate the PLs of various metallic NWs [34, 35, 36, 37, 38, 39, 40, 41] with varied operating wavelengths, composed materials, geometric shapes, etc.

Among different shapes of metallic NWs, nanobelt is a type of NW with rectangular cross section and both rectangular dimensions on the order of nanometers. A nanobelt has its own advantages over other shapes. The most important one, as is expected, is that the rectangular cross section can serve as a flat platform on top of which other nanoparticles (dielectric or metallic, passive or active) can be physically supported, thus making the nanobelt significantly ideal as a base for further research on plasmon-based optical signal processing, amplification, and transportation. Although there has been pioneering investigations on rectangular-cross-section NWs before, especially by Berini et al. [52, 53, 54, 55, 56], the widths of the reported NWs are often at the order of microns, limiting subwavelength/nanoscale applications. In contrast to Berini's structures, often referred to nanostripes, the recently achieved experimental fabrication of nanobelts [2] has removed such limitations. Furthermore,

the realization of single-crystalline nanobelt and smooth crystallographic plane as the edges of the nanobelt [2] has minimized the electron scattering at mis-matched crystal surfaces, thus indicating a less damped material and a longer PL, which is favored. As a result, basic understanding of the excited wire SPPs is highly desired, especially from numerical simulations, from which one can not only justify experimental findings but also conduct mode analysis and appropriate predictions.

To make the NWs applicable, one favors PL as large as possible. In this sense, an active medium can be introduced to compensate the loss of propagating SPP [57, 58, 59, 60, 61, 62, 63, 64, 65, 66, 67, 68, 69, 70, 71, 72] or even to allow a net gain during the propagation in a gold nanostripe [73]. However, the gold nanostripe reported in Ref. [73] has a width of 1  $\mu\text{m}$  which is not competitive enough for making a nano-width device, especially for the case of sub-wavelength dimension for visible-regime operating wavelength. Therefore, the realization of loss compensation or even net gain in a NW by using active (gain) medium is still in great need.

### 1.3 Nanoparticle

As for nanoparticle(s), the electron is localized and confined by the physical boundaries of metal-dielectric interfaces. Under proper excitation condition (either by optical incidence or electron incidence), surface plasmon can be excited at metal-dielectric interfaces and will experience resonance under resonant frequency. And as a result of the 3D confinement, there is no allowed propagating direction of such excited surface

plasmon. Therefore, the literature has assigned a term "localized surface plasmon resonance (LSPR)" to define such a phenomenon. The simplest example of LSPR is a dipolar resonance of a nanosphere, for instance a gold nanosphere with radius 50 nm.

Experimentally, LSPR is often characterized by an optical spectroscopy. When a light beam is incident on an investigated object, the light will be scattered by the object. If the object is absorptive (true for most metals), the incident light will also be absorbed by the object. Scattering or absorption cross sections are then used to quantify the abilities of the object to scatter or absorb light, respectively. The sum of scattering and absorption cross section is called the "extinction" cross section, which measures the object's ability to make light "extinct" from the forward-propagating incidence. The product of a cross section for a given term (scattering, absorption, extinction) and the incident intensity, is a power quantity for the corresponding term, carrying a unit of Watt.

In theory, just analogous to 2D nanowire, the full vectorial electromagnetic scattering and absorption problem can only be analytically solved for single nanoparticle with a few geometric shapes. For example, the scattering and absorption of a particle with spherical symmetry (nanosphere [74, 75, 76], spherical nanoshell [76, 77], multilayered nanomatryushkas [78, 79]) has been perfectly and analytically solved by Mie calculation. For a single nanoparticle with irregular shape or a more-than-one nanoparticle group, which we refer to nanoparticle cluster in this thesis thereafter, one



usually has to seek for numerical simulations. There are quite a few numerical simulation techniques available for full retarded electromagnetic calculation. To name a few, they are Finite Difference Time Domain (FDTD), Finite Element Method (FEM), Boundary Element Method (BEM), Discrete Dipole Approximation (DDA).

For a nanoparticle cluster formed by varying number of nanoparticles, there is in principle no available analytical solution to the EM scattering problem. Numerical techniques are expected in simulating the experiments and calculating the desired quantities accordingly. There have been intensive studies on some typical nanocluster: dimer [80, 81, 82, 83, 84, 85, 86], trimer [87, 88], quadrumer [87, 89], heptamer [90, 91], etc. For the heptamer structure, Fano-resonance has been observed [90, 91] in the optical scattering.

The spectral position and width of the LSPR strongly depends on a lot of factors. For a single nanoparticle, these factors are typically size, shape, material, ambient dielectric constant, presence of the substrate, roughness of the surface, etc. For a nanoparticle cluster, the interparticle distance and the array in which the individual particles are placed become the most important ones.

### **1.3.1 Single nanoparticle and nanobubble**

A lot of nanoparticle-based plasmonic applications has emerged in recent years. Besides the extensively studied nanosphere [92, 93, 94, 95, 96, 97, 98, 99], nanodisk [100, 101, 102, 103, 104, 105, 106, 107, 108] and nanoshell [76, 77, 78, 79], a lot of

nanoparticles with other shapes have also been fabricated and investigated for their unique plasmonic properties, such as nanostar [109, 110, 111, 112, 113], nanorice [114, 115, 116], nanocup [117, 118, 119, 120], nanowedge [121], etc.

The nanoparticle-based applications can be simply identified in thermal and optical categories. As it means, thermal application employ the thermal properties resulted from the plasmonic modes excited in the NP. While the incident light is absorbed, a majority portion of the absorbed energy is transferred into heat, while the rest into other channels such as electron-hole pair, phonon coupling.

When heat is generated, the temperature of the nanoparticle will be increased such that some electrons near the Fermi surface will gain additional kinetic energy that big enough to release those electrons from the metal surface. The escaped electron due to plasmon heating, called hot-electron, is then considered a controllable electron source that can inject electrons into other materials or structures, leading to a lot of promising electron-participated applications, for instances, photo-detector [8, 43], graphene- doping-induced optical and transistor [42], accelerated chemical reaction [44], etc.

Being the ground stone of hot-electron based applications, plasmon heating itself is a large research area of novel applications. At resonance, the nanoparticle has maximum absorption ability and thus becomes a nanoscale heat source which has been applied in various disciplines. One example is cancer treatment. By attaching nanoparticles to tumor cells and exciting the LSPR by proper illumination, one can

heat up the nanoparticles thus kill the tumor cell. Such a practice has been proved a breakthrough in cancer therapy [122, 9, 11, 12, 13]. Another example is bubble generation. When embedded in liquid and excited under sufficient incident intensity, the plasmon-induced heating power is so high that the surrounding liquid can quickly vaporize and experience an explosive process. After the initial explosion, a bubble can be formed once the vapor pressure is balanced by the curvature-induced surface tension at liquid-vapor surface in addition to the internal liquid pressure. This type of phenomena has been widely observed in experiments where pulsed laser is used to excite the LSPR of the nanoparticle. Recently, a macroscopic experiment further indicated bubbles can be generated when nanoparticles are immersed in water and under focused solar illumination [32], showing an attractive potential of using nanoparticles for solar energy harvesting which has been a hot research area [25, 123, 124, 23], as well as massive and highly efficient water-steam production. The latter is essential to large scale medical, industrial, commercial and residential usages, such as sanitation, distillation, water heating and cleaning.

Another important category of application is achieved by utilization of optical properties of the LSPR. The optical properties are often signatored by optical scattering spectra as well as near-field field enhancement (The calculated field intensity  $|E|^2$  under unity incident intensity). One important example is derived from the strong dependence of LSPR on ambient dielectric constant: when a spectral shift of the LSPR is sensed, it is usually inferred that the dielectric of the surrounding ma-

material has been changed, if other factors can be reasonably deemed unchanged. The shift of LSPR is generally quite sensitive to a small change of the ambient dielectric constant, so by turn the shift of the LSPR can be used to sense a tiny dielectric change in the surrounding environment of the studied particle. One can also utilize field related properties of the nanoparticle plasmon for optical applications, such as Surface-Enhanced Raman Spectroscopy (SERS) [125] and particle-trapping [126] where field enhancement and field-gradient are exploited respectively.

### 1.3.2 Nanocluster

Similar to SERS, Four-Wave Mixing (FWM) can also benefit from the strong field enhancement often associated with LSPR. Plasmonic nanoclusters, an ordered group of metallic nanoparticles intercoupled to each other, can exhibit Fano resonances (FR) [90, 91] originated from the intercoupling between their subradiant and superradiant plasmon modes. In the spectral position of Fano resonance, highly localized, intense near fields arises from strongly enhanced absorption, giving the potential to enhance nonlinear optical processes [120]. Furthermore, a double resonant structure tuned at operating frequencies is desired for a highly efficient FWM.

## 1.4 Outline

In this thesis we present several studies on the plasmonic properties and relevant applications of metallic nanostructures with different confinement dimensionalities.

In Chapter 2, we report a perfect absorber designed as a hybrid layered structures featuring a silver nanofilm perforated by a periodic array of holes with varying radii. This absorber exhibits wide-angle near-unity absorbance in the visible regime. The periodicity of the structure enables excitation of SPPs, and results in a splitting of the absorbing peaks between which the gap is dependent on the hole radius. An analytical formalism based on perturbation theory was developed to provide results in excellent agreement with experimental data and showed how the absorption peak can be potentially tuned with hole geometry, periodicity and material parameters. Being extendable to more complex hybrid structures, our result is important for the development of photon harvesting devices and thermal emitters.

In Chapter 3, we present several studies on the nanowires with various cross-sectional shapes, materials (gold or silver), and ambient medium. Basic plasmonic properties, such as resonances, propagation lengths, and induced charge distributions of different excited plasmonic propagating modes are investigated accordingly. In Section 3.1, we report that a gold nanobelt with rectangular cross section of nanoscale height and width, under epi-bright illumination, exhibits a tunable resonant wavelength that approximately linearly redshifts with increasing aspect ratio. In Section 3.2, for a nanobelt of cross section of  $125 \times 40 \text{ nm}^2$  and at 850 nm maximum emission intensity, we further show the propagation properties of the two modes excited by longitudinal ( $m = 0$ ) and transverse ( $m = 1$ ) polarizations with respect to the belt length. In FDTD simulations, a cross over of the  $m = 0$  and 1 mode intensities is

predicted at around  $7.6 \mu\text{m}$ , which is verified by experimental results at  $\sim 7.7 \mu\text{m}$ . Although higher mode confinement often indicates a trade off in propagation length, we report a mode area of  $\sim 2400 \text{ nm}^2$  associated with a propagation length of  $17.5 \mu\text{m}$ , leading to a figure of merit (FOM), introduced by Buckley et al. [127], as high as  $\sim 1300$ . This FOM may have been the highest one for a sub-wavelength guiding structure made of a bare metallic nanowire and operated near infrared regime. In Section 3.3, we report an observed stimulated emission of SPP (SESPP) in a sub-wavelength silver nanowire supported by a gain (active) medium. The SESPP was found to compensate the intrinsic loss of the dominant propagating mode and thus increase the propagation length from  $6.3$  to  $7.0 \mu\text{m}$ , as simulated in FDTD calculations.

In Chapter 4, we report a practical thermal application enabled by nanoparticles, i. e. the plasmon-heated bubble generation. In Section 4.1, we report a study on the characterization of observed nanobubble out of a plasmon-heated gold nanosphere under the illumination of continuous-wave laser. The size, pressure and temperature of the bubble are characterized using a simple model which incorporates the bubble-induced spectral blueshift and continuum medium model. We also performed surface Raman spectroscopy to measure the surface temperature of the gold nanosphere and the measured temperature well agreed with the characterized one in our model. Further, in Section 4.2, a local-field weighted effective medium method (LFWEMM) is proposed, developed and applied to in the characterization (determining the size, pressure and temperature, etc.) of the nanobubble generated by the LSPR of gold

nanosphere. A benchmark test with other effective medium methods (EMMs) was performed and it is shown that LFWEMM exceeds the boundary of traditional EMM and delivers more accurate results of bubble radius, while conserving a virtue of mean field theory and a concise mathematical description. The pressure and temperature of nanobubble, together with the nanoscale thermal conductance of gold-steam and steam-water interfaces, were therefore calculated using a classical heat equilibrium theory, revealing that the saturated steam at nanoscale behave as an ideal thermal conductor. Our study of the LFWEMM demonstrates the importance and significance of including near-field patterns in effective medium method in a field-localized scenario, and thus has bridged the gap between the highly localized plasmonic field and averaging-based EMM, indicating further potential applications of this LFWEMM in other scenarios with highly localized field.

In Chapter 5, a gold nanocluster supporting two distinct FRs is designed and fabricated. We show that the optical Four-Wave Mixing (FWM) process taken in this structure exhibit a higher efficiency, than in other double-resonant plasmonic clusters that lack this specific property. A model that explains the observed FWM features is proposed, based on the numerically simulated intense local fields at the nanocluster surfaces. This model is generally applicable to any third-order processes in plasmonic nanostructures. Having a larger effective susceptibility  $\chi^{(3)}$  relative to existing nonlinear optical materials, this double FR nanocluster open a new area of high-performance third-order nonlinear optical media designed with plasmonic nan-

ocluster.



## Chapter 2

### Nanofilm based perfect absorber

#### 2.1 Motivation

The collective oscillations of free electrons at dielectric-metal interfaces constitute propagating modes referred to as surface plasmon polaritons (SPPs). The discovery of extraordinary transmission of light through a periodically perforated metallic film [5] has largely contributed to defining an emerging research area of anomalous light-metal interactions [6, 17, 18]. Being complementary to the extraordinary transmission phenomenon, the concept of plasmonic perfect absorber (PPA) [19, 20, 21] has stimulated a new research field of clear relevance for solar energy harvesting applications [25, 123, 124, 23]. SPP excitation has been shown to account for a wide range of resonant phenomena in perforated metallic structures, both in the optical and terahertz regime [7]. The perforated hole array play a crucial role in designer SPPs [7] in the terahertz regime where the metal is essentially a perfect electric conductor. In the visible regime, the shape and size of the subwavelength hole array have strong influences on the extraordinary resonant phenomena [14, 15, 16]. The periodicity introduced in SPP systems, can induce two distinct effects: (I) a significantly enlarged density of states (DOS) above the light line, both for localized surface plasmon scat-

terers [128, 129] and in SPP systems [6, 130, 131, 132]; (II) a photonic band gap (PBG) effect [6, 130, 133], where the increased density of leaky modes above the light line makes wide-angle coupling from incident light to leaky Bloch modes possible. An alternative Bloch mode based description has also been reported by P. Lalanne et al. [134, 135] A subsequent coupling from Bloch modes to highly confined SPP modes, whose planar momentum differs by a reciprocal lattice vector  $G$ , finally leads to the perfect absorbing phenomenon. For a perfect absorber to be useful in typical photon-absorbing applications/thermal emitters, it is often desired to exhibit unity absorption/zero reflectance for a broad range of incident angles [20, 22, 23], broad- or multi-band near unity absorption [23, 24] or zero reflectance [22], and wavelength tunable absorption characteristics. While significant progress in developing such a device has recently been made [19, 20, 21, 25, 23, 26, 27], the underlying interacting physical modes are yet to be better elaborated. Moreover, since the knowledge in the relation between hole size and resonant energy shift is limited [15], a further investigation of the hole size effect would be necessary.

In this chapter, we report the development of a PPA which possesses several of these desired characteristics [1]. We present experimental measurements (Section 2.2) and an analytical theoretical analysis (Section 2.3) of a metallic hole array based structure that exhibit near unity absorbance in the visible for a wide range of incident angles and also exhibit tunable absorption characteristics. Most interestingly, a splitting of the absorption peak is observed resulting in two absorption peaks with

energy difference that oscillates with the hole radius of the array, i.e. direct evidence of the tunability of the device. This splitting can be explained using an analytical model based on degenerate perturbation theory. This general theoretical model provides a simple understanding of the physics underlying the PPA phenomenon and, most importantly, provide the framework for a systematic design of PPA based on metallic hole arrays of different materials and structures with desired absorption characteristics of relevance in light harvesting applications.

## 2.2 Experimental measurements

The Fourier transform infrared spectroscopy (FTIR) setup is shown in Fig. 2.1(a). The incoming light is split by a beam splitter and then reflected by a concave mirror which focuses the light onto the sample PPA. The heterostructural geometry of the PPA is shown in Fig. 2.1(b) and consists of three layers with a thick Ag mirror ( $h_3 = 80$  nm) at bottom, and a thin Ag film at top ( $h_1 = 20$  nm). The middle  $\text{SiO}_2$  dielectric spacer ( $h_2 = 40$  nm) functions as a bridge to couple the SPPs on the two Ag films. This triple-layer plasmonic structure was fabricated by using electron beam evaporation. Focused ion beam (FIB) milling (Nava 200, FEI Co.) was then used to generate a periodic array of circular holes on the top Ag film. The sample has a structural footprint of  $100 \times 100 \mu\text{m}$ . The period in both  $x$  and  $y$  directions is  $L = 240$  nm, and the hole radius ( $R$ ) is varied from 40 to 90 nm.

The measured reflectances ( $\mathbb{R}$ ) under slightly oblique incidence (as shown in

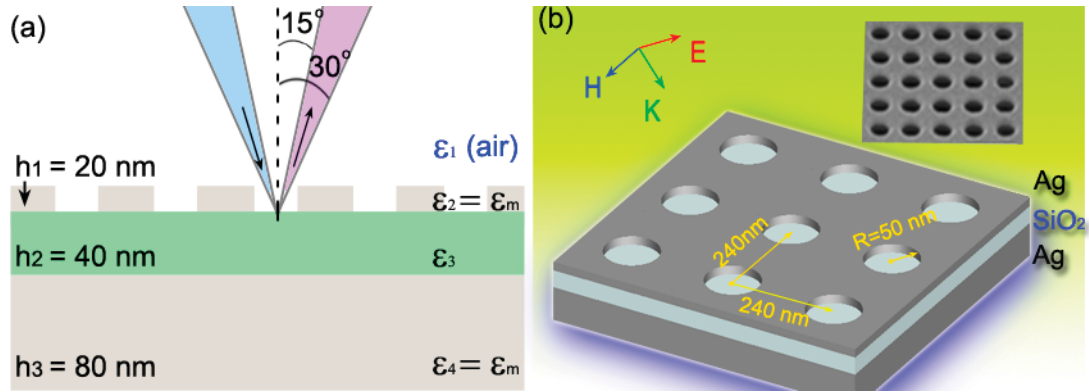


Figure 2.1 : Schematic of the experimental configuration (a) and the perfect absorber structure (b). Inset is the SEM image for the hole array. [1] ©2012 APS

Fig. 2.1(a)) are plotted in Fig. 2.2(a) for hole radii  $R$  changing from 30 to 80 nm in 10 nm steps. The measurements were performed using FTIR, with in-plane magnetic field polarization (TM) as illustrated in Fig. 2.1. The transmittance of the structure is totally eliminated ( $\mathbb{T} = 0$ ) in the visible regime due to the small penetration depth ( $\sim 20$  nm at these frequencies) relative to the thickness of the bottom Ag mirror. A narrow-band of perfect absorbance  $\mathbb{A} = 1 - \mathbb{T} - \mathbb{R}$  is observed around 646 nm for  $R=30\sim 50$  nm. When the hole radius is larger than 50 nm, a clear splitting of the reflectance dip is observed. Neither of the split dips are non-zero for 70 and 80 nm radius but still exhibit a high level absorbance. The splitting that appears for 60 nm radius demonstrates that it is able to expand the narrow dip into a broader one, which shows the potential of this structure for realizing broad- and multi-band PPA functionality. In Fig. 2.2(b) we show how the absorption depends on the incident angle. The data shows that the absorbance remains higher than 89% over a wide incident angular range around  $90^\circ$ . It was also experimentally found that the optimal

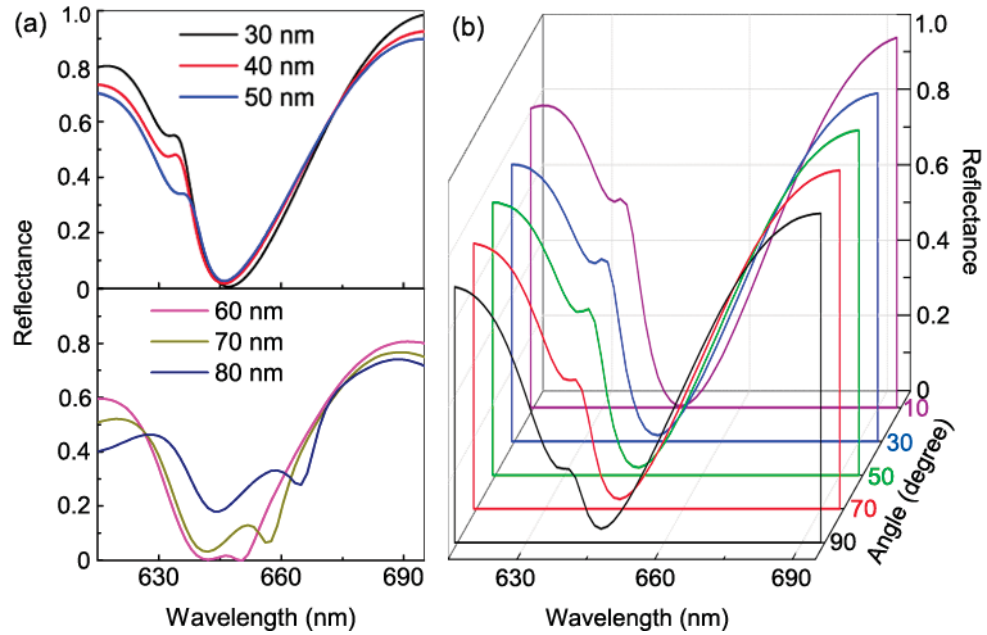


Figure 2.2 : (a) Experimental reflectance for hole radius changing from 30 to 80 nm. A perfect absorber ( 99% absorbance) is realized when the hole radius is 50 nm and an clear spectral splitting is observed for radius 60~80 nm. (b) Measured reflectance for different angles of incidence for a hole radius 50 nm. All the spectra in (a) were collected under slightly oblique incidence as shown in Fig. 2.1(a). [1] ©2012 APS

thickness of the top Ag layer is about 20 nm for the presence of the perfect absorption band.

Further, it is worth mentioning that because this work is motivated by perfect photon-absorbing applications such as the optical black body/thermal emitters, we are interested in a system where all the absorbed energy is dissipated into heat in the metal, and no unwanted losses is expected. As a result, we choose  $\text{SiO}_2$  as the middle spacer for our visible regime perfect absorber. In contrast, if the  $\text{SiO}_2$  was replaced with Si, there would be some loss due to the interband transitions in Si, which is unwanted.

## 2.3 Theoretical description

In the theoretical modeling of this work, our aim is not to at providing direct comparison with the experimental spectrum, which can be done by performing numerical calculations of the reflection, transmission or absorption spectrum by employing efficient S-matrix methods [136, 137, 138], also known as Fourier modal method [14, 16, 20] or rigorous coupled-wave analysis [135], as well as other available commercial packages such as finite-integration time-domain [21], finite-difference time-domain [23, 139, 22], etc. Instead, we'd like to introduce a simple coupling mechanism between incident wave and the excited SPPs followed by a detail analytical modeling based on degenerate perturbation concept, in order to explain the observed split of the perfect-absorbing, which has not been reported to our knowledge.

### 2.3.1 Coupling mechanism

Figure 2.3(a) illustrates the PPA mechanism in which the coupling of incident light into highly confined SPP is enhanced by employing leaky Bloch modes, possessing increased DOS (PBG effect) as an efficient bridge. In reciprocal space, the states at the highly symmetric points of the Brillouin Zone (BZ) are degenerate because the difference with each other is a multiple of reciprocal lattice constant  $2\pi/L$ . The periodic perforation, thus leads to interaction of these states and the formation of hybridized states consisting of linear combinations of the unperturbed states (PBG effect). This effect accounts for the energy splitting near symmetric points of BZ.

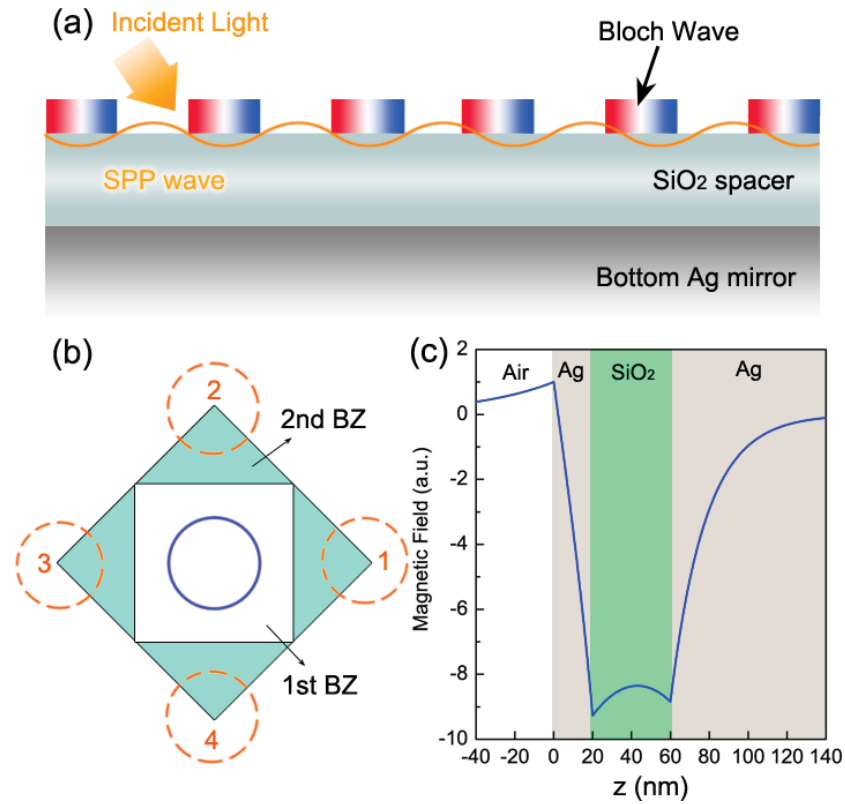


Figure 2.3 : (a) Excitation mechanism of the SPP responsible for perfect absorption in our device. (b). BZ schematics. Incident light with small in-plane wave vectors (inside blue circle) excites the Bloch mode; the latter then acquires crystal momentum to excite the SPP with corresponding in-plane wave vector (within orange dash circles). (c). Lateral magnetic field of the unperturbed state. See text for parameters. [1] ©2012 APS

Due to the periodicity of the structure, the incident light with its small transverse momentum can couple to states with  $k$ -vectors [6], as indicated in Fig. 2.3(b).

### 2.3.2 A perturbative approach

We now develop a perturbative approach for describing the hybridized states. Since the unperforated hybrid structure has been extensively studied with rigorous fully retarded approaches [46, 45], we use this solution as the zero-order unperturbed so-

lution. We then consider the perforations as perturbations and derive the first order corrections using degenerate perturbation theory. Because the unperforated structure was considered as an infinitely large planar heterolayered structure, it does not support TE modes, but only TM modes with spatial components

$$\mathbf{H}^{(0)}(\mathbf{k}) = H_0 f(z) e^{i\mathbf{k}_{\parallel} \cdot \rho} \mathfrak{R} \hat{\mathbf{k}}_{\parallel}, \quad (2.1)$$

and time dependences of  $e^{-i\omega_0 t}$ .

By assuming an infinitely thick bottom Ag layer, the lateral distribution of the field has the form

$$f(z) = \begin{cases} e^{S_1 z} & 0 < z \\ \cosh(S_2 z) + \frac{S_1 \epsilon_m}{S_2 \epsilon_1} \sinh(S_2 z) & 0 \leq z < h_1 \\ C \cosh(S_3(z - h_1)) + D \sinh(S_3(z - h_1)) & h_1 \leq z < h_1 + h_2 \\ [C \cosh(S_3 h_2) + D \sinh(S_3 h_2)] e^{-S_4(z - h_1 - h_2)} & z \geq h_1 + h_2 \end{cases}, \quad (2.2)$$

where  $\mathbf{k}_{\parallel} = k_x \hat{x} + k_y \hat{y}$  is the in-plane wave vector of the SPP's,  $\rho$  is the field point vector projected on  $x - y$  plane with  $\mathbf{r} = \rho + z \hat{z}$ . The quantities  $S_i = \sqrt{k_{\parallel}^2 - \epsilon_i \omega_0^2 / c^2}$  are the wave vectors normal to the interfaces in regions  $i = (1, 2, 3, 4)$  (See Fig. 2.1(a)),  $H_0$  is a constant complex amplitude, and  $\mathfrak{R} \hat{\mathbf{k}}_{\parallel}$  is a unit vector rotated from  $\hat{\mathbf{k}}_{\parallel}$  by  $\pi/2$  clockwise, with  $\mathfrak{R}$  denoting the rotation operator. The coefficients in Eq. (2.2) are determined by the continuity of the tangential magnetic field at the interfaces:

$$C = \cosh(S_2 h_1) + \frac{\kappa_1}{\kappa_2} \sinh(S_2 h_1), \quad (2.3)$$

$$D = [\kappa_2 \sinh(S_2 h_1) + \kappa_1 \cosh(S_2 h_1)] / \kappa_3, \quad (2.4)$$



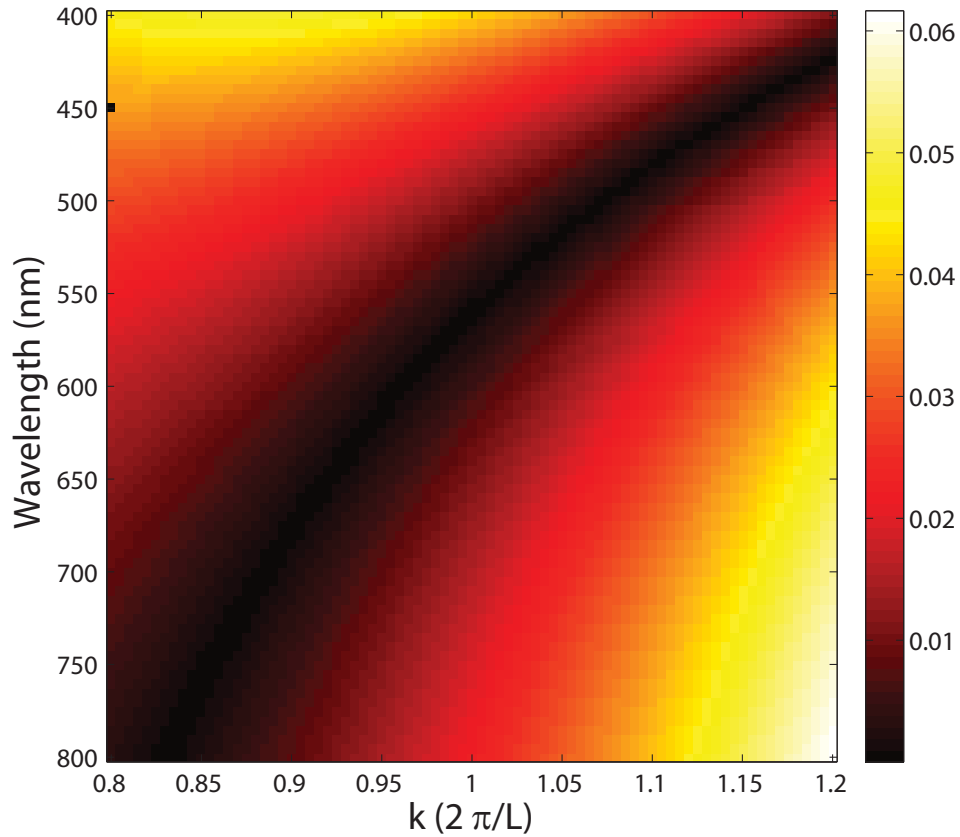


Figure 2.4 : Dispersion relation diagram of the hybridized surface plasmon polariton in the unperturbed heterostructure. The absolute value of the left hand side of Eq. 2.5 as a function of wavevector  $k$  and wavelength is plotted and the dispersion relation is then indicated by the black curve where such value vanishes. [1] ©2012 APS

with  $\kappa_i = S_i/\epsilon_i, i = (1, 2, 3, 4)$ . The parameters  $\epsilon_2 = \epsilon_4 = \epsilon_m$  are the relative permittivity of the metal. The dispersion relation  $\omega(\hat{\mathbf{k}}_{\parallel})$  is obtained from

$$C[\kappa_3 \tanh(S_3 h_2) + \kappa_2] + D[\kappa_3 + \kappa_2 \tanh(S_3 h_2)] = 0, \quad (2.5)$$

and is shown as the black curve in Fig. 2.4. Notice that for the wavevector of  $k = 2\pi/L$  the resonant wavelength is  $\sim 560$  nm, as read from the dispersion diagram, having

around  $\sim 15\%$  difference from the experimental value of 646 nm.

In order to develop a perturbative approach, we need to find an operator for which the plasmon modes are eigenstates. A simple choice for such an operator is  $\Theta_0 \equiv \nabla \times (\epsilon_i^{-1} \nabla \times)$  [140]. In each region we have,

$$\Theta_0 \mathbf{H}^{(0)} = -\frac{1}{\epsilon_i} \nabla^2 \mathbf{H}^{(0)} = \frac{k^2}{\epsilon_i} \mathbf{H}^{(0)} = \frac{\omega_0^2}{c^2} \mathbf{H}^{(0)}, \quad (2.6)$$

where  $\mathbf{k} = k_x \hat{x} + k_y \hat{y} - iS_i \hat{z}$ , and  $\omega_0^2 = c^2 k^2 / \epsilon_i$ . Thus the operator  $\Theta_0$  plays the same role as the Hamiltonian operator in quantum mechanics, and standard degenerate perturbative theory can be applied [140] with the unperturbed energies being equal to  $\omega_0^2 / c^2$ . The perturbation resulting from the holes is thus described by a term

$$\Theta' \equiv \nabla \times \left[ \left( \frac{1}{\epsilon_m + \Delta\epsilon(\mathbf{r})} - \frac{1}{\epsilon_m} \right) \nabla \times \right], \quad (2.7)$$

where  $\Delta\epsilon(\mathbf{r})$  is the permittivity change due to the perforation, and the total operator is  $\Theta = \Theta_0 + \Theta'$ . To make the operator  $\Theta$  Hermitian,  $\epsilon_i$  must be real. While this model can take into account the dispersion in metal permittivity by substituting  $\epsilon_m = 1 - \omega_p^2 / \omega^2$  where  $\omega_p$  is the bulk plasma frequency of the metal, for silver in our narrow frequency range we use  $\epsilon_m = -19$  and for layers 1 and 3 we use  $\epsilon_1 = 1, \epsilon_3 = 2.25$ . The imaginary part of  $\epsilon_m$  is here neglected because it is much smaller than the real part in the visible regime and we focus on the mode energies instead of dissipation. By referring to the optical constants of silver in literature [141], we confirmed that the magnitude ratio of the imaginary part to real part of silver permittivity, i. e.  $abs(\text{Im}(\epsilon_{Ag}) / \text{Re}(\epsilon_{Ag}))$ , is less than 5% for free space wavelength 400~800 nm.

As illustrated in Fig. 2.3(b), no matter how large the incident angle is, the in-plane incident wave vector is always small (within the blue solid circle) compared with the reciprocal lattice constant  $2\pi/L$ . As result, any excited SPP always carries an approximate momentum as  $\mathbf{G}/2$  (within the orange dashed circle), determined by conservation of crystal momentum. After perforation, the four states with in-plane wave vectors of  $\mathbf{k}_i = (\pm 2\pi/L, \pm 2\pi/L)$  are degenerate because they are on the vertices of the 2nd BZ which are equivalent points separated in  $k$  space by  $\mathbf{G}$ . These four states are numbered in Fig. 2.3(b) and will be referred to below. The lateral distribution of the magnetic field of unperturbed state calculated from Eq. (2.2) is plotted in Fig. 2.3(c), showing a strong field confinement consistent with findings from previous studies of similar systems [142, 21]. The lateral penetration depth  $1/S_2$  of these states is  $\sim 20$  nm, which is much smaller than the 80 nm thickness of the bottom Ag layer thus rendering the approximation of an infinitely thick bottom layer valid. For instance, at the dielectric-metal surface of the bottom Ag layer ( $z = 60^+$  nm), the magnitude reads 8.84, while at about one penetration depth away from such surface ( $z = 80$  nm) it reads 2.92, showing approximately  $1/e$  decay and thus supporting a penetration depth of  $\sim 20$  nm. At the far end surface of the Ag layer ( $z = 140$  nm), the magnitude has decayed into a negligible value of 0.11 or 1.2% of the value at  $z = 60$  nm.

The hybridization and energy splitting due to the perturbation can be found by expanding the perturbed states in the unperturbed degenerate states Eq. (2.1), as

in conventional degenerate perturbation theory. The secular equation takes the form  
(See detailed derivation in Appendix A of Ref. [1]),

$$\det \begin{vmatrix} \Omega_1 - \Delta\omega^2/\omega_0^2 & \Omega_2 & \Omega_3 & \Omega_2 \\ \Omega_2 & \Omega_1 - \Delta\omega^2/\omega_0^2 & \Omega_2 & \Omega_3 \\ \Omega_3 & \Omega_2 & \Omega_1 - \Delta\omega^2/\omega_0^2 & \Omega_2 \\ \Omega_2 & \Omega_3 & \Omega_2 & \Omega_1 - \Delta\omega^2/\omega_0^2 \end{vmatrix} = 0, \quad (2.8)$$

where

$$\begin{aligned} \Omega_1 &= \left(\frac{\epsilon_m}{\epsilon_1} - 1\right) \frac{F_1 \pi R^2}{F_0 L^2}, \\ \Omega_2 &= \left(\frac{\epsilon_m}{\epsilon_1} - 1\right) \frac{F_3 R J_1(2\sqrt{2}\pi R/L)}{F_0 2\sqrt{2}\pi L}, \\ \Omega_3 &= \left(\frac{\epsilon_m}{\epsilon_1} - 1\right) \frac{F_2 R J_1(4\pi R/L)}{F_0 4\pi L} \end{aligned} \quad (2.9)$$

are determined by the interaction matrix elements  $(\mathbf{H}^{(0)}(\mathbf{k}_i), \Theta' \mathbf{H}^{(0)}(\mathbf{k}_j))$  with  $i, j \in \{1, 2, 3, 4\}$ , as well as by the normalization condition  $(\mathbf{H}^{(0)}(\mathbf{k}_i), \mathbf{H}^{(0)}(\mathbf{k}_i)) \equiv 1$ . The  $F_i$  coefficients are functionals of  $f(z)$  which is described by Eq.(2.2)) and can be written as (See Appendix A of Ref. [1]),

$$\begin{aligned} F_0(f(z)) &= \int_{-\infty}^{+\infty} \left[ \left( \frac{\partial f(z)}{\partial z} \right)^2 + k_i^2 f^2(z) \right] dz, \\ F_1(f(z)) &= \int_0^{h_1} \left[ \left( \frac{\partial f(z)}{\partial z} \right)^2 + k_i^2 f^2(z) \right] dz, \\ F_2(f(z)) &= \int_0^{h_1} \left[ - \left( \frac{\partial f(z)}{\partial z} \right)^2 + k_i^2 f^2(z) \right] dz, \\ F_3(f(z)) &= \int_0^{h_1} k_i^2 f^2(z) dz. \end{aligned} \quad (2.10)$$

The eigenenergies of Eq. (2.6) are readily obtained as

$$\begin{aligned}
\left(\frac{\Delta\omega^2}{\omega_0^2}\right)_{1,2} &= \Omega_1 - \Omega_3, \\
\left(\frac{\Delta\omega^2}{\omega_0^2}\right)_3 &= \Omega_1 - 2\Omega_2 + \Omega_3, \\
\left(\frac{\Delta\omega^2}{\omega_0^2}\right)_4 &= \Omega_1 + 2\Omega_2 + \Omega_3,
\end{aligned} \tag{2.11}$$

where the eigenstates 1 and 2 are degenerate. The corresponding eigenvectors and spatial field patterns of these modes are

$$\begin{aligned}
V_1 &= (0, -1, 0, 1)^T, & H \propto \sin \frac{2\pi y}{L}; \\
V_2 &= (-1, 0, 1, 0)^T, & H \propto \sin \frac{2\pi x}{L}; \\
V_3 &= (-1, 1, -1, 1)^T, & H \propto \sin \pi \frac{x+y}{L} \sin \pi \frac{x-y}{L}; \\
V_4 &= (1, 1, 1, 1)^T, & H \propto \cos \pi \frac{x+y}{L} \cos \pi \frac{x-y}{L}.
\end{aligned} \tag{2.12}$$

In Fig. 2.5(a)-(c), the magnetic field patterns of eigenstates 1,3,4 are plotted. After perforation by small holes such that  $J_1(2\sqrt{2}\pi R/L) > 0$ , the energy of state 3, as in Fig. 2.5(b), is higher than that of state 4 as in Fig. 2.5(c). This is because the lower energy state tends to have more electromagnetic energy stored in region of high permittivity to be more stable [140]. As is shown in Fig. 2.5(c), the lower energy state 4 has intensity maximum in the center of the holes where the permittivity is higher than that of silver; in contrast, the state 3 in Fig. 2.5(b) experiences field nodes in the hole center resulting in higher energy. For the state 1 shown in Fig. 2.5(a), since the spatial modulation of field is not as violent as in state 3 and 4, the energy is even lower.

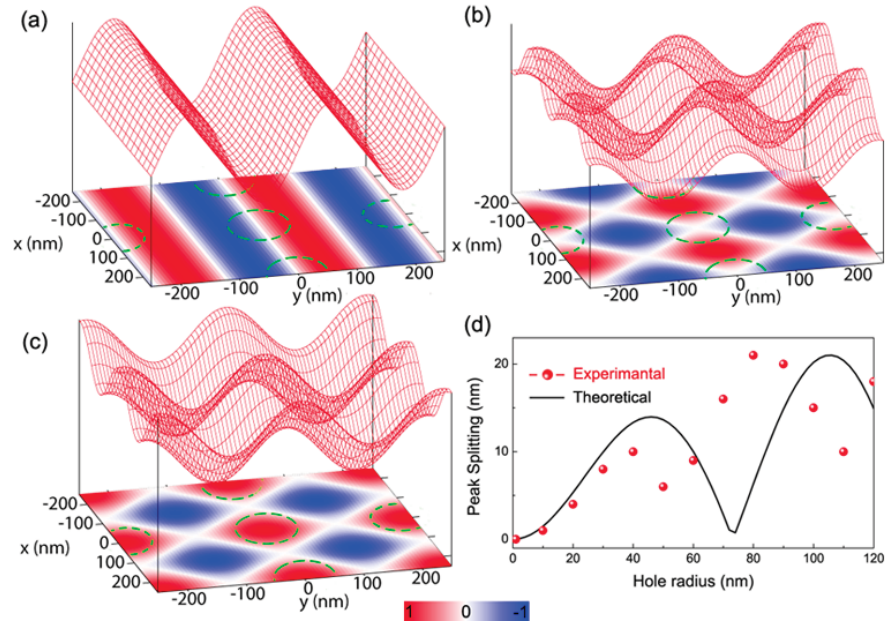


Figure 2.5 : (a-c) Magnetic field ( $H$ ) patterns of the three unperturbed eigenstates described in the text. The green circles indicates the holes. (d) The dependence of the absorption peak splitting on hole radius. The normalized theoretical result (black line) represents a same oscillation trend as the experimental data (red dots). [1] ©2012 APS

There are three possible energy gaps in this system. By using the approximation  $\sqrt{1 + \Delta} \approx 1 + \Delta/2$  and writing the perturbed mode energies  $\omega_i$  in terms of  $\Delta\omega^2$ , we have  $\omega_i \approx \omega_0 [1 + 0.5 (\Delta\omega^2/\omega_0^2)_i]$  and hence the possible gaps are

$$\delta\omega^{(1)} \equiv |\omega_3 - \omega_4| \approx 2\omega_0|\Omega_2|, \delta\lambda^{(1)} \approx 2\lambda_0|\Omega_2|;$$

$$\delta\omega^{(2)} \equiv |\omega_3 - \omega_1| \approx \omega_0|\Omega_2 - \Omega_3|, \delta\lambda^{(2)} \approx \lambda_0|\Omega_2 - \Omega_3|;$$

$$\delta\omega^{(3)} \equiv |\omega_4 - \omega_1| \approx \omega_0|\Omega_2 + \Omega_3|, \delta\lambda^{(3)} \approx \lambda_0|\Omega_2 + \Omega_3|.$$

(2.13)

Noting that it is hard to tell the sign of the splitting from the experiment, we

use the absolute values in the above expressions for the shift. Since the calculated  $F_3/F_0 = 0.028$ , is much smaller than  $F_2/F_0 = -0.52$ , the observed splitting should be dominated by  $\lambda_0|\Omega_3|$ . In Fig. 2.5(d) we compare the calculated splitting  $\lambda_0|\Omega_3|$  with the measured split of the absorption peaks for different hole radii. The results agree qualitatively and shows that the magnitude of peak split exhibit an oscillatory behavior with the hole radius. As seen in Fig. 2.2(a) and Fig. 2.5(d), for small radii, the splitting is small but still discernible for radii in the range 30~50nm. As the radius increases, the split decreases and then become large for radii 60~80 nm, and then decreases again. This oscillation of the peak splitting originates from the perforation-induced two-dimensional periodicity. A close inspection of the theoretical result reveals that the splitting depends on a number of factors, including the hole radius, array period and the geometry of the hybrid structure. Such information, for instance the layer thicknesses and material permittivities, is contained in the function  $f(z)$  in Eq. (2.2). Our simple theoretical model can thus straightforwardly be used for the design and optimization of the PPA. Moreover, since the unperturbed states are the SPP modes of a hetero-layered structure, our approach can readily be extended to more complicated layered structures, including more layers and different materials.

## 2.4 Conclusion

In conclusion, we have experimentally realized and characterized a hetero-layered hole array structure that exhibit wide-angle perfect absorbing capability in the visi-

ble region of the spectrum. We suggest that this ability is attributed to an increased photonic density of states (flat band) above the light line, which is a feature of coupled periodic plasmonic system. This increased density of states mediates a coupling between the incident light with its small in-plane momentum and surface plasmon polaritons at high symmetry points of the two dimensional Brillouin zone boundary. A spectral splitting of the reflectance dip (absorption peak) is clearly observed in the experiments and may be important for future multi-band or broadband energy harvesting applications. A simple model based on degenerate perturbation theory provides a qualitative description of the phenomenon and can be used to further optimize the device. This model can straightforwardly be extended to more complicated periodic structures and serve as a design tool for the development of perfect absorbers exhibiting multi-band or broadband absorption.



## Chapter 3

### Plasmonic properties of nanowires

#### 3.1 Surface plasmon resonance of nanobelt

##### 3.1.1 Introduction

Noble metal nanostructures with sub-wavelength dimensions exhibit localized surface plasmon resonances when excited by light. These resonances lead to strong absorption, scattering, and near field enhancement at frequencies that depend on the nanoparticle size and shape [143]. Over the past decade, a wide variety of plasmonic gold and silver structures have been fabricated to manipulate light at the nanometer scale where they are pursued for novel applications and basic research [144, 145]. For example, plasmon resonant optical absorption enables molecularly targeted heating for applications in nanomedicine such as photothermal therapy and drug delivery [146, 147]. Larger plasmonic nanostructures exhibit bright plasmon resonant scattering which may prove useful for microscopic imaging contrast and particle tracking [148, 149]. Nanoparticles with sharp tips and gaps between nanoparticles create regions of highly enhanced electromagnetic fields which amplify powerful spectroscopies for sensing applications [150]. Plasmonic nanoparticles can be coupled to fluorescent dyes or quantum dots to manipulate radiative decay rates and directions, thus fun-

damentally manipulating optical emission [151, 152]. All of these applications rely to some extent on the ability to tune nanoparticle plasmon resonances to match a biological window of tissue transparency, to coincide with an emitter excitation, or simply to match a laser source. The capability to tune the plasmon resonance has played a crucial role in stimulating the current interest in plasmonics. Plasmonic effects are also studied in extended structures where they may be used to transport optical information at the nanometer scale. For example, light can be coupled into surface plasmon polaritons in two dimensional films, and its propagation can be manipulated by nanostructures within the film [153, 6] Recently there has been interest in plasmon propagation in one dimensional plasmonic nanowires [124]. Here light can be coupled into and out of the nanowires through symmetry broken sites such as tips, kinks, or nanoparticle-nanowire junctions [154, 155]. The coupling between propagating nanowire plasmons and nearby quantum dots could enable the integration of plasmonic structures into nanometer scale optoelectronic devices [156, 157, 158, 159]. Nanowire propagating plasmon modes have been studied largely with silver nanowires that have cross-sectional diameters of hundreds of nanometers [154, 39, 41, 160]. While these efficiently couple, transport, and emit light, their large size leads to transport based on a mixture of higher order plasmonic modes and may limit the strength of interactions with nearby emitters and other plasmonic structures [34].

Here we describe the optical properties of gold nanowires with rectangular cross sections referred to as gold nanobelts [161]. Their sub-100 nm cross-sectional di-

mensions and extended lengths (larger than  $10\ \mu\text{m}$ ) combine the tunability and sharp resonances of sub-wavelength sized nanoparticles with the extended structure of nanowires. The detail of the synthesis of the gold nanobelt can be found in Ref. [2].

### 3.1.2 Sharp resonance

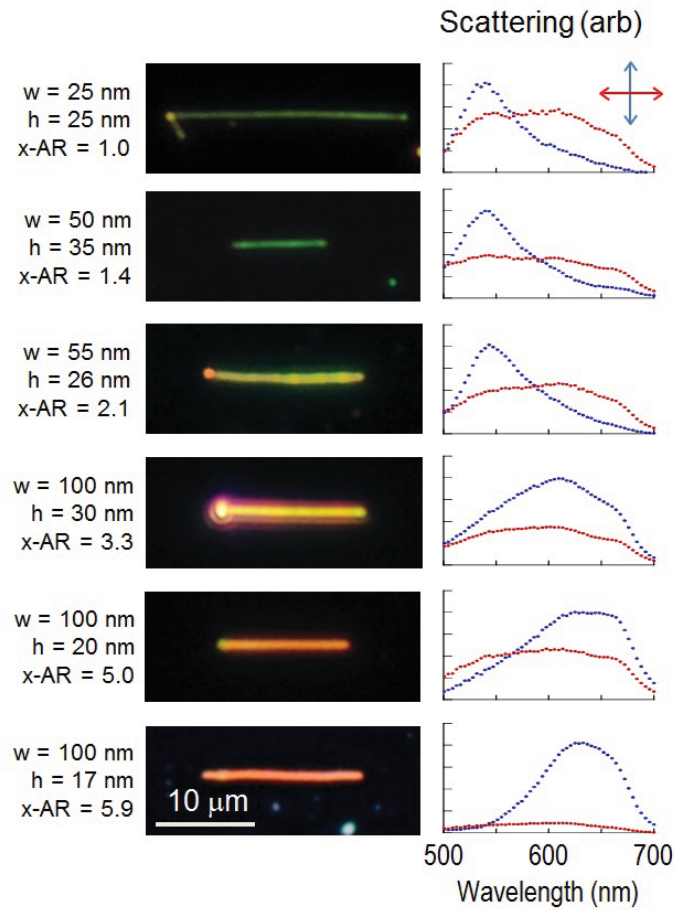


Figure 3.1 : Dark field micrographs (left) and corresponding single nanobelt spectra (right). The given dimensions and aspect ratio were determined by atomic force microscopy. The blue spectra are polarized transverse to the nanobelt, and the red spectra are polarized parallel to the nanobelt. [2] ©2011 ACS

As seen in Figure 3.1, the nanobelts exhibit a range of colors covering the visible spectrum from green to red. These same nanobelts were imaged by atomic force microscopy (AFM) to determine their height and width, also provided in Figure 3.1 (see the Supporting Information for AFM images and analysis of Ref. [2]). Here we define the cross-sectional aspect ratio, x-AR, as the nanobelt width divided by the height. Since these nanobelts are very long, we do not consider the length to width aspect ratio that has been addressed in previous studies [162, 163]. As seen in the dark-field images, the existence of a tunable plasmon resonance is apparent, as nanobelts with low cross-sectional aspect ratio appear green and those with higher aspect ratio appear red. The nanobelt scattering spectra were recorded from the center of each belt by an imaging spectrograph and CCD camera. White light was incident through the annular dark field objective and was unpolarized. A polarizer behind the objective analyzed the scattered light. As seen in Figure 3.1, the measurements reveal a plasmon mode polarized perpendicular to the nanobelt length which redshifts with increasing cross sectional aspect ratio. Also shown are scattering spectra polarized parallel to the nanobelts, which were relatively featureless.

### 3.1.3 Simulation

To understand the nature of the observed nanobelt plasmon resonance, finite-difference time-domain (FDTD) calculations were carried out for the nanobelt geometry using a measured dielectric function for gold [141]. The simulation geometry, shown schemat-

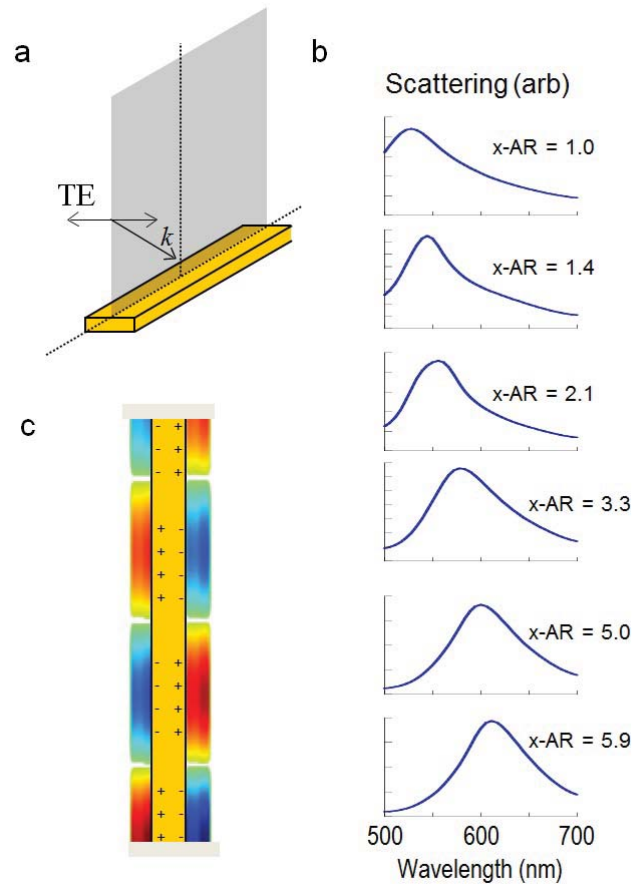


Figure 3.2 : (a) Gold nanobelt simulation geometry and (b) resulting spectra for cross-sectional aspect ratios that match Figure 3.1. (c) The calculated charge distribution of the scattering mode. [2] ©2011 ACS

ically in Figure 3.2a, was designed to match the experimental dark field spectroscopy measurements. Illumination was incident at 45 degrees to the nanobelt long axis (as in the experiment) and the total scattering cross section for an infinitely long nanobelt was calculated. The infinite nanobelt was simulated by extending it through perfectly matched layer boundary conditions that minimize reflections [164]. With the incident  $k$ -vector along the nanobelt length and TE polarization across the nanobelt as shown

in Figure 3.2a, a scattering resonance was found (Figure 3.2b) that shifts with aspect ratio in a manner similar to the experimental measurement. Analysis of the charge and field distributions showed that the bright scattering resonance is a plasmon mode with antisymmetric charge alignment across the nanobelt width as depicted by the charge distribution plot in Figure 3.2c. This mode is analogous to the propagating  $HE_1$  plasmon mode for nanowires of cylindrical cross section [165]. Note that the simulation results in Figure 3.2 do not include the substrate. However, a simulation for a finite nanobelt of cross-sectional aspect ratio 3.3 was run that included a glass substrate and it was found to have little effect, causing only an 18 nm redshift in the scattering peak (see Supporting Information in Ref. [2]). To more closely match the experimental measurement, FDTD simulations were also carried out for a finite nanobelt and the differential scattering cross section was calculated. Due to computational complexity, these simulations were performed on a nanobelt of only 0.4 micron length, which resulted in strong Fabry-Perot resonances that do not occur in our experiment because the nanobelt lengths are greater than 10 microns. We therefore chose to compare the experimental data to the total cross sections calculated for infinite nanobelts.

#### 3.1.4 Discussion

Other plasmon modes were found in the simulations that were not evident in the experiments. For instance, for TM polarization, the calculations revealed an an-

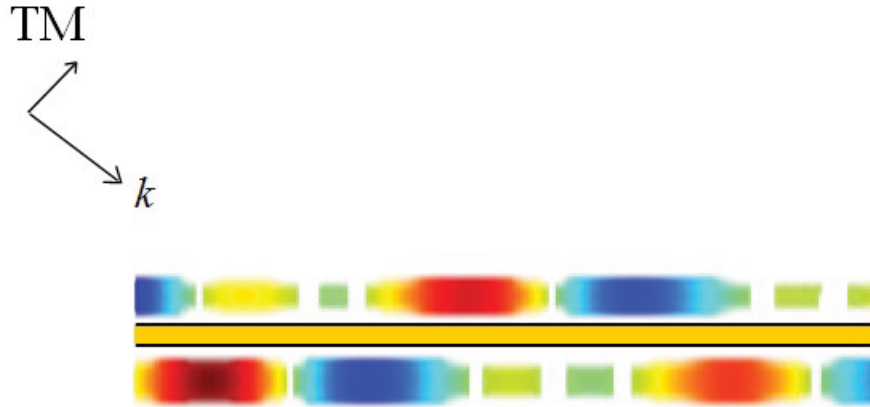


Figure 3.3 : The calculated charge distribution of the zig-zag mode at 624 nm excited by incident TM illumination. [2] ©2011 ACS

tisymmetric mode, with its dipole moment oriented in a zigzag pattern along the nanobelt length (Figure 3.3). This peculiar orientation of the dipole moment is due to an admixture of symmetric and antisymmetric plasmon modes on the upper and lower surfaces of the nanobelt [165]. The zigzag mode was found to predominantly scatter in a direction outside the numerical aperture of the microscope objective, so it was not observed.

The measured spectra of the high cross-sectional aspect ratio nanobelts appear to have some structure as though they are made up of multiple peaks. While such peaks can be attributed to substrate interactions [166], here they are artifacts of the data analysis. Different choices of the background subtraction parameters cause somewhat different spectral shapes in Figure 3.1, although they do not affect the overall tunability. In addition, the measured line widths given in Table 1 of Ref. [2]

are similar to the homogeneous line widths of single gold nanoparticles [167].

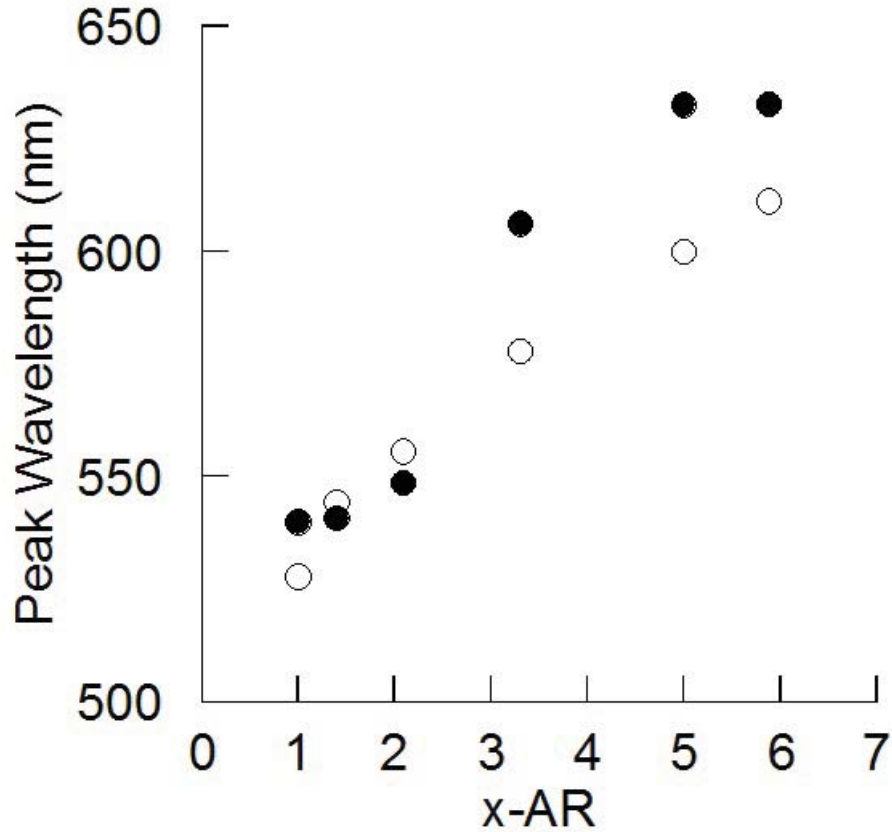


Figure 3.4 : The dependence of the plasmon resonance peak on cross-sectional aspect ratio in the experiments (●) and simulations (○) [2]. ©2011 ACS

Spectral scattering peaks for both the experiments and simulations were fitted to analyze the tunability of the transverse plasmon resonance in the nanobelt structure. The results, plotted in Figure 3.4, agree well and reveal an approximately linear relationship between the cross-sectional aspect ratio and resonance wavelength, which is very similar to the behavior for elongated nanoparticles such as gold nanorods [143]. Interestingly, the nanobelt structure has a lower sensitivity to the cross-sectional



aspect ratio, shifting only 100 nm ( $\sim 525$  nm to  $\sim 625$  nm) with cross-sectional aspect ratio increasing from 1 to 5. In contrast, gold nanorods (with their aspect ratio defined as the ratio of the length and width) shift over a similar spectral range with an aspect ratio change of only 1 to 2.5 [168]. An additional increase in the nanobelt cross-sectional aspect ratio through synthesis may enable the plasmon resonance to be further tuned to the near infrared.

The results presented here describe a simple synthetic route towards an extended structure which exhibits sharp plasmon resonances for antisymmetric excitation across the nanobelt width. The nanobelts are single crystal structures with smooth surfaces which should minimize loss in plasmon propagation [41]. These propagating modes may be important in plasmonic waveguide applications. Since their energies are well defined it may be possible to optimize in- and out-coupling antennas for efficient light-to-plasmon conversion [169] enabling both efficient sub-wavelength waveguides and remote plasmon-enhanced spectroscopies such as surface-enhanced Raman scattering [170, 171]. These structures may also find applications as sub-wavelength plasmonic bandpass filters, only allowing light of specific wavelengths determined by the cross sectional geometry to be transmitted. A more detailed investigation of the propagation losses and the potential applications of these structures in plasmonics circuit applications is in progress. Furthermore, gold nanobelts may be considered for biological applications that currently employ tunable nanoparticles. The larger size of the nanobelts will provide a larger scattering cross section for imaging contrast or

detection, and nanobelts may offer unique interactions with cells and tissues due to their size and shape.

### **3.1.5 Conclusion**

In conclusion, we have developed an efficient chemical synthesis method for the fabrication of gold nanobelts with cross sectional dimensions smaller than 100 nm. We showed that the transverse plasmon modes of these extended structures are remarkably narrow and depend sensitively on the cross-sectional aspect ratio. These nanostructures may find applications in plasmonic circuits or nanomedicine.

## **3.2 Propagation and electromagnetic confinement in nanobelt**

### **3.2.1 Introduction**

The continued miniaturization of optical devices requires manipulation of light at the nanometer scale. Gold and silver nanostructures have been actively investigated for this purpose since they localize light to deep sub-wavelength dimensions through the formation of surface plasmons [151]. Surface plasmons can be described classically as the electromagnetic surface modes of metal nanostructures. Gold and silver nanoparticles exhibit localized surface plasmon resonances which lead to strong scattering and absorption at visible frequencies. Extended gold and silver nanowires support surface plasmons that propagate along their length. These propagating plasmons may serve as interconnects in future nanophotonic circuitry, where light is coupled into one end

of a nanowire and emitted at the other [39, 172, 173, 41, 6]. Looking beyond the classical description, propagating plasmons in nanowires are quasiparticles that retain the quantum information of the photons that generate them [174, 175, 176, 177]. Intriguing device architectures have been considered based on strong interactions between quantum emitters and plasmonic nanowires, including all optical transistors and single photon sources [178, 157]. However, the intrinsic losses in gold and silver at optical frequencies limit the propagation distances to several microns. Recent attention has therefore focused on characterizing the propagating modes, and how the propagation lengths depend on nanowire geometry, wavelength, dielectric environment, substrate, and metal crystallinity [41, 34, 179, 38, 35, 36, 180, 160, 40, 181].

Silver exhibits lower intrinsic losses than gold, and has been the focus on of most work on plasmon propagation in nanowires [41, 175, 180, 160, 40, 181, 182, 183]. The propagation can be directly measured with far field optics by focusing light at one end of the nanowire and observing emission at the other end. Chemically synthesized silver nanowires yield the longest propagation lengths, while lithographically fabricated wires offer the opportunity to investigate complex nanowire architectures. Reflections of surface plasmons at nanowire ends result in Fabry-Perot resonances within the nanowire which can be probed to extrapolate the wavelength and decay length of propagating plasmons [41, 38, 36, 180, 40, 181, 183]. Experimental results are in good agreement with both analytical solutions and numerical simulations using the measured dielectric function of silver.

There is much interest in thinner nanowires with a higher level of confinement to explore strong interactions between propagating plasmons and nearby quantum emitters [159]. However, smaller diameter nanowires also have shorter propagation lengths and weaker emission signals. In addition, gold nanowires may be preferred to silver for improved chemical stability and ease of functionalization, but the higher intrinsic loss in gold again leads to shorter propagation lengths. Plasmon propagation in the gold nanowires is therefore difficult to study with far field optics since the emitting nanowire end will be dim and imaged very close to the brightly scattering excitation end. Recent reports have found alternative methods to study gold nanowire propagation. Through excitation by total internal reflection at the surface of a prism, emission from lithographically fabricated gold nanowires was observed and spectrally analyzed. A Fabry-Perot model yielded a decay length of 2 to 4  $\mu\text{m}$  depending on frequency, although the Fabry-Perot fringes were not as clear as those for silver nanowires [38]. Propagation in gold nanowires has been observed by near field excitation of fluorophores. Fluorescence images of Coumarin 30 near the nanowires yields propagation lengths of 2.4 to 3.6  $\mu\text{m}$  [36]. Also, a method has been developed based on the near field bleaching of fluorophores and monitoring their recovery. This yields propagation lengths of 1.8  $\pm$  0.4  $\mu\text{m}$  at a wavelength of 532 nm [34] and 7.5  $\pm$  2.0  $\mu\text{m}$  at 785 nm [35]. With this method, the fundamental propagating mode ( $m=0$ ) is quenched by the fluorophore layer. The longer measured propagation length in these experiments was found to be due to a higher-order propagating mode ( $m=1$ )

which decays much slower than the fundamental propagating mode. All of these results are in reasonable agreement with theory, but each is either indirect or relies on models with some assumptions (such as reflectance coefficients of the nanowire ends) or some ambiguity regarding the propagating mode.

### 3.2.2 Propagation length measurements

Here we describe plasmon propagation in chemically synthesized gold nanobelts, which are gold nanowires with rectangular cross sections that are 25–150 nm in width and only 17–45 nm in height. The synthesized nanobelts range from 1 to 100  $\mu\text{m}$  in length [2], but usually display geometric defects or tapering if the nanobelts are much longer than 5  $\mu\text{m}$ . Gold nanobelts are attractive structures for plasmon propagation due to their single crystal gold structure, their relatively small cross-sectional size for strong confinement, and their elongated cross-sections, which may strengthen interactions with nearby emitters. Synthesis details can be found in Ref. [2], in which we recently reported the colorful plasmon resonances observed in these structures by dark-field microscopy that are due to an asymmetric excitation across the nanobelt width, which is tunable with cross sectional aspect ratio [2]. Both dark field and scanning electron microscope (SEM) images of nanobelts are displayed in Figure 3.5.

For plasmon propagation experiments, the nanobelts were imaged with an oil immersion 100X/NA=1.25 objective under epi-brightfield illumination with a white light emitting diode (LED). To observe plasmon propagation, a separate 850 nm LED

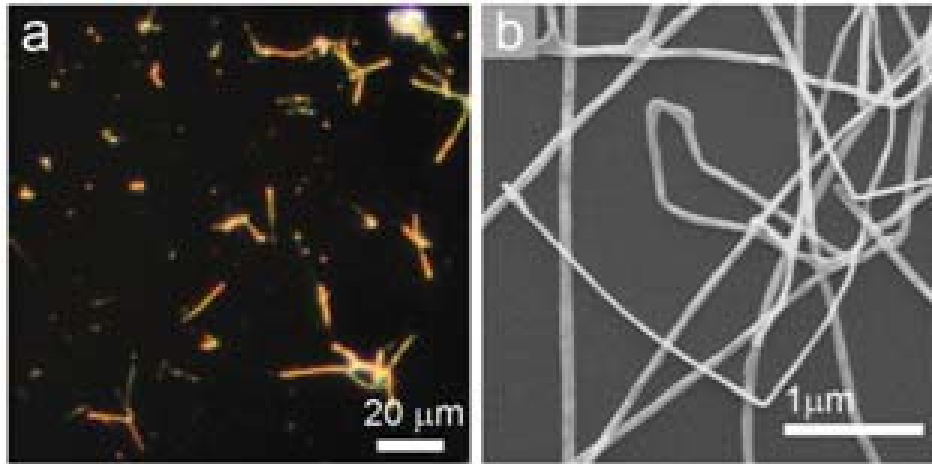


Figure 3.5 : Gold nanobelts deposited on a substrate and imaged a) by dark-field optical microscopy, and b) by scanning electron microscopy.

was positioned approximately 1 meter behind the objective lens and coupled in with a pellicle to produce a tightly focused spot in the object plane. The focused light was placed at one end of the nanobelt and light emission was observed at the other end, as seen for two short nanobelts in Figure 3.6. Efforts to generate propagation images with focused laser spot were unsuccessful due to the background of interference fringes and speckle patterns inherent to high coherence illumination, as we show in Figure 3.6. With low coherence LED illumination, the background is smooth and easily subtracted. To compare our measurements with previous reports on silver nanowires, the experiments were performed with 100 nm diameter silver nanowires synthesized following the extensive parametric polyol synthesis study by Coskun et al. [184]

The propagation length is defined here as the  $1/e$  decay length of the electromagnetic intensity inside the nanowire. It can be determined from measurements on gold

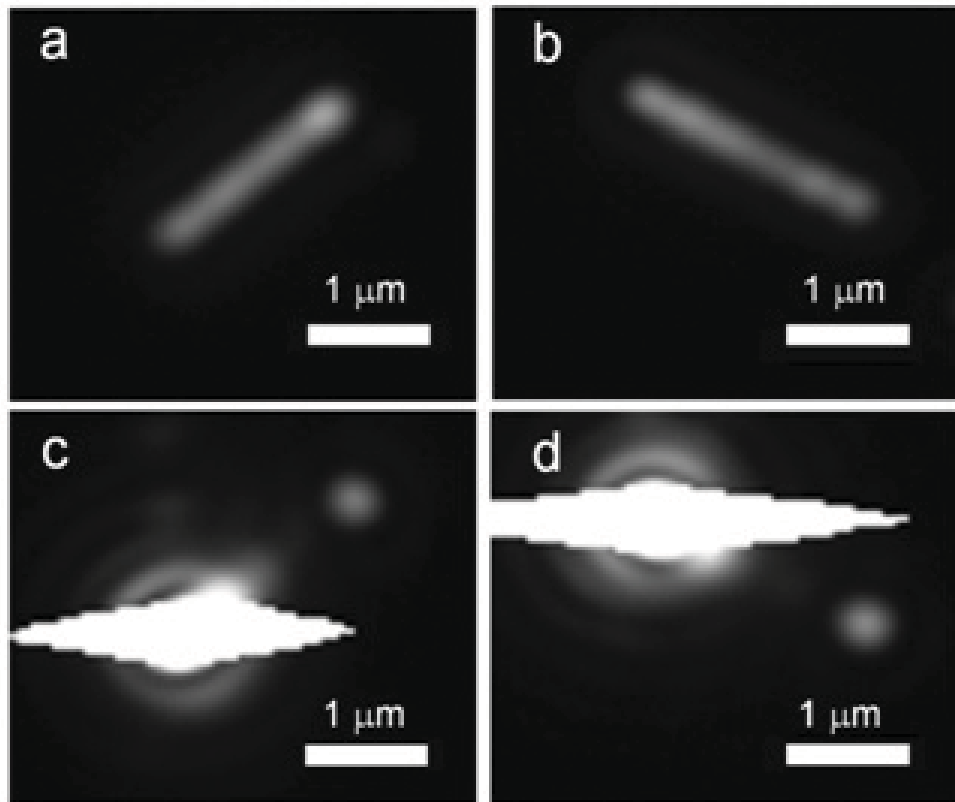


Figure 3.6 : Two gold nanobelts imaged with (a,b) epi-bright field illumination and (c,d) focused illumination to display propagation. The left nanobelt (a,c) is  $1.6 \mu\text{m}$  in length and the right nanobelt (b,d) is  $1.8 \mu\text{m}$ . The illumination wavelength is 850 nm.

nanobelts and silver nanowires with different lengths, assuming that the light emitted at the end is proportional to the intensity at that point. However, the data must be corrected for different nanowire diameters and nanobelt heights and widths since the size affects the quantity of light absorbed and re-emitted. Rather than correct the data with microscopic size measurements, we considered how three relevant processes scale with size for a cylindrical nanowire of radius  $r$ , as illustrated in Figure 3.7a. At the illuminated end the absorption of light will scale as  $r^3$  (roughly treating the

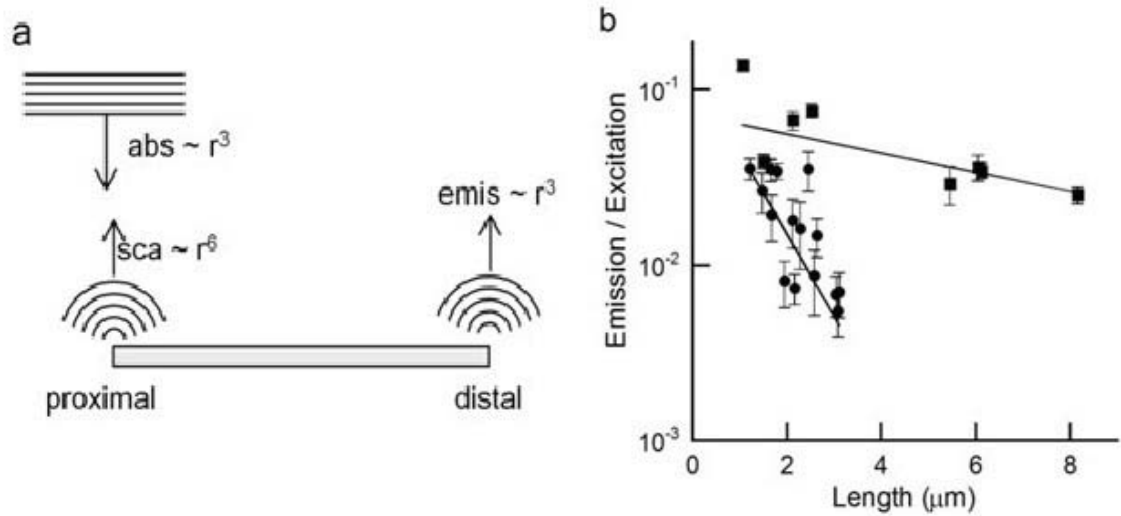


Figure 3.7 : The plasmon propagation length of gold nanobelts and silver nanowires. (a) A schematic that illustrates the scaling rationale. (b) Emission/excitation rates for gold nanobelts (●) and silver nanowires (■), with the exponential decay fits resulting in 0.94 and 8  $\mu\text{m}$  propagation lengths, respectively.

nanowire end as a sphere). Emission at the distal end will also scale approximately as  $r^3$ . Taken together, the entire process will scale as  $r^6$ . Direct scattering at the illuminated end also scales as  $r^6$  (again approximating the end as a sphere) and can be measured from the experimental images. We therefore scale the count rate of the emission by the count rate of the scattering from the excitation end for each nanobelt or nanowire. The ratio is plotted versus nanowire length in Figure 3.7 for both silver nanowires and gold nanobelts. Uncertainties were taken as the square root of the total counts for tip images and the nearby backgrounds. The data were fit to simple exponential decay by nonlinear least squares regression, weighting each data point by its uncertainty. The resulting propagation lengths were 8.0  $\mu\text{m}$  for silver nanowires



(with a 3.6 to 35  $\mu\text{m}$  95% confidence interval) and 0.94  $\mu\text{m}$  for the gold nanobelts (with a 0.61 to 2.1  $\mu\text{m}$  95% confidence interval).

Even using the emission/excitation ratio to account for different nanowire and nanobelt sizes, there is still significant scatter in the data and significant uncertainty in the resulting propagation lengths. Since each point in Figure 3.7 corresponds to a nanowire or nanobelt of different size, each point also corresponds to a different plasmon propagation length, and the resulting fit is therefore an average. The expected propagation lengths for thin cylindrical gold nanowires were calculated by solving the electromagnetic wave equation for an infinitely long right circular cylinder following Chang et al.[159] The resulting imaginary part of the wave vector gives the propagation length. The range of measured gold nanobelt propagation lengths are well matched to calculated propagation lengths of gold nanowires of similar cross sectional size.

### 3.2.3 Simulated properties of propagating modes

#### Propagation intensity and length

The gold nanobelt presented in Figure 3.8 was subject to detailed structural analysis by atomic force microscopy (AFM), and found to be 40 nm tall, 125 nm wide, and 5.5  $\mu\text{m}$  long. Figure 3.8a and Figure 3.8b show its dark-field and propagation images, respectively. Based on the nanobelt size and previous reports on propagating nanowire modes [35, 36], we expect two dominant propagating modes. The AFM

measurement of this particular belt is shown in Figure 3.8c. Figure 3.8d shows the calculated charge distribution for this nanobelt (top view) corresponding to both the fundamental  $m = 0$  mode and the higher-order  $m = 1$  mode. Only the fundamental mode exists for all nanowire diameters and is the strongest propagation mode for thinner nanowires [?, 185]. Figure 3.8e shows the FDTD-calculated magnitude of the plasmon Poynting vector along the length on a logarithmic scale. This directional energy flux is proportional to the emission that would take place if the belt were to terminate at that given length. The linearity of the logarithmic Poynting vector as a function of propagated distance shows that no Fabry-Perot resonances is present in the belt, as expected, since the simulated nanobelt is semi-infinite long. The propagation length, the reciprocal of the absolute slope of the straight line of Poynting vector, is fitted to be 1.9 and 17.5  $\mu\text{m}$ . The simulations also predict that light couples strongest to the  $m = 0$  mode, but that it decays more rapidly along the length than the  $m = 1$  mode. This leaves the  $m = 1$  mode stronger at longer lengths. For this nanobelt geometry, the cross-over occurs at  $\sim 7.6 \mu\text{m}$ .

FDTD calculations show that for this experimental geometry, the  $m = 0$  mode results in emission at the nanobelt tip that is polarised parallel to the belt length and the  $m = 1$  mode emission is polarised transverse to the belt, which makes sense based on the charge distribution in both cases. To identify the propagation modes experimentally, a calcite beam displacer was placed in the imaging path. This element spatially separates the two polarizations of the signal. The displacer was rotated to

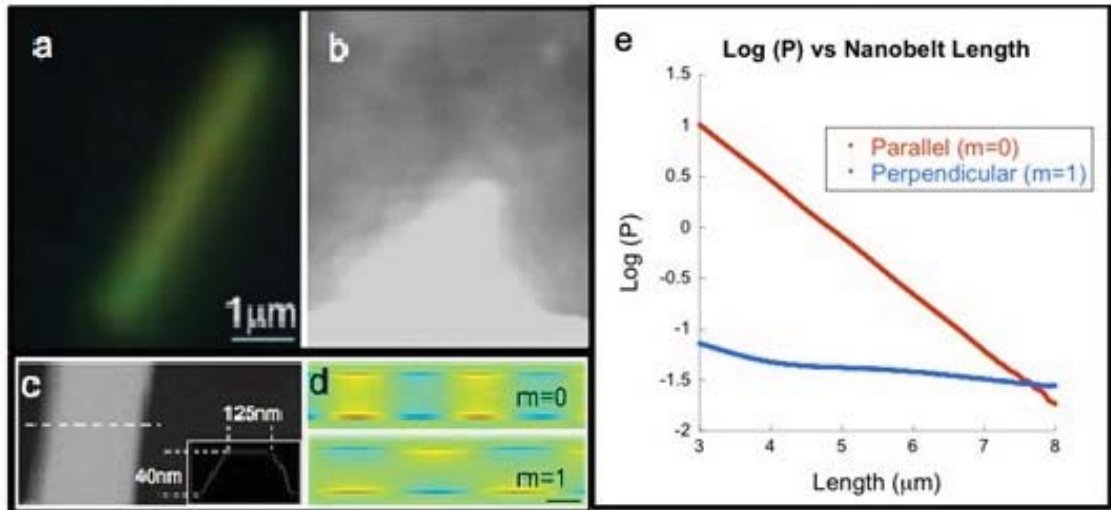


Figure 3.8 : (a) Dark-field image of 5.5  $\mu\text{m}$  long, 125 nm wide, 40 nm tall gold nanobelt. (b) Plasmon propagation image of the same nanobelt, illuminated at one end with an 850 nm LED. (c) AFM of the nanobelt cross section. (d) Calculated charge distribution for the fundamental  $m=0$  mode and the higher-order  $m=1$  mode (scale bar = 100 nm). (e) Calculated logarithmic of Poynting vector for two propagating modes along a 125nm x 40nm nanobelt. For the  $m = 0(1)$  mode, the polarization of the incident illumination is parallel (perpendicular) to the belt length, with symmetric (antisymmetric) induced surface charge across the belt width.

the orientation of the nanobelt on the sample so that the resulting images were light polarized parallel and perpendicular to the nanobelt. Figure 3.9a and Figure 3.9b show displaced propagation images for 2.4  $\mu\text{m}$  and 5.8  $\mu\text{m}$  long gold nanobelts. For the short nanobelt (Figure 3.9a), there is strong  $m = 0$  emission (polarized along the nanobelt), while the  $m = 1$  emission (polarized perpendicular to the nanobelt) is present but barely detectable. For the longer nanobelt (Figure 3.9b) the  $m = 0$  emission is still strong, but the  $m = 1$  emission is a larger fraction of the total. This behavior follows the calculated prediction in Figure 3.8e. Highly uniform nanobelts of this length are difficult to find, but a comparison of the  $m = 0$  and  $m = 1$  signals from

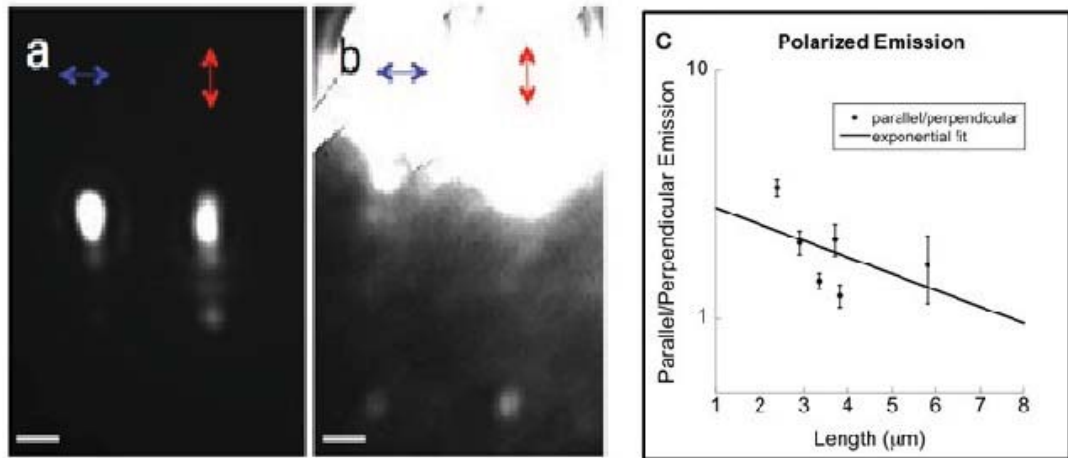


Figure 3.9 : Plasmon propagation through a  $2.4 \mu\text{m}$  long (a) and a  $5.8 \mu\text{m}$  long (b) gold nanobelt for polarizations perpendicular (blue) and parallel (red) to the belt. (scale bar =  $1\mu\text{m}$ ) (c) The ratio of the parallel to perpendicular components of the emission for several nanobelts.

nanobelts at several lengths reveals that the ratio of parallel to perpendicular light emitted at the nanobelt tip decreases exponentially as predicted by the simulations (Figure 3.9c). An exponential fit of these data give a cross-over length of  $7.7 \mu\text{m}$ , which is in good agreement with the simulations.

### Mode pattern

For further insight into the propagation lengths of the  $m = 0$  and  $m = 1$  modes, we investigated their cross-sectional field intensity and corresponding heat distribution which were then calculated using FDTD (Figure 3.10). The  $m = 0$  mode generates higher intensity fields than the  $m = 1$  mode, but most of the field intensity exists outside the nanobelt in the dielectric medium. The loss is mostly due to heat generation

due to the field just inside the metal, which can be difficult to predict based on static charge distributions like Figure 3.8d. However, the heat plots in Figure 3.10 make it clear that the  $m = 0$  mode also has higher losses, especially in the thin metal surface layers where the field intensity are much more significant than deep inside the body, which is why it has a shorter propagation length than the  $m = 1$  mode.

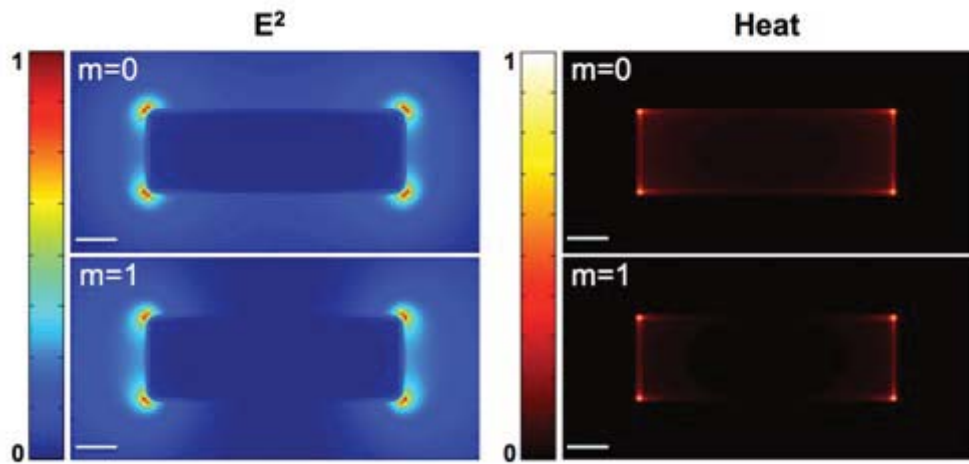


Figure 3.10 : Cross-sections of normalized field and heat intensity (arbitrary units) in a 125 x 40 nm gold nanobelt for both the  $m=0$  and  $m=1$  modes. Scale bar = 20 nm.

For plasmonic waveguides there is a trade-off between high field confinement, which strengthens interactions with nearby emitters, and propagation length, which is important for transmitting information [186]. As the cross-sectional diameter decreases, the quantum confinement increases due to tighter localization of the electromagnetic field, but the propagation length decreases due to an increased fraction of the field inside the metal. For 2D strip waveguides a figure of merit (FOM) was pro-

posed by Buckley et al that accounts for both confinement and propagation length: [127]

$$M_1^{2D} = 2\sqrt{\frac{\pi}{A_e}}L_{prop}, \quad (3.1)$$

where the mode area  $A_e$  is defined as the area bounded by the closed  $1/e$  field magnitude contour relative to the electric field maximum, and the  $L_{prop}$  is propagation length. In favor of a high FOM, the  $m = 1$  mode outperforms the  $m = 0$  mode for the studied gold nanobelt, because the former has a  $L_{prop}$  of  $\sim 17.5 \mu\text{m}$ , about 9 times as large as the latter, while they have comparable mode areas. The calculated figure of merit for  $m = 1$  mode is  $\sim 1300$ , better than those reported (around 300) for strip waveguides at the wavelength of our interest (850 nm). The strip waveguides were microns in width, so they have longer plasmon propagation lengths, but lower confinement. When strong coupling interactions are desired, the mode area is of primary importance. The mode area for the  $125 \times 40 \text{ nm}$  nanobelt is calculated to be around  $2400 \text{ nm}^2$ , which is only 48% of its cross section area and is roughly two orders of magnitude smaller than the mode area of the larger strip waveguides. Our calculations also show that a 100 nm diameter cylindrical silver nanowire, as a comparison, has a mode area of around  $10,300 \text{ nm}^2$  (131% of its cross section area), a propagation length of  $\sim 9.5 \mu\text{m}$ , and a resulted FOM of 335. Such an improved strong confinement achieved with gold nanobelts may be useful for studying interactions between plasmons and quantum emitters bridging the gap between plasmonic and

quantum systems.

### 3.2.4 Conclusion

In summary, we have directly observed plasmon propagation in thin gold nanobelts by focusing light at one end and imaging the emission from the other. Problems with imaging short propagation lengths and weak emission signals were overcome through the use of low coherence LED illumination. Emission measurements from multiple nanobelts were scaled for different sizes to yield a fitted propagation length of  $0.94 \mu\text{m}$  at a wavelength of 850 nm. The calculations and experiments also demonstrate that with increasing nanobelt length, a higher-order mode takes over due to its longer propagation length. Evidence of this cross over was seen in analysis of the emission polarization. The emission was also found to strongly favor near infrared frequencies, agreeing with an analytical model of a cylindrical gold nanowire. The high confinement factor, with Figure-of-Merit as high as around 1300, for these structures represent an important step towards studying strong interactions of propagating plasmons with nearby quantum emitters, given the reduced cross-sectional size and the facile surface chemistry of gold nanobelts.

### **3.3 Stimulated emission of SPP in nanowire: dye-assisted propagation length enhancement**

#### **3.3.1 Introduction**

Subwavelength confinement, control and manipulation of light is essential for realization of integrated nanophotonic and optoelectronic applications [187, 188, 6]. To this effect, noble metal nanowires (NWs) offer excellent solution as transport vehicle for subwavelength-confined optical signal [38, 33, 41, 180, 189], owing to their ability to support surface plasmon polaritons (SPPs) [190], which are collective oscillations of conduction band electrons on the metal surface. However, SPP propagation suffers substantial intrinsic (Ohmic) and extrinsic (e.g., radiative) losses that seriously limit the application potential of these nanostructures [38]. Although there have been some important efforts to loss compensation and amplification of SPPs in planar waveguide structures [73, 191, 192, 193, 57], no such attempt have been made, so far, to achieve gain of SPPs propagating in a subwavelength nano-waveguide. Here, we report the first demonstration of gain into SPP modes in chemically prepared silver nanowires, obtained by optical pumping of a dye-doped polymer acting as dipolar gain medium. An obvious compensation of the subwavelength propagation losses was achieved in this study, which is an important stepping stone towards low-loss subwavelength plasmonics.

The lossy propagation in various plasmonic waveguides poses a major challenge



for their application in integrated photonic and other devices, and therefore, there has been a considerable recent interest in the SPP amplification and compensation of the propagation losses [191, 192, 193, 57, 194, 195, 58]. Amplification and stimulated emission of weakly confined SPP modes supported on metal surface of thin film waveguides were demonstrated in attenuated total-reflection setups by prism-decoupling techniques [57, 194, 195, 58]. For a quantum-dot-doped polymer-loaded gold film, Grandidier et al. showed a significant enhancement in propagation length of SPPs excited in the IR region (1550 nm), by optically pumping the quantum dots using a 532 nm laser [192]. In another study, the net optical gain was estimated by measuring amplified spontaneous emission for a metallic thin film embedded in a fluorescent polymer [193]. Amplification of ultra-confined plasmonic or hybrid modes in nanoscale cavity and subsequent laser-like emission were demonstrated in metal-semiconductor [196] or metal-dielectric nanostructures [197], and recently, in bowtie nano-antenna [198].

Most demonstrations of SPP gain were either based on indirect techniques like prism decoupling, amplified spontaneous emission etc [193, 57, 194] or through some laser-like behavior of nanoscale cavity modes [196, 197, 198]. A direct measurement of net amplification of long-range SPPs propagating in a thin gold stripe has been demonstrated De Leon and Berini [73], where they were able to fully compensate the SPP propagation losses and record an amplified signal at the output end. However, so far there has been no such effort to demonstrate SPP amplification or gain in the

metallic NWs, neither any literature on SPP stimulated emission in these waveguides, despite the fact that plasmon waveguiding in silver and gold NWs is well-documented [38, 33, 41, 180, 189, 36, 35, 34].

Although silver and gold nanowires (NWs) are attractive candidates for subwavelength waveguiding [38, 33, 41, 36, 35, 34], the SPP propagation is also significantly lossy in these nanostructures. For example, recent estimation of SPP propagation length by fluorescence-based mapping techniques [36, 35, 34] have revealed that the plasmonic field intensity decays to 1/3 of its initial value for a 10  $\mu\text{m}$  long propagation in a silver NW [36], and almost 20 times in a gold NW for comparable propagation [34]. Thus, SPP gain will be crucial for the use of these NWs in integrated photonic applications or building nanoscale optical components. Also, as silver NWs can demonstrate Fabry-Perot type resonance [41, 180, 189], a net amplification of SPPs can potentially lead to the realization of subwavelength plasmonic laser with NW acting as a laser cavity.

### 3.3.2 Experiment

In this work we report a straightforward demonstration of gain-assisted propagation of confined SPP modes in single silver NWs, by optically pumping the associated dye-doped polymer acting as gain medium. The experimental design of the excitation of SPPs for individual NWs, with and without pumping the dye, and estimation of SPP gain is schematically described in Figure 3.11. Detailed measurement protocol has

been delineated in Methods section. Briefly, chemically prepared silver NWs were deposited on Rhodamine 640 (R640) -doped PMMA layer (gain medium) coated on clean glass coverslip, and the sample was excited from bottom, as shown in Figure 3.11. The SPPs were launched by exciting one end of a NW with 633 nm laser and the optical output due to decoupling of SPPs into light emission/scattering from the opposite (output) end of the wire was monitored (Figure 3.11A). The measurement was then repeated by combining SPP excitation at 633 nm with optical pumping of the dye layer by 514 nm laser (pump laser), where the former was focused on NW-end and the latter (pump laser) in the middle of the NW. The gain into the SPP modes was achieved by high power ( $0.1 \sim 0.8 \text{ kW/cm}^2$ ) pumping of the dye layer with 514 nm laser, and estimated by measuring and comparing the output signal intensities with and without pumping the dye.

A direct experimental manifestation of optical gain into the SPP modes has been illustrated in Figure 3.12, which summarizes the result of a representative gain experiment. Figure 3.12A shows the NW image recorded in CCD under optical excitation at the left-end with red (633 nm) laser at low power ( $15 \text{ W/cm}^2$ ). Figure 3.12B shows the image of the same NW, which is now illuminated in the middle with the green (514 nm) laser at a high power ( $0.35 \text{ kW/cm}^2$ ). Here, both ends of the NW lights up due to outcoupling of the spontaneous emission of the dye. A third image, whence both red and green (pump) lasers were on, was recorded (Figure 3.12C) using similar conditions (integration time, laser powers etc) as before and a much brighter output

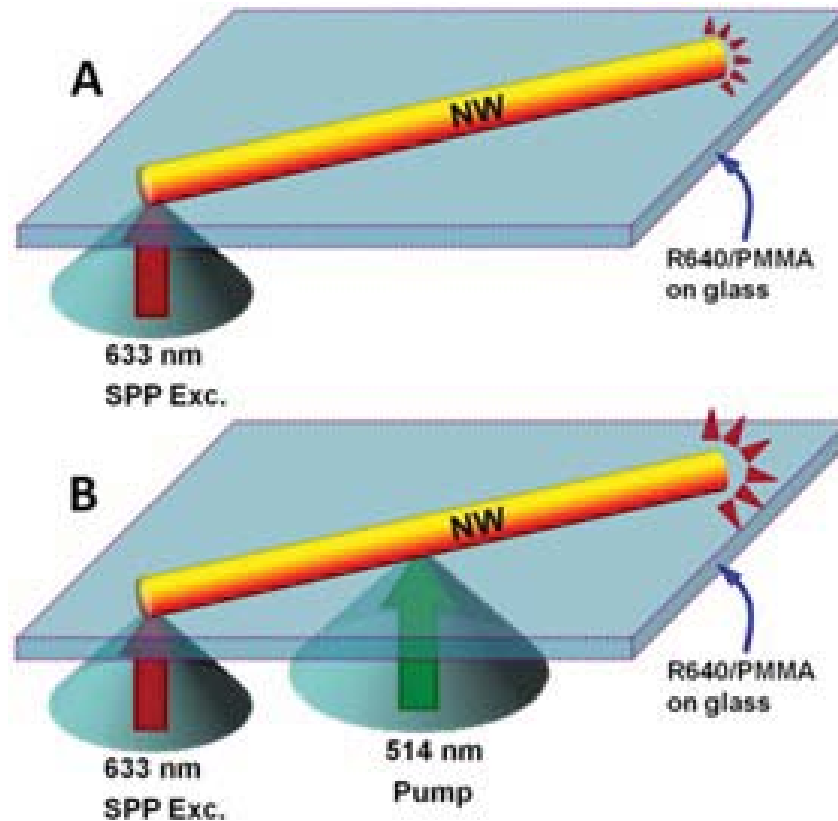


Figure 3.11 : Schematic description of the gain experiment: (A) The SPP in a silver NW, placed on top of a gain medium (a dye-doped polymer), is excited by 633 nm laser at left end and the output from the opposite end (right end) is monitored. (B) An additional laser at 514 nm, now focused in the middle of the NW, optically pumps the gain layer below the NW, resulting in a significant enhancement of output signal from the right end.

signal is observed in this case of combined excitation compared to the previous cases of individual red or green excitations. The enhanced output signal for combined excitation is a direct outcome of dye-assisted gain into propagating SPP modes of the NW.

A 20% enhancement of the optical output signal solely due to the SPP modes was observed for the above NW, as estimated from the intensity cross-sections of

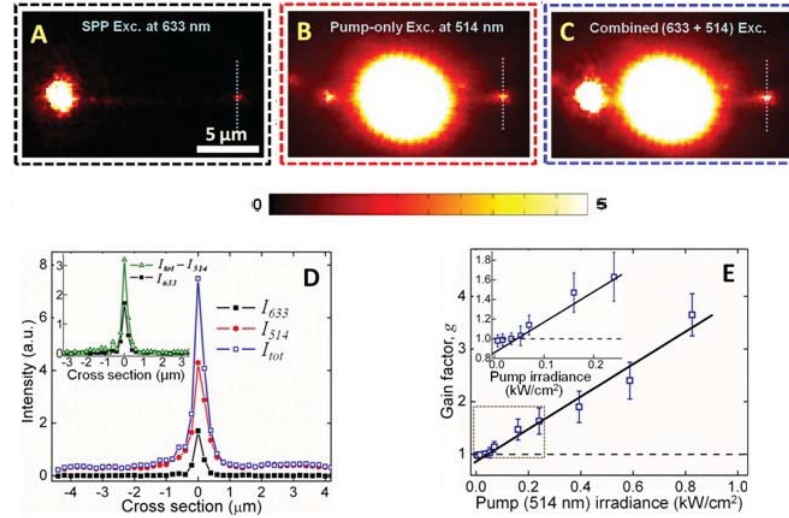


Figure 3.12 : A representative gain experiment: (A) A CCD image of a silver NW exciting at left end by 633 nm CW laser at  $15 \text{ W/cm}^2$  (integration time 0.3 s). (B) The same NW imaged by exciting with CW 514 nm (pump) laser at  $0.38 \text{ kW/cm}^2$  in the middle. The optical output from both ends of the NW reveals outcoupling of dye spontaneous emission. (C) Combined excitation with both 633 nm (SPP excitation) and 514 nm (pump) lasers, with same power and integration time as before. A strong output emission is observed in this case. (D) The plot of intensity cross sections, shown by dashed lines in AC, of the output signal for the respective images:  $I_{633}$ ,  $I_{514}$  and  $I_{tot}$  correspond to (A) 633 nm, (B) 514 nm and (C) combined excitations, respectively. Inset shows that  $I_{tot} - I_{514} > I_{633}$ , signifying enhancement of output signal corresponding to SPP modes, thereby revealing gain into SPP modes. (E) Pump power (irradiance) dependence of the gain factor,  $g$ , with linear fit to the region  $g > 1$ . Inset: The threshold gain behavior is depicted more clearly by highlighting the region of low pump irradiance (dotted box).

the output signal (Figure 3.12D) through the maximum intensity channel for each of three cases shown in Figures 3.12A–C. It should be noted here that the output intensity corresponding to combined excitation with red and green laser ( $I_{tot}$ ) has the contribution from the spontaneous emission noise ( $I_{514}$ ) in it (Figure 3.12D), which means that net output of the SPP modes under pumping =  $I_{tot} - I_{514}$ . Thus the condition for gain is  $I_{tot} - I_{514} > I_{633}$ , as revealed in inset to Figure 3.12D, which

substantiates the fact that gain is provided by the optically pumped dye layer in terms of stimulated emission into the SPPs modes. So, we define the relative gain factor as

$$g = \frac{I_{tot}^{max} - I_{514}^{max}}{I_{633}^{max}}, \quad (3.2)$$

where the superscript max to each term in the right-hand side Eqn. 3.2 stands for the corresponding maximum value of respective parameter. From Eqn. 3.2 it is obvious that when  $g = 1$ , we have  $I_{tot} - I_{514} = I_{633}$ , i.e., no net gain into propagating SPPs.

Further evidence of the gain due to stimulated emission into the SPP modes was obtained from the linear dependence of the gain factor,  $g$ , on pump laser power (irradiance), as shown in Figure 3.12E. The value of  $g$  at each given pump power was estimated by averaging the individual  $g$  values for 8~10 NWs. A clear threshold corresponding to the pump irradiance = 0.05 kW/cm<sup>2</sup> for the onset of gain, given by the condition  $g > 1$ , is observed from Figure 3.12E and more clearly depicted in the inset. The observation of a threshold point and a linear gain behavior above the threshold (when  $g > 1$ ) is the signatures of stimulated emission [73, 192, 57], which is consistent with our assignment.

### 3.3.3 Simulation

Electromagnetic simulation was performed using finite difference time domain (FDTD) method. The simulation assumed a silver nanowire with 12  $\mu$ m length and 100 nm

diameter, placed on a 250 nm thick dielectric layer with permittivity of  $\varepsilon' = 2.25$ , that was illuminated by a 633 nm Gaussian beam with 300 nm width, which was transmitted through the dielectric layer and focused on one end of the NW. For the dielectric function of silver, the tabulated values by Johnson and Christy were used [141]. The emitted energy flow from the opposite end (output end) of the NW was simulated as a distribution surrounding the output end of the NW and at the bottom of the NW, i.e., the interface between gain layer and the dielectric layer to faithfully reproduce the experimental configuration. To represent the experimental gain medium, an imposed imaginary part ( $\varepsilon''$ ) of the permittivity was introduced into the aforesaid dielectric layer and the E-field intensity, as well as the energy flow, around the output end was calculated with and without such gain medium. Using this model the relative enhancement of output signal with respect to zero gain condition ( $\varepsilon'' = 0.0$ ) was calculated for a number of  $\varepsilon''$  values of increasing magnitude.

The enhancement of output signal intensity due to optical gain is shown in Figure 3.13. For a silver NW lying on top of a gain layer that assumes an effective dielectric function with small negative imaginary part, and, the energy flux and E-field intensity distribution surrounding its output end was simulated by illuminating the NW at one (input) end with 633 nm Gaussian beam. A stronger field enhancement in presence of a gain layer with imaginary permittivity,  $\varepsilon'' = -0.003$  than that in a simple dielectric, for which  $\varepsilon'' = 0$ , was observed from the both top-view (Figure 3.13A,B) and cross-sectional (Figure 3.13C,D) plots, predicting a 20% amplification over the output signal

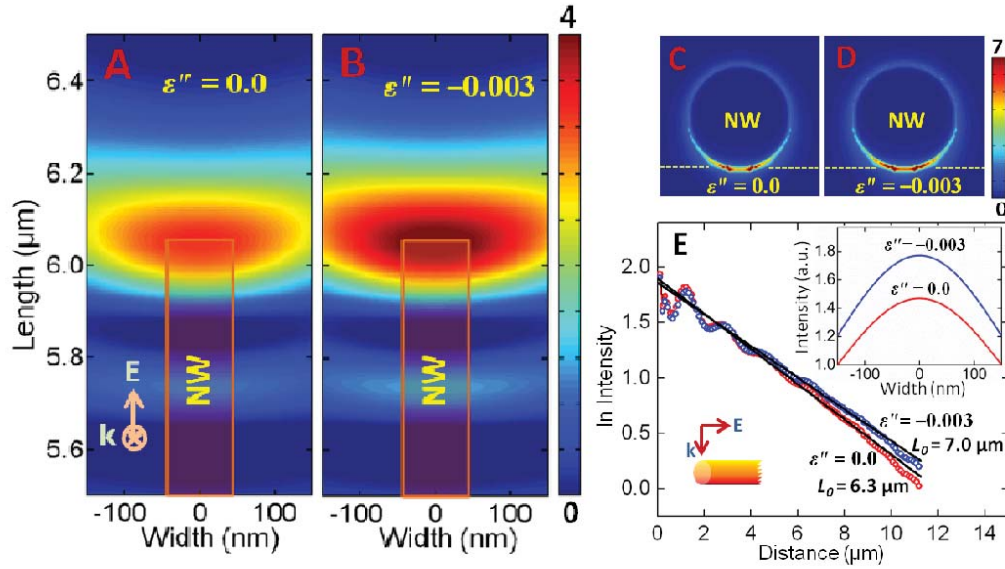


Figure 3.13 : FDTD simulation of SPP gain for a  $12 \mu\text{m} \times 100 \text{ nm}$  silver NW lying on top of a dielectric/gain layer with real permittivity,  $\epsilon' = 2.25$ . (A) Top-view of energy flux (normal to the substrate) distribution around the output-end of a silver NW under 633 nm laser excitation at input end (not shown) when there is no gain, i.e., imaginary permittivity,  $\epsilon'' = 0$  and (B) the same with a gain medium corresponding to  $\epsilon'' = -0.003$ . (C) The E-field intensity from the cross-sectional view of the NW-end without gain ( $\epsilon'' = 0$ ) and (D) with gain ( $\epsilon'' = -0.003$ ). Here the dashed line indicates the upper boundary of the gain medium. Stronger E-field enhancement with the gain layer is visible from both pictures. (E) Decay of SPP field intensity along the long NW axis and associated propagation lengths without and with the gain medium. The inset shows the E-field intensity cross-sections without (black) with (red) gain layer, revealing a 20% enhancement of output intensity for the given ( $\epsilon'' = -0.003$ ) gain medium.

without gain (inset to Figure 3.13E). The simulation also demonstrates a subsequent enhancement of SPP propagation length due to the aforesaid gain (Figure 3.13E), suggesting gain-assisted compensation of SPP propagation losses.



### 3.3.4 Conclusion

In summary, we have successfully demonstrated the gain-assisted propagation of SPPs in single silver NWs where the optical gain into SPP modes was provided by a laser-pumped dye layer. Our result shows that as much as half of the SPP propagation losses are compensated using simple dye-based gain medium. With further improvements like minimizing the dye photobleaching by using a circulating dye solution instead of a dye-doped polymer etc and/or some optimization of the gain medium, like using a lossless dielectric host etc, it might be possible to achieve a net loss compensation or even amplification SPP in these nanowires. This achievement will be crucial for development of nanoscale plasmonic amplifiers and subwavelength lasers, among other applications, and for ultimate realization of low-loss plasmonic nanomaterials for all-optical miniaturized devices.

## Chapter 4

### Plasmon-heated bubble generation

#### 4.1 Experimental characterization

##### 4.1.1 Motivation

Recently an ensemble of nanoparticles has been employed in a macroscopic-scale solar energy harvesting and steam generation which has promising future applications in medical treatment, sanitation, distillation and industrial usage [32]. The achievement of relatively high efficiency (24%) of solar energy transferring into heat-up steam, as well as a low-threshold incident light intensity ( $\sim 10^6 W/m^2$ ), has inevitably intrigued a fundamental scientific interest in understanding the physical bubble-generating process further at microscopic scale, i. e. the evolution of the light-induced vapor generated out of single nanoparticle into the formation of bubbles of larger scale.

When an Au nanoparticle in a liquid medium is illuminated with resonant light of sufficient intensity, a nanometer scale envelope of vapor -a nanobubble- surrounding the particle, is formed [31, 199, 200, 201, 202]. This is the nanoscale onset of the well-known process of liquid boiling, occurring at a single nanoparticle nucleation site, resulting from the photothermal response of the nanoparticle. Here we examine steam generation at an individual metallic nanoparticle in detail. Incipient nanobub-

ble formation is observed by monitoring the plasmon resonance shift of an individual, illuminated Au nanoparticle, when its local environment changes from liquid to vapor. The temperature on the nanoparticle surface is monitored during this process [203, 204, 205, 125], where a dramatic temperature jump is observed as the nanoscale vapor layer thermally decouples the nanoparticle from the surrounding liquid. The subsequent formation of freely diffusing macroscopic bubbles results from the coalescence of the individual, nanoparticle-bound vapor envelopes into larger, micron-scale bubbles: the contributions of incident light intensity and nanoparticle density to this process are quantified. These studies provide the first direct and quantitative analysis of the evolution of light-induced steam generation by nanoparticles from the nanoscale to the macroscale, a process that is of fundamental interest for a growing number of applications [201, 206, 207, 208, 209, 210, 211, 212].

Noble metal nanoparticles, when illuminated at a wavelength corresponding to their plasmon resonance, can serve as highly efficient localized heat sources at the nanometer length scale [202, 213, 214, 215]. This is a unique property that enables numerous applications across a range of fields including energy [25, 216, 217], chemical catalysis [201, 206], macroscopic steam generation [207, 208], protein imaging [209, 210], and biomedicine [211, 212]. Several aspects of this general property have been studied, including vapor formation in a large ensemble of metallic nanoparticles under CW and pulsed laser excitation, as well as single bubble formation and superheating [31, 202, 214]. However, it is a significant experimental challenge to determine the

precise properties of the liquid-vapor phase transition at the nanoparticle surface, such as the temperature, internal pressure, and size of the vapor envelope –the nanobubble–formed upon resonant laser excitation. Quantifying these properties at the single nanoparticle level, for direct comparison with a theoretical picture that takes into account the energy distribution in the illuminated nanoparticle-fluid-vapor system, is crucial to provide an accurate picture of precisely how this process occurs.

In the present section, we scrutinize the process of plasmon-induced steam generation, from generation of a vapor nanobubble at an individual nanoparticle surface to the formation of a microscopic bubbles. We examine the localized surface plasmon resonance (LSPR) and the surface-enhanced Raman scattering (SERS) spectrum of para-mercaptoaniline adsorbate molecules on an individual Au nanoparticle, performed during controlled resonant laser excitation both below and above the threshold required to induce local vapor formation. This combination of local optical measurements allows us to determine the key microscopic parameters of this system, such as the nanobubble radius around the nanoparticle surface, the internal nanobubble pressure, the nanoparticle surface temperature, and their dependence on incident light intensity. The transition from local, nanoparticle-bound vapor layers to free-floating, micron-scale bubbles is also studied. The formation of macroscopic bubbles results from the coalescence of nanobubbles that form at the individual nanoparticle sites. Here we quantify the energetics of macroscopic bubble formation based on the incident laser power and the areal density of nanoparticle nucleation sites. This series of

experiments provides a detailed picture of the multistage steam formation process by resonant excitation of metallic nanoparticles which will be useful for the development of applications, both at the nano- and macroscale, of this unique phenomenon.

#### 4.1.2 Experimental evidences of formed nanobubble

Gold nanoparticles were chemically synthesized, then immobilized with an ultrathin layer of poly(4-vinyl pyridine)(PVP) onto a transparent dielectric substrate at the bottom of a microchamber (Fig. 4.1a). These nanoparticles were dispersed onto the substrate surface at a very dilute areal coverage, nominally 1 nanoparticle/ $100 \text{ m}^2$  (Figure 4.1b shows a SEM image of a sample of deposited nanoparticles at significantly higher areal density, for visualization purposes; more details in the Methods section). The microchamber was designed to be optically probed by dark field microscopy (for LSPR spectroscopy) during simultaneous illumination by a CW heating laser beam. Alternatively, the CW resonant heating laser also served as the Raman pump laser for SERS studies of heating at the nanoparticle surface, from which an effective temperature at the nanoparticle surface could be monitored. The chamber could be evacuated for studies in ambient air, or filled with DI water (total fluid volume =  $6 \text{ cm}^3$ ).

Dark-field optical microspectroscopy [218, 219] was used to detect changes in the single nanoparticle LSPR scattering spectrum upon resonant laser illumination (Fig. 4.1c). The measured LSPR spectrum in air was found to peak at 563 nm. When

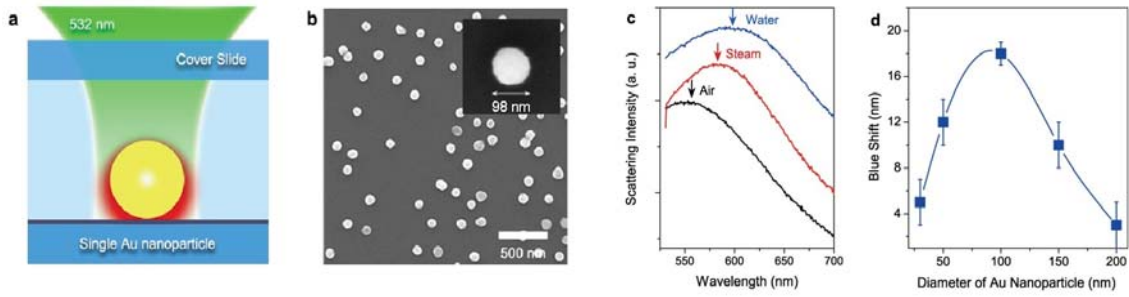


Figure 4.1 : Light-induced generation of a nanobubble at a single nanoparticle surface. (a) Schematic showing illumination and plasmonic heating of an individual Au nanoparticle on the transparent glass substrate floor of our fluidic microchamber. (b) Scanning electron microscope (SEM) images of a sample with a dense coverage of Au nanoparticles randomly distributed on the glass substrate, and a typical nanoparticle (inset). (c) Scattering intensities of a single 100-nm diameter nanoparticle in air (black), water (blue), and an envelope of water vapor produced by laser illumination (red). The blueshift corresponds to formation of a finite vapor envelope of nanometer scale thickness around the nanoparticle. Spectra are shifted vertically for clarity. (d) Dependence of nanobubble-induced LSPR blueshift on Au nanoparticle diameter, with a maximum shift observed for a nanoparticle diameter of 100 nm. The error bars represent the nanoparticle-to-nanoparticle variation observed in the LSPR blueshift.

the microchamber was filled with DI water with a temperature of 20 °C the LSPR was observed to redshift to 598 nm. The redshift of 35 nm is in good agreement with the redshift obtained from a Mie calculation for the same particle embedded in air compared to that in water at 20 °C ( $\epsilon=1.778$ ). When a 532 nm excitation laser beam with 25 mW power, focused to a  $1 \mu\text{m}^2$  beam spot, was incident on a nanoparticle, the LSPR was observed to blueshift to 581 nm. This incident intensity level ( $\sim 2.5 \times 10^{10} \text{ W/m}^2$ ) corresponded to the threshold intensity for the observed shift. It is worth knowing that there is a difference of a few orders of magnitude for the incident light intensity between the reported nanoparticle-ensemble experiment [32] and our single-particle experiment. Possible reasons accounting for such a difference

may include the multiple-scattering effect absent in the single-particle experiment, as well as the infrared absorption of water molecules. The observed blueshift implies a decreased refractive index of the medium directly surrounding the nanoparticle, which we interpret as corresponding to the formation of a water vapor envelope surrounding the nanoparticle.

When illuminated by a CW laser, an Au nanoparticle is heated due to nonradiative plasmon decay into inelastic electron collisions. For low incident laser power, heat from the nanoparticle is transferred into the surrounding solution, resulting in a steady-state thermal gradient.<sup>3</sup> At higher incident powers (25 mW and above), a thin layer of surrounding water vaporizes and forms a nanobubble which provides a transient thermal barrier, reducing subsequent heat transfer into the surrounding solution. The size of the nanobubble will be determined by energy balance: it expands until the energy dissipation into the liquid becomes equal to the energy absorbed by the nanoparticle from the incident laser light. The observed blueshift is far too large to be consistent with merely heating the liquid surrounding the nanoparticle: for a gold nanoparticle of equivalent size immersed in 100 °C water ambient, only a 3 nm blueshift would be observed (Fig. S1, Supporting Information in Ref. [3]).

The rate of plasmon-induced heat generation in a nanoparticle is proportional to its optical absorption cross-section multiplied by the incident optical intensity [31, 201]. Since the absorption efficiency (absorption cross-section divided by the nanoparticle cross-section  $\pi R_{NP}^2$ ) varies with nanoparticle size, the dependence of the

blueshift on nanoparticle size was also investigated (Fig. 4.1d). A maximum blueshift of 18 nm was detected for Au nanoparticles of 100 nm, decreasing quite strongly for both smaller and larger nanoparticles. This trend clearly shows an optimal nanoparticle size for steam generation that corresponds to maximum absorption efficiency at 532 nm (See Fig. S2, Supporting Information in Ref. [3]). For a single gold NS, the optimal size of around 100 nm diameter corresponds to a single-particle heating power of  $\sim 5 \times 10^{-4}$  W. The reason for the decreased blueshift for large nanoparticle radii is the redshift of their LSPR with increasing size. The error bars reflect variations in the resonance blue-shift measured for different particles with the same nominal size, which we attribute to the size and shape variation of chemically synthesized Au nanoparticles in each size range, indicating a sensitivity of the steam nucleation threshold to details of nanoparticle morphology.

A second evidence of the presence of the nanobubble is obtained by direct measurements of the temperature at the nanoparticle surface when steam generated. We performed SERS on individual 100 nm diameter Au nanoparticles. The nanoparticles were functionalized with a monolayer of para-mercaptoaniline (pMA, 0.3 nm thick), shown previously to yield a robust SERS signal from individual nanoparticles under resonant laser pumping [125]. The SERS measurements were performed in the water-filled microchamber.

Optical vibrational pumping was observed, showing an evolution of the Raman response of the system as a function of incident laser power (Fig. 4.2). While several



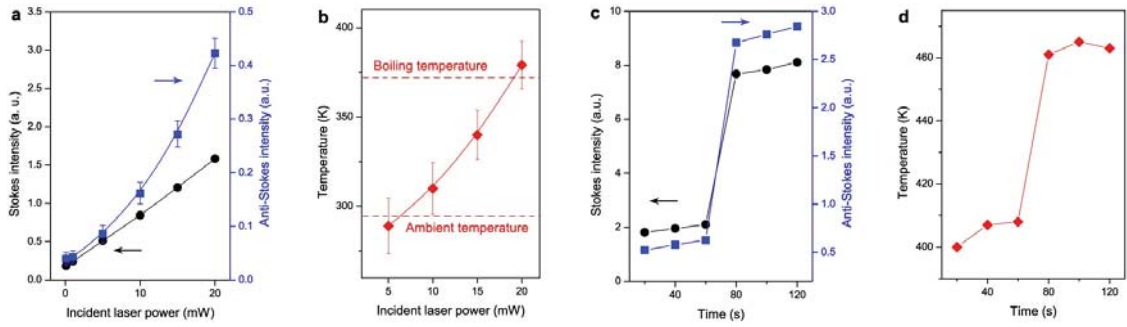


Figure 4.2 : Temperature at the Au nanoparticle surface during the steam generation process. (a) Power dependence of the Au-S Stokes (black dots) and anti-Stokes (blue squares) mode amplitudes at  $\sim 390$   $\text{cm}^{-1}$  for a pMA-coated single Au NP (100 nm diameter) as a function of incident laser power. (b) Temperature obtained from the mode amplitudes in a and Eqn. 4.1, as a function of incident pump laser power. Error bars in panels a and b indicate the uncertainty in the signal due to the low anti-Stokes signal levels in this range of incident laser intensities. (c) Time dependence of Stokes (black dots) and anti-Stokes (blue squares) signals with 25 mW laser excitation. A large intensity jump occurs after 60 s of laser excitation. (d) Temperature jump obtained from the mode amplitudes shown in c and Eqn. 1 occurring after 60 s of 25 mW laser excitation.

spectral peaks were observed in the Stokes spectrum, our analysis focused on the  $390 \text{ cm}^{-1}$  mode, corresponding to the Au-S stretching mode associated directly with chemical bond between the adsorbate molecules and the Au nanoparticle surface. A quadratic dependence of the anti-Stokes intensity on incident power is observed, as expected in the optical pumping regime (Fig. 4.2b) [220]. A temperature was extracted from the ratio of the Stokes and anti-Stokes intensities for this vibrational mode using [203, 205, 125]

$$\frac{I_{AS}}{I_S} = A \left( \frac{E_0 + E_{ph}}{E_0 - E_{ph}} \right)^4 \exp\left(-\frac{E_{ph}}{k_B T}\right), \quad (4.1)$$

where  $I_{AS}$  and  $I_S$  are the anti-Stokes and Stokes Raman intensities for the mode, and

$E_0$ ,  $E_{ph}$  is the energy of photon and phonon respectively.  $A$  is a correction factor that accounts for the ratio of cross-sections for Stokes and anti-Stokes Raman scattering.

At low incident laser power (1 mW), the temperature obtained, assuming  $A = 1$ , was 289 K, corresponding very closely to the ambient temperature of the water prior to laser illumination (290 K). We therefore assumed that the cross-sections for Stokes and anti-Stokes scattering are similar, and set  $A = 1$  for our subsequent analysis. Stokes and anti-Stokes spectra were obtained from the nanoparticle as incident laser power was increased, and the integrated areas of the  $390\text{ cm}^{-1}$  mode peaks were converted to effective temperatures using Eqn. 1 (Fig. 4.2b). As the incident laser power was increased, the temperature at the nanoparticle surface obtained in this manner was observed to increase smoothly and reversibly from 289 K to 379 K ( $\pm 20$  K). This reversibility implies that for this temperature range, corresponding to the nanoparticle surface temperature ranging between its initial ambient value and the boiling point of water ( $\sim 373$  K), the nanoparticle surface responds directly to the incident power, without any delay effects that would indicate a dramatic change such as the formation of a vapor envelope around the nanoparticle, or a change in nanoparticle morphology or surface chemistry.

When the incident laser power was increased to 25 mW, however, corresponding to the earlier observed threshold interpreted as nanobubble formation, the Raman spectra exhibited large changes in intensity. Both the Stokes and Anti-Stokes intensities for the  $390\text{ cm}^{-1}$  vibrational mode exhibit a dramatic jump after 60 seconds

of illumination at this power level (Fig. 4.2c). From the Stokes and anti-Stokes data and Eqn. 4.1, we see that the observed spectral changes correspond to a rapid temperature increase from 400 K to 465 K ( $\pm 3$ K) (in this regime of higher pump power levels, the error bars are within the symbols used to plot the data). Since this incident power regime is consistent with our interpretation of nanobubble formation observed in the LSPR measurements, we interpret this rapid temperature increase as a further heating of the Au nanoparticle surface within the nanobubble, due to the decrease in heat transfer between the nanoparticle and the liquid medium after nanobubble formation. The final steady-state temperature of 465 K observed is determined by an energy balance between the incident power and the heat transfer across the nanobubble/water interface, and likely corresponds, within uncertainties, to the Au nanoparticle surface temperature within the nanobubble.

#### 4.1.3 Theoretical analysis

A scheme of bubble generation is shown in Fig. 4.3a. When the surface plasmon of the nanoparticle is excited by a laser, some of the incident energy dissipates elastically, into scattered photons. The dominant portion of the remaining energy is absorbed by the nanoparticle, causing inelastic electron collisions, resulting in heating. The calculated heat source density, that is, the generated Joule heating power per unit volume for a 100 nm diameter Au nanoparticle, immersed in water and illuminated by a linearly polarized plane wave with the incident E field along the  $y$  axis, is shown

in Fig. 4.3b. The hottest regions occur at the north and south poles where the wave-vector enters and leaves the sphere. This is quite distinct from the regions of the nanoparticle surface with the largest plasmon-induced field enhancements, which occur on the sides of the sphere aligned with the incident E field (Fig. 4.3c). The origin of this discrepancy is two-fold. First, the surface current driven by the tangential electric field is largest at the north and south poles of the particle due to the dipolar-like electric field distribution. Second, the electric field is normal to the particle surface at its east and west sides, and is decreased by a factor of  $1/\epsilon_{Au}$  inside the metal because of the requirement of electric displacement continuity at the particle surface. Based on a concentric geometry where the effect of the dielectric substrate is neglected (Fig. 4.3a, inset), our Au nanosphere with radius  $R_{NP}$  is assumed to be surrounded by a concentric water vapor bubble of radius  $R_B$ .

Since the observed blueshift of the nanoparticle surface plasmon is less than that for an infinite embedding medium of water vapor, we can use this information to estimate the bubble radius  $R_B$ . Within an electrostatic dipole model [221, 222], the redshift of the dipolar surface plasmon resonance is proportional to the relative permittivity change:

$$\frac{\Delta\lambda_B}{\Delta\lambda_w} = \frac{\Delta\epsilon_B^{eff}}{\Delta\epsilon_w} \equiv \frac{\epsilon_B^{eff} - \epsilon_{air}}{\epsilon_w - \epsilon_{air}}, \quad (4.2)$$

where  $\Delta\lambda_B$  is the experimental redshift of the plasmon resonance for a nanoparticle in a finite nanobubble,  $\Delta\lambda_w$  is the redshift of the plasmon resonance in water relative to its value in air,  $\Delta\epsilon_B^{eff}$  is the permittivity increase for a finite nanobubble

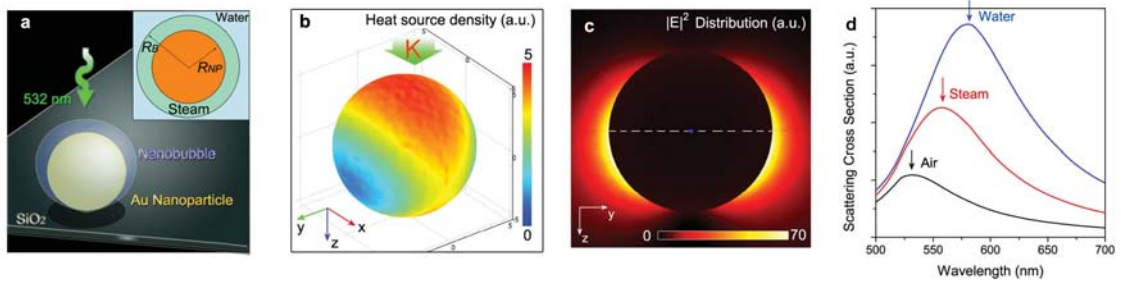


Figure 4.3 : Nanobubble theoretical modeling. (a) Schematic of nanobubble formation around a nanoparticle under 532 nm resonant laser illumination. Inset: geometry of our model where the nanobubble is a dielectric spacer layer of outer radius  $R_B$  between the nanoparticle surface (with radius  $R_{NP}$ ) and the surrounding water medium. (b) Simulated heat-source density for an illuminated 100 nm diameter Au nanoparticle immersed in water. (c) Near-field intensity enhancement for a 100 nm diameter Au nanoparticle in water, relative to incident field intensity. The polarization of the incident E-field is along the y-axis, with the wave vector  $k$  along the z-axis. (d) Mie calculation of the scattering cross-sections for a 100 nm diameter Au NP in air (black), surrounded by a steam bubble with outer radius  $R_B=60$  nm (red), and in water (blue). The simulation for the steam layer is in good agreement with the experimental observations in Fig. 4.1c.

relative to air ambient, and  $\Delta\epsilon_w$  is the permittivity increase for water relative to air ambient. The superscript *eff* denotes the effective permittivity change experienced by the nanosphere. Assuming the geometry depicted in Fig. 4.3a, and adopting the values of  $\epsilon = 1.0$  for steam (verified below) and  $\epsilon = 1.77$  for water at room temperature, we performed Mie calculations [75, 74] to obtain theoretical scattering spectra for different values of the bubble radius. From comparison of the measured value of  $\Delta\lambda_B/\Delta\lambda_w=0.51$  (Fig. 4.1c) to the calculated spectra, we deduce that the thickness of the vapour shell around a single Au nanoparticle is nominally 6.5 nm ( $R_B = 56.5$  nm) (See Supporting Information, Figure S4 in Ref. [3]). The LSPR

measurement provides strong and consistent evidence that a nanosize bubble is generated. The spectral shift, calculated from Mie theory, agrees with the experimental scattering spectra using the concentric steam-water shell model where  $R_B = 56.5$  nm (Fig. 4.3d).

With the nanobubble radius determined, the temperature and pressure of the confined steam within the nanobubble can be estimated as follows. We assume that the system reaches steady state after bubble formation, as suggested in Fig. 4.2c and 4.2d. At equilibrium, the Laplace pressure due to the surface tension at the water-steam interface is balanced by the vapor pressure of the steam, which is a function of temperature given by the Clausius-Clapeyron Relation (CCR). Hence, we have

$$C \exp\left(\frac{h}{k_B T_s}\right) = p_0 + 2\gamma(T_s)/R_B, \quad (4.3)$$

where  $C$  is a constant,  $h$  is the enthalpy of water evaporation,  $k_B$  is Boltzmann constant,  $T_s$  is the temperature of saturated steam inside the bubble,  $p_0$  is the atmospheric pressure (1 atm), and  $\gamma$  is the surface tension coefficient (See Section 4.3). The calculated steam temperature  $T_s$  within the nanobubble is 464K, with a corresponding internal pressure of 1.49 MPa (14.7 atm). At this pressure and temperature, the permittivity of steam is close to 1.0, confirming the previous assumption made in the determination of the steam layer thickness.

The energy-conservation law must be observed when the system spatially within  $R_{eff}$  is steady, meaning that the absorbed power must be equal to the dissipated power. By applying this law as well as the Fouriers law of heat transfer, we obtain

the temperature difference ( $T_{NP} - T_s$ ) estimated to be approximately 72 K (See Supporting Information Text S1 in Ref. [3] for the detailed calculation), resulting in an estimated nanoparticle surface temperature of  $T_{NP}=536$  K. The estimated average temperature of the molecular layer at the gold-vapor interface was found to be nominally 500 K, which is close to the experimental value of 465 K obtained from our SERS measurements.

#### 4.1.4 From nanobubble to microbubble

To study the transition from discrete nanobubbles localized onto their parent nanoparticles to macroscopic, freely-floating bubbles, several types of measurements were performed for Au nanoparticle samples of varying interparticle distances under 532 nm laser illumination. A time series of images under these conditions resulting in the formation of a 10  $\mu\text{m}$  bubble is shown in Figure 4.4a. After illumination ( $t=10.6$  sec), a 1  $\mu\text{m}$  bright spot (bubble) appears in the image, and after  $t=13.0$  sec it has expanded to a bubble of 10  $\mu\text{m}$  diameter. Energetically, the size of the bubble should saturate when heat dissipation through the vapor/water interface is equal to the heat generated by nanoparticle absorption. The origin of these macroscopic bubbles appears to be the coalescence of nanobubbles initially produced at the individual Au nanoparticles. A proposed process for macroscopic bubble formation is illustrated in Fig. 4.4b. At high incident powers, nanobubbles are generated around individual nanoparticles. If the interparticle spacing is sufficiently small, the nanobubbles ap-

pear to attract each other and rapidly coalesce, resulting in the formation of a stable micron-sized bubble. Similar attraction-and-coalescence has also been observed for the macroscopic bubbles studied.

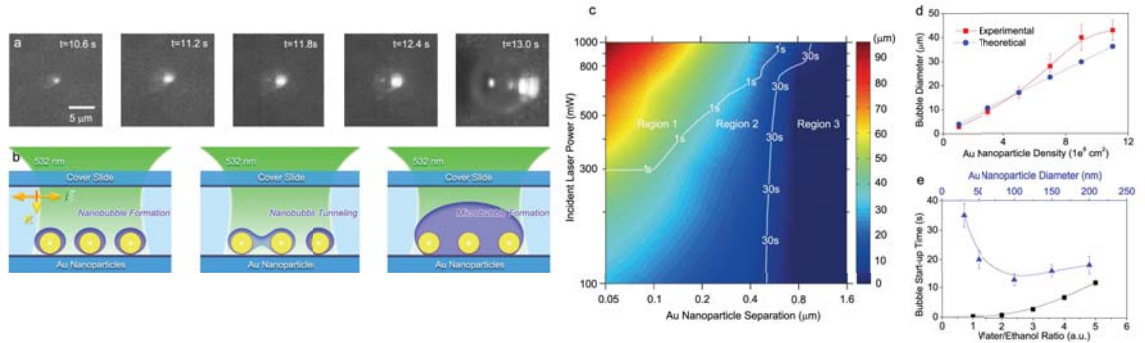


Figure 4.4 : Coalescence of nanobubbles into micron-sized bubbles. (a) Time series of microbubble generation. The nanoparticle areal density is  $3 \times 10^8 \text{ cm}^{-2}$  (average NP-NP separation  $\sim 0.5 \mu\text{m}$ ) and the incident laser power is 75 mW with a beam spot diameter of  $5 \mu\text{m}$ . (b) Schematics depicting microbubble formation due to the coalescence of neighboring nanobubbles produced on individual Au nanoparticles. (c) Experimental diagram of the dependence of final bubble size and formation time on incident laser power and average nanoparticle separation, where the white contours represent the formation time, and the colors indicate final bubble diameter. (d) The influence of nanoparticle areal density on generated bubble size with an incident power of 75 mW. (e) Bubble formation time versus water/ethanol ratio (with 100 nm Au nanoparticles, black squares), and nanoparticle size (blue triangles) for the water only. The incident laser power is 75 mW with a spot size of  $5 \mu\text{m}$ . Error bars of (d) and (e) indicate uncertainty induced by variations in nanoparticle morphology and nanoparticle separation distances.

Both the final size of the bubble and the formation time (the interval between the turn on of the laser and the micron-sized bubble being observed) are functions of both incident power and nanoparticle separation. This is shown in the contour plot in Figure 4.4c, where the line represents the formation time, and the color mapping



represents the final bubble size (with a  $5 \mu\text{m}$  incident laser spot diameter). Generally, higher incident powers ( $\geq 400 \text{ mW}$ ) and shorter interparticle separations ( $\leq 0.4 \mu\text{m}$ ) result in a shorter formation time and a larger bubble size, as illustrated in Region 1 of Fig. 4.4c. In Region 2, with lower power ( $\leq 300 \text{ mW}$ ) or longer interparticle separation (for instance  $\geq 0.4 \mu\text{m}$ ) than Region 1, stable microbubbles can also be observed, but a significantly longer time is needed for the bubble to expand to an observable size, and its final size is smaller than for the Region 1 parameters. Nanobubbles generated with even lower incident power levels may be less likely to form, or may form as only partial vapor envelopes around the individual nanoparticles, which may explain the power dependence of the formation time (Fig. 4.4c) from Region 1 to Region 2, even for the smallest interparticle separations. The power required for microbubble formation in the small interparticle separation regime is between 300 to 500 mW, agreeing well with our theoretical estimate of 450 mW for this process (See Supporting Information, Text S2 in Ref. [3]). For very long interparticle separations ( $> 0.8 \mu\text{m}$ , Region 3), no microbubble is generated even at the highest incident power level, because nanobubble coalescence is inhibited for such large interparticle distances.

The size of a microbubble is controlled by the nanoparticle areal density and the incident laser power. For an incident power level of 75 mW, the dependence of microbubble diameter on nanoparticle density increases linearly (Fig. 4.4d), a measurement that agrees with our theoretical prediction (see Supporting Information,

Text S2 in Ref. [3]). The essential reason is that for a fixed laser spot diameter ( $5 \mu\text{m}$ ), the total heat generated within a microbubble is proportional to the nanoparticle density, while the heat dissipation across the vapor/water interface is proportional to the bubble radius  $R_B$ , not the bubble area  $R_B^2$ . A larger bubble is thus generated when the total energy absorbed by the nanoparticle ensemble is increased. The experimental deviation from the theoretically predicted linear trend, for large bubbles, may be explained by small contributions of collective effects, such as multiple scattering, or changes in nanoparticle absorption efficiency due to microbubble formation.

For a more general perspective on microbubble coalescence, we also examined this process in a water-ethanol mixture instead of pure water, as a function of relative ethanol concentration and nanoparticle diameter. The incident laser power was 75 mW with a spot size of  $5 \mu\text{m}$ . We observed that the microbubble formation time is approximately linear with increasing water/ethanol ratio. However, it is significantly enhanced for small ( $\sim 50 \text{ nm}$  diameter) nanoparticles (Fig. 4.4e). For water/ethanol ratios  $\leq 1$ , the nanobubble is generated more easily because the ethanol decreases the boiling point of the liquid mixture, resulting in more rapid microbubble formation. The reason why small Au nanoparticles exhibit a long bubble formation time is that, for a given nanoparticle surface density, the interparticle separation of 30 nm nanoparticles is larger than that for 200 nm nanoparticles, resulting in a decreased nanobubble coalescence efficiency as previously discussed.

## 4.2 Local field weighted effective medium method

### 4.2.1 Introduction

As discussed previously, plasmon-heating has been a hot research topic in recent years [28, 29, 30, 31], because it provides an energy-transfer path into heat at nanoscale, by exciting plasmonic modes in noble metals which decay largely into Joule heating. Various applications of plasmon-heating have been proposed, such as photodetection [8], cancer treatment [79, 9, 11, 12, 13], and the generation of nanobubbles [28, 29, 30, 31, 32]. In these applications, nanobubble generation has been investigated widely, since the generated bubble is a promising material for medical surgery [10], electricity generation from solar-energy, water cleaning [32], etc.

Discussed in the previous section, characterizing the steam bubble generated at nanoscale has been a long time fundamental challenge to the nano-science community. While various techniques, such as pulsed laser [28], X-ray diffraction [30] etc., have been applied in the study and characterization of the heating dynamics of nanobubbles based on transient heat transfer process, our have developed and discussed a novel characterization approach of the plasmon-heated nanobubble originated from continuous heat transfer in Section 4.1. In this approach, first of all, the source of exciting the plasmon on the nanoparticle (NP) is a continuous-wave (CW) laser which allows the establishment of meta-stable state in which the size and location of the generated nanobubble are meta-stable and the heat due to excitation of plasmon is dissipated through the thin bubble layer in equilibrium. Such meta-stable state al-

lows for a dark-field single-particle back-scattering measurement [2, 223] which can last for tens of seconds. Next, from the optical-spectra measured for gold nanospheres (NS) embedded in air, in water without bubble and in water with surrounding bubble respectively, the size of generated nanobubble is determined from the change of peak positions of plasmonic resonances of the metal NS (Section 4.1). Such changes indicate changes of local dielectric environment around the NP and hence serve as a convincing evidence of the formation of nanobubbles. Furthermore, the bubble radius can be determined by matching the relative peak shifts. Such peak position shifts can be simulated in rigorous Mie [74, 75] or brutal-force Finite-Difference Time-Domain (FDTD) calculations where the bubble radius is varied until perfect match. Finally, upon the calculation of bubble radius, the pressure and temperature inside the bubble can be derived according to a classical heat equilibrium theory.

The merit of an effective medium method (EMM) is important within this approach. Although the brutal force calculations, such as Mie, FDTD or other applicable numerical methods for solving dynamic Maxwell equations, are deemed accurate and sufficient enough for obtaining the bubble size, they have inborn drawbacks: the bubble radius is a prerequisite input in the calculations and the searching of optimal bubble radius for matching the peak shift is in fact a parameter-sweeping optimization. This optimization, no matter how fast and automatic it is, represents a tedious indirect solving process which hinders conceptual understanding of the interplay between the surface plasmon and the whole surrounding dielectric environment. By

contrast, as we will show below, by treating the ambient dielectric environment as a whole averaged one, the merit of an EMM, and by employing the dipolar approximation, we greatly simplify the relation between peak shift and the bubble size which then becomes directly solvable. Therefore, a clear picture of the interplay among surface plasmon, local field and ambient dielectrics results.

In this section, we present an EMM based semi-analytical modeling to solve the bubble radius directly rather than parameter-sweeping as we did by using Mie calculations. Unsatisfied with the accuracy of conventional EMM in our scenario, we propose a local-field weighted effective medium method (LFWEMM) which incorporates the weights of the local electric field in volumetric averaging of the local dielectric responses. We will show that as a derivative of the conventional mean field theory, the LFWEMM is more accurate than other EMMs when benchmarked with rigorous Mie calculations, suggesting that the inclusion of near-field weighting is beneficial and promising when applying EMM in a field-localized scenario, commonly seen near excited surface plasmon.

#### **4.2.2 Results and discussion**

Plasmon heating has been applied to generate bubbles. When a metal NP is illuminated by a light source, for example, pulsed or CW source, a collective oscillation of electron cloud, or as known as plasmon, can be excited. Upon the excitation, the plasmon can lose its energy by radiation, as well as dissipation through electron scat-

tering. These two energy-losing mechanisms are characterized as radiative damping and intrinsic damping respectively. The latter mechanism determines that the energy dissipated is transferred into the Joule heat, and the temperature of the NP is increased as a result. Within linear response regime, the power of heating, i.e. the absorbed power by the NP, is proportional to the intensity of the illumination, by a factor of the absorption cross section of the NP. It is also well known that when a NP is immersed in liquid, e.g. water in this paper, and is illuminated by a light source with strong enough intensity, the heating power will be high enough to increase the temperature of the NP to a level that evaporate the liquid surrounding the NP.

It is worth mentioning that intuitively, while strong enough intensity is a requisite condition, an efficient bubble formation is also dependent on geometric factors. A sphere-like heat source density distribution, combined with a spherical shape of the NP, is favorable to bubble formation. Therefore, here we mainly discuss the bubble formation through the excitation of dipolar resonances of gold NS which is expected to be most favorable to the bubble formation.

As we showed in Fig. 4.1 in Section 4.1, with the peak well separated from those of the other two, the observed spectrum for bubble indicates that the bubble is of medium size, neither too large nor too small. Otherwise it would be too close to the left or the right one to be distinguishable. It is also worth to mention that the blueshift of the spectrum for bubble with respect to that for water is not caused by heated-up water surrounding the NS, which is illustrated in the inset of Fig. 4.5. By

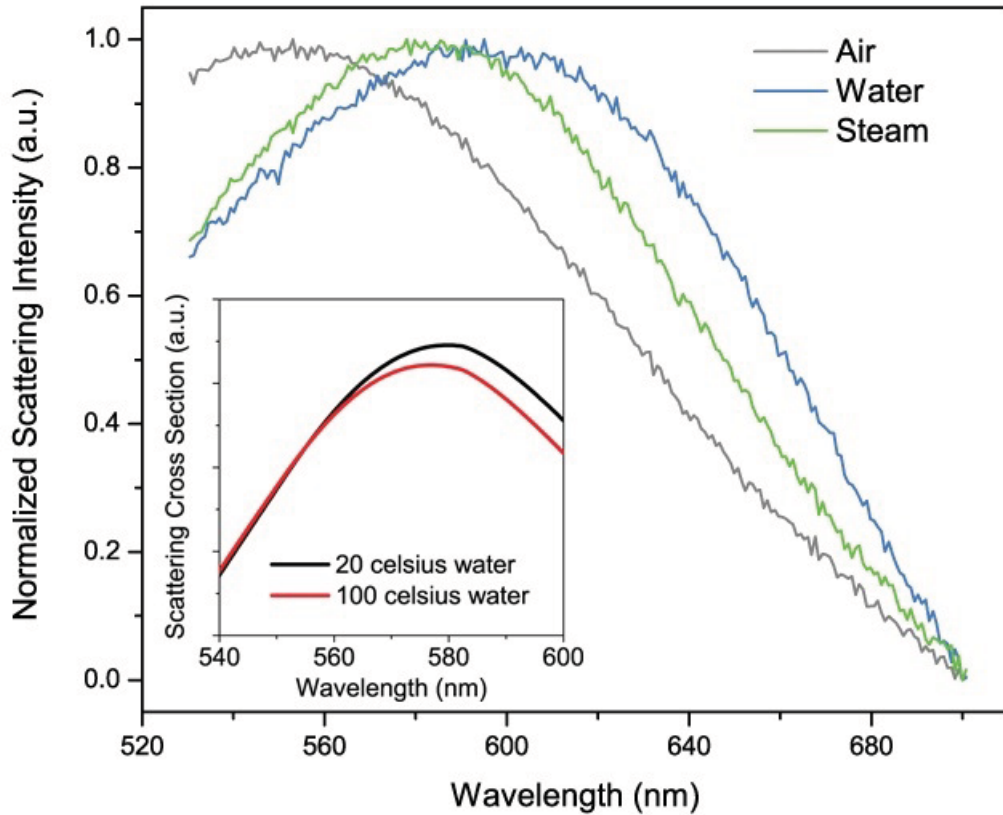


Figure 4.5 : Experimental optical spectra for a gold nanosphere (NS) with 50 nm radius when embedded in air (grey), steam (green), water (blue). This is essentially the normalized version of Fig. 4.1c for better peak positioning. Inset shows the Mie-calculated blueshift due to water temperature of 100 °C (red) compared with 20 °C (black). The resonance peak of the NS in 100 °C water has a  $\sim 3$  nm blueshift compared with the one in 20 °C water.

ruling out such a possibility, it is safe to attribute the spectral blueshift with respect to water ambience to the formation of bubble.

Determined from the optical spectrum, the redshift in wavelength of the dipolar peak for a specific dielectric ambience with respect to air ambience is theoretically proportional to the difference between the two permittivities, according to plasmon hybridization theory [224, 4] or dipolar coupling models [221, 222]. For a dielectric

ambience of bubble which is not too large to completely isolate the NP from water, the NP should see an effective permittivity which is averaged from the contribution of water and steam. This effective permittivity is described by Eq. 4.2.

To employ an EMM, we next introduce a sphere with cut-off radius  $R_{eff}$ , by knowing the interaction between excited plasmon and ambient dielectric is short-range. Outside the cut-off radius  $R_{eff}$ , the dielectric material is assumed to have no interaction with the NP plasmon. To determine  $R_{eff}$ , we performed a set of Mie (or FDTD) calculations in which the bubble radius  $R_B$  is increasing from the NP radius  $R_{NP}$  until a critical value was met. At such critical  $R_B$ , the scattering spectrum obtained should have the same peak position as the one for NP embedded in air. Thus the  $R_{eff}$  is calibrated as this critical  $R_B$ . Figure 4.6 schematically shows the model we used and corresponding notations, and also exemplifies the calculated scattered electric near-field distribution around the gold NP with radius 50 nm when illuminated by a linear-polarized plane wave near resonance.

### **Characterization of bubble size by LFWEMM: local field is important**

To start the characterization process, we next applied an EMM in the finite spherical volume, defined by  $R_{eff}$ . In such a volume, only two materials are present: water and steam. In a typical EMM, water (or steam) is assigned a weight for averaging the permittivity and such weight is hence definitely related to the peak shifts due to the existence of a bubble. Please refer to Methods for details of insertion of a



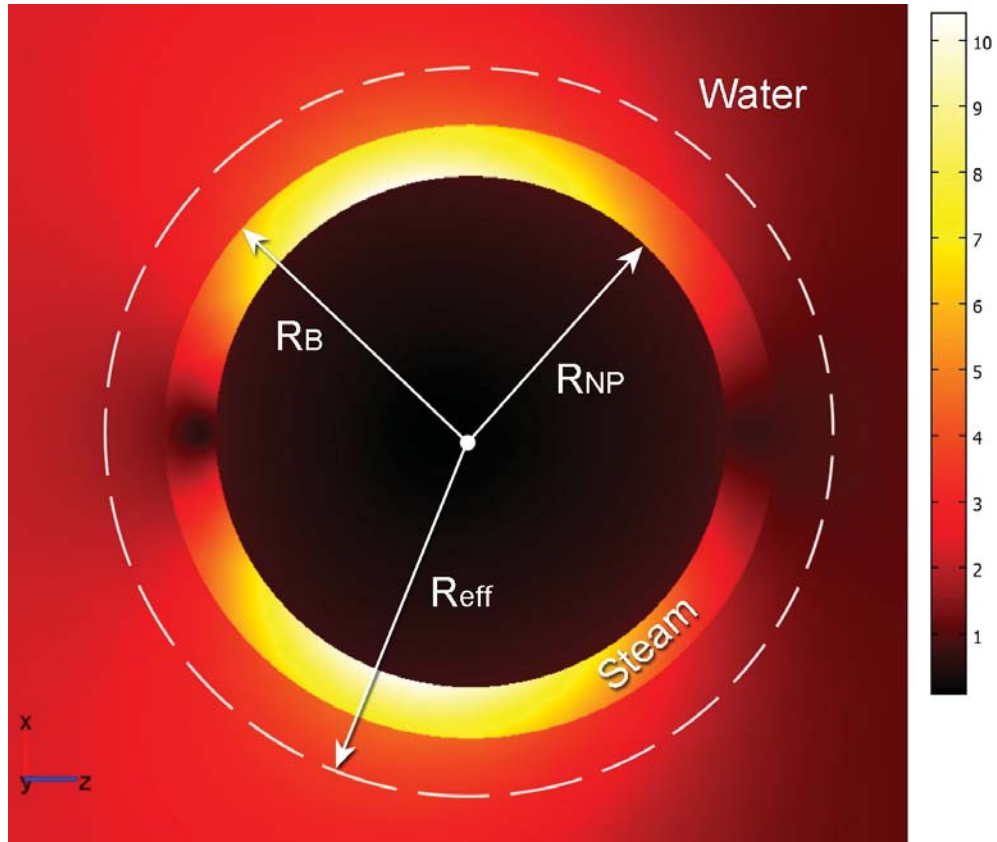


Figure 4.6 : Schematics and simulated scattered electric field intensity ( $|E_{sc}|^2$ ) of a plasmon-heated nanobubble around a gold nanosphere and its ambience. The notations are explained in the main text. The incident field is polarized along x axis and propagates along z axis. The field intensity is for  $R_B=60$  nm and  $R_{NP}=50$  nm.

typical EMM in our model. Different averaging schemes, i. e. the way the averaged permittivity is contributed from different constitutions, are the signatures of different EMMs, while the weights of different constitutions are overwhelmingly just the simple volume fraction of that constitution in various EMM. Quite a few EMMs have already been proposed in literature (See Methods) [225, 226, 227, 228]. To be specific, the EMMs to be discussed are zero screening (ZS), maximum screening (MS), Lorentz-Lorenz/Maxwell-Garnett (LL/MG), Bruggeman, and Lichtenecker. The for-

mer four were discussed in Ref. [225] and the latter in Ref. [226, 227]. Unfortunately, below we will show that none of them deliver satisfactory result, and this is because we used the volume fraction as the weights. Hence, it strongly indicated a poor strategy of weighting in a field-localized scenario. Although there have been various modifications to the conventional EMMs, for instance, by Spanier et al. [229] and by Myroshnychenko et al., [230], and the awareness of the inefficiency of conventional EMM when dealing with intense local field has been brought up (See Fig. 7 in Ref. [230] and the corresponding discussion), an explicit inclusion of the weight of the field in the EMM is still absent to our best knowledge.

To improve the weighting strategy of the water (steam)  $w_w$  ( $w_s$ ), we propose the LFWEMM. In this method,  $w_w$  is proportional not only to the volume filling factor of water, as commonly seen in literature [225], but also to a coefficient representing the exponential decay nature of radial distribution of the local plasmon-induced electric field. For a given  $R_B$ , the actual local field is not spherical symmetric (Fig. 4.6); and the radial distribution is dependent on the bubble radius. For simplicity, we have made two approximations. First, the local field is approximated to be spherically symmetric so that we ignore the angular variation of the field. Second, the radial intensity distribution taken into account in the weighting is approximated to be the one without bubble presented ( $R_B = R_{NP}$ ). Thus, the normalized  $w_w$ , as a function of  $R_B$ , is then described by

$$w_w(R_B) = \frac{\int_{R_B}^{R_{eff}} dr' 4\pi r'^2 e^{-r'/\alpha}}{\int_{R_{NP}}^{R_{eff}} dr' 4\pi r'^2 e^{-r'/\alpha}}, \quad (4.4)$$

where  $\alpha$  is the radial decay length (a parameter to be determined) of the electric field intensity  $|E|^2$ . We then have an equation relating  $R_B$  to the experimentally measured peak shift ratio as (See Methods for detail derivation)

$$\eta \frac{\Delta\lambda_B}{\Delta\lambda_w} = \frac{\int_{R_B}^{R_{eff}} dr' 4\pi r'^2 e^{-r'/\alpha}}{\int_{R_{NP}}^{R_{eff}} dr' 4\pi r'^2 e^{-r'/\alpha}}. \quad (4.5)$$

To justify our claim of bubble formation and our model quality, we take an example by using the experimental data  $\Delta\lambda_B$  and  $\Delta\lambda_w$ , 18 nm and 35 nm respectively, as determined from Fig. 4.5. As a result, Eq. 4.2 yields an effective permittivity of 1.400 within the bubble. Because this number is larger than  $\varepsilon_{air} = 1.00$  but less than  $\varepsilon_w = 1.778$ , the  $R_B$  is expected to be smaller than  $R_{eff}$  and thus both water and steam will be present within  $R_{eff}$  as illustrated in Fig. 4.6. Next,  $R_{eff}$  and  $\alpha$  are calibrated to be 80 nm and 15 nm respectively for gold NS with  $R_{NP}=50$  nm, using the definitions aforementioned. Further, considering the fact that the actual permittivity of steam  $\varepsilon_s$  can be safely set to be 1.00 [231] under our experimental condition (pressure, temperature), we conclude that the difference between  $\varepsilon_s$  and  $\varepsilon_B^{eff}$  reflects a stratified mixture of steam and water in the vicinity of the nanosphere.

By employing the proposed LFWEMM, we can calculate the bubble radius from Eq. 4.5 to be  $R_B=60$  nm. Further confirmed by Mie scattering calculations, this radius corresponds to a  $\Delta\lambda_B/\Delta\lambda_w$  value of 0.40, in good agreement with the experimental value of 0.51.

## Physical origin

Important to know, the physical origin of our weighting function Eq. 4.4 still follows the general concept of effective medium, and our approach is nothing but an analogy to the mean-field based averaging in conventional EMM (See Eq. (2) in Ref. [229]). In conventional EMM, the field is varying slowly so that as a good approximation it can be extracted out of the summation or integral over different constitutions and be normalized out. By contrast, in our LFWEMM, the field is rapidly decaying so that the probability of finding a material with constant field in conventional EMM is naturally in analogous to the probability of finding an infinitesimal volume with constant field in LFWEMM. As a result, the integration for LFWEMM is then taken over infinitesimal volume instead of constitutions (Eq. (2) in Ref. [229]), with the field expression kept in integrand.

### 4.2.3 Benchmark test

The advantage of the proposed LFWEMM is the inclusion of decaying nature of the local field, which other EMMs in literature do not consider. To justify such advantage for bubble characterization purpose, we performed a benchmark test on a gold NS with 50 nm radius, by comparing the result from LFWEMM with those from rigorous Mie calculations, FDTD simulations, and popularly used EMMs in literature [225, 226].

For a given peak shift ratio  $\Delta\lambda_B/\Delta\lambda_w$ , the procedure of solving the radius from different EMM is essentially the same despite different averaging scheme. An example

of solving  $R_B$  using different EMMs for  $\Delta\lambda_B/\Delta\lambda_w=0.51$  is given in Methods, where the averaging strategy for a specific EMM is also presented. The  $R_B$  as a function of the shift ratio was further calculated using the mentioned EMMs as well as our LFWEMM. To obtain a benchmark for comparison, we also performed calculations using Mie and FDTD. The results are presented in Figure 4.7.

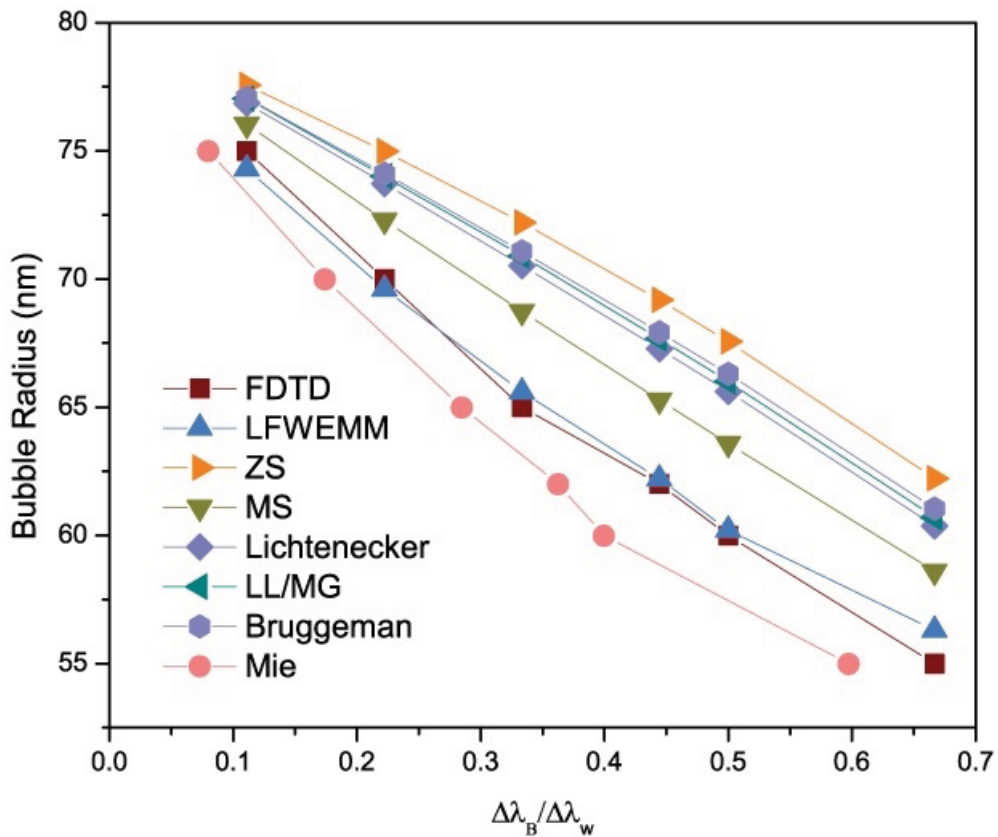


Figure 4.7 : Calculated bubble radius as a function of peak shift ratio. The Mie calculation is accepted to be most accurate; the LFWEMM and FDTD (mesh size=1 nm) have comparable accuracy over a broad range of argument; the LL/MG, Lichtenecker, and Bruggeman lie within two boundaries represented by zero-screening (ZS) and maximum screening (MS).

As we can see in Fig. 4.7, LFWEMM has the best accuracy over other EMMs in

determining  $R_B$ . The results from ZS are overestimated, compared with those from LFWEMM. This is because the ZS only considers the volume fraction of water as the contributing weight to the effective medium, thus requiring that the field strengths inside the two constituent materials be comparable on average. However, this is not true in our investigated model since the local near field outside the gold NS is decaying exponentially. By ignoring the significant field strength difference between the two constituent materials, this model has to exaggerate the  $R_B$  to account for the same contributing weight of steam in LFWEMM. The results from MS are better than ZS but still worse than LFWEMM.

It is commonly accepted that the ZS and MS represent two boundaries of various EMMs. We observed again this behavior in Fig. 4.7 where the curves from LL/MG, Lichtenecker, and Bruggeman all lie within those two from ZS and MS. While volume-fraction weighting is the essence of a traditional EMM, the large error of the resulted bubble layer thickness indicates that using only volume fraction in weights (Eq. (11) in Methods), is insufficient when a highly localized near field pattern is involved. Therefore, a simple and intuitive extension of a traditional EMM should include of the nature of decaying field strength in the weights. As a result, by associating the decaying field pattern to the ZS EMM, the LFWEMM is such a physically-favorable analytical approach that it delivers results much closer to rigorous Mie calculations. As shown in Fig. 4.7, the fact that the LFWEMM curve not lying between ZS and MS also indicates that LFWEMM has broken the boundary of traditional EMMs,

while it still possesses a mathematical conciseness.

#### 4.2.4 Methods

##### Mie and FDTD calculations

All Mie and FDTD calculations were carried out under plane wave excitation and the used dielectric function of gold was by Johnson and Christy [141]. For Mie, it is accepted to be the most accurate method for a spherical object and the details can be found in Ref. [74, 75]; the maximal orbital momentum  $l=20$  was used. For FDTD, we used a mesh size of 1 nm where the results were confirmed to have been converged.

##### Application of a typical EMM in bubble radius calculation

In a typical effective medium method, the overall permittivity of the water-steam mixture is determined by

$$\varepsilon^{eff} = w_s \varepsilon_s + w_w \varepsilon_{w-hot}, \quad (4.6)$$

where  $\varepsilon_{w-hot}$  is the permittivity of surrounding hot water within  $R_{eff}$  at assumed temperature of 373K, and  $w_s$  and  $w_w$  are weights of the steam and water respectively, which should satisfy

$$w_s + w_w = 1. \quad (4.7)$$

Plugging Eq. 4.7 into Eq. 4.6 yields  $\varepsilon^{eff} - \varepsilon_{air} = (1 - w_w) \varepsilon_s - \varepsilon_{air} + w_w \varepsilon_{w-hot}$ , and by using  $\varepsilon_s = \varepsilon_{air} = 1$  we have

$$\frac{\varepsilon^{eff} - 1}{\varepsilon_{w-hot} - 1} = w_w. \quad (4.8)$$

By comparing Eq. 4.8 to Eq. 4.2 and noting  $\varepsilon_{air} = 1$ , we obtain

$$\eta \frac{\Delta\lambda_B}{\Delta\lambda_w} = w_w, \quad (4.9)$$

where  $\eta \equiv (\varepsilon_w - 1)/(\varepsilon_{w-hot} - 1)$  is the correction coefficient for water temperature difference and is calculated as 1.05, since  $\varepsilon_{w-hot} = n_{w-hot}^2 = 1.740$  ( $n_{w-hot} = 1.319$ ) and  $\varepsilon_w = 1.778$  [231]. To insert into our model an EMM with a same averaging scheme (described by Eq. 4.6) but different weighting function, i. e.  $w_w$ , we just replace the right hand side of Equation 4.9 with specific weighting function of water of that EMM. For an EMM with a different averaging scheme from Eq. 4.6, see the examples below.

### Bubble radius from different traditional EMMs

The solving process for different traditional EMMs is essentially the same: calculate the effective permittivity from Eq. 4.2 first; then solve the bubble radius from permittivity-averaging equation when using a volume fraction for the water weight. Let us use  $\Delta\lambda_B/\Delta\lambda_w=0.51$  for example. The effective permittivity in ZS method is described by Eq. 4.6 with a weight of water

$$w_w(R_B) = \frac{R_{eff}^3 - R_B^3}{R_{eff}^3 - R_{NP}^3}. \quad (4.10)$$



This ZS method, simply yields  $R_B=68$  nm. For the MS method, we have

$$\frac{1}{\varepsilon^{eff}} = \frac{w_s}{\varepsilon_s} + \frac{w_w}{\varepsilon_{w-hot}}, \quad (4.11)$$

with also the weighting function as Eq. 4.10. Following similar derivation from Eq. 4.6 to 4.8, we obtained

$$\frac{1/\varepsilon^{eff} - 1}{1/\varepsilon_{w-hot} - 1} = w_w. \quad (4.12)$$

To replace the  $\varepsilon^{eff}$  by an experimentally observable quantity  $\Delta\lambda_B/\Delta\lambda_w$ , we combine Eq. 4.12 and 4.2 and have

$$\frac{\eta\varepsilon_{w-hot}}{\varepsilon_w - 1 + (\Delta\lambda_B/\Delta\lambda_w)^{-1}} = w_w. \quad (4.13)$$

Further combination of Eq. 4.13 and 4.10 gives  $R_B=63$  nm. Lichtenecker equation [226, 227] yields (remembering  $\varepsilon_s=1$ )

$$\frac{\log\varepsilon^{eff}}{\log\varepsilon_{w-hot}} = w_w, \quad (4.14)$$

which together with Eq. 4.2, 4.10 gives an  $R_B=65$  nm.

In our investigated model as illustrated in Fig. 4.6, if we consider the steam as the hosting dielectric, the Lorentz-Lorenz (LL) method is equivalent with Maxwell-Garnett (MG) method [225], i. e.

$$\frac{\varepsilon^{eff} - 1}{\varepsilon^{eff} + 2} = w_s \frac{\varepsilon_s - 1}{\varepsilon_s + 2} + w_w \frac{\varepsilon_{w-hot} - 1}{\varepsilon_{w-hot} + 2}, \quad (4.15)$$

because  $\varepsilon_s=1$ . Following a similar calculation, Eq. 4.15 and 4.10 yield an  $R_B =66$  nm. Bruggeman method is given by (Ref. [225])

$$0 = w_s \frac{\varepsilon_s - \varepsilon^{eff}}{\varepsilon_s + 2\varepsilon^{eff}} + w_w \frac{\varepsilon_{w-hot} - \varepsilon^{eff}}{\varepsilon_{w-hot} + 2\varepsilon^{eff}}. \quad (4.16)$$

Having known that  $\varepsilon^{eff}=1.40$ , we solved  $w_w=0.58$  from Eq. (17). Plugging  $w_w=0.58$  into Eq. 4.10 also yields  $R_B=66$  nm.

### 4.3 Determination of bubble pressure and temperature

For calculating the temperature inside the nanobubble, the steam generated inside the bubble is assumed saturated. Hence the pressure of the saturated steam is actually the vapor pressure of water as a function of temperature. In addition, once formed, the nanobubble is assumed in steady-state and the system in thermal equilibrium such that the steam pressure is equal to the Laplace pressure due to surface tension at the water-steam interface. We then use the Clausius-Clapeyron Relation (CCR), Eq. 4.3, to represent the relation between the vapor pressure of water and the temperature. In Equation 4.3, the left hand side is the CCR and the right hand side is the Laplace pressure. The surface tension coefficient is a function of temperature:  $\gamma(T) = -0.2222T + 142.2$  mN/m [232]. The parameters in the CCR for water are  $C = 95$  GPa and  $h = 7082 \times 10^{-20}$  J. By plugging in  $R_B=60$  nm, we solved Ts from Eq. 4.3 to be 462 K which corresponds to a steam pressure 1.42 MPa. It is worth to reemphasize that at such pressure and temperature, the refractive index of steam is determined to be  $n=1.002$  at a source wavelength of 532 nm, according to Eq. A1 in Ref. [231] as well as the reference therein. It is important to mention that this value of  $n$  is self-consistent with our previous assumption in which the refractive index of steam is 1, a crucial value in the analysis of the steam shell thickness.

#### 4.4 Analysis of nanosphere surface temperature

The energy-conservation must be obeyed in any energy exchange process. In our case, when the system spatially within  $R_{eff}$  is steady, the absorbed power must be totally dissipated and we assume 100% transfer rate into Joule heat. Fouriers law for heat transfer at the Gold-steam interface is expressed as

$$P_{abs} = G_{g,s}S_{NP}(T_{NP} - T_s), \quad (4.17)$$

where  $P_{abs}$  is the power absorbed by the Au NP,  $G_{g,s}$  is the effective interfacial thermal boundary conductance,  $S_{NP} \equiv 4\pi R_{NP}^2$  is the surface area of the nanoparticle, and  $T_{NP}$  is the NP surface temperature. Similarly, at the steam-water interface, we have

$$P_{abs} = G_{s,w}S_B(T_s - T_w), \quad (4.18)$$

where  $G_{s,w}$  is the effective thermal boundary conductance at the steam-water interface,  $S_B \equiv 4\pi R_B^2$  is the outer surface area of the nanobubble, and  $T_w$  is the temperature of the surrounding hot water within  $R_{eff}$ , assumed to be the water boiling point 373 K. The power by the Gold NS is determined as  $P_{abs} = \sigma P_{inc}/A$ , where  $\sigma$  is the effective absorption cross section of the Gold NS after nanobubble formation,  $P_{inc}$  is the incident power of the laser, and  $A \equiv \pi D^2/4$  is the laser spot area with a diameter  $D = 1 \mu\text{m}$ . We obtain  $P_{abs} = 0.59 \text{ mW}$  for a single Gold NP with 100 nm diameter, given that  $P'_{inc} = 24 \text{ mW}$  (a 25mW input power multiplied by 96% transmission of the glass cover slide), and  $\sigma = 0.0192 \mu \text{ m}^2$  as calculated by Mie method.

By inserting  $P_{abs} = 0.59$  mW,  $R_B = 60$  nm,  $T_s = 462$  K,  $T_w = 373$  K into Eq. 4.18, we have  $G_{s,w} = 146$  MW/(m<sup>2</sup>K). This value is comparable to the nanoscale gold-water (105 MW/(m<sup>2</sup>K)) [30] and platinum-water (130 MW/(m<sup>2</sup>K)) [233] values. Noting that the effective steam-water interfacial thermal conductance (ITC) is within the same order as the metal-water ITCs, we argue that such a high thermal conductance may be a result of *condensation-evaporation* balance at steam-water interface where saturated steam meet the water. Unlike an unsaturated steam layer that is a thermal insulator, the saturated steam layer is surprised to behave like an excellent thermal conductor. For explanation of the large  $G_{s,w}$ , while it seems beyond the limit of traditional description of ITC employing acoustic mismatch and phonon scattering, we believe that it is essential for a successful heat transfer theory to include the interfacial phase-transition dynamics at nanoscale.

We propose two different methods to estimate the effective gold-steam ITC. On one hand, first, we can assume a stronger phonon coupling at the Gold-steam interface than at steam-water interface, by knowing that solids usually have well-defined densities of states of phonons compared with liquids; next, we can assign a moderate enhancement  $G_{g,s} = 2G_{s,w} = 292$  MW/(m<sup>2</sup>K). On the other hand, the second method features a common hypothesis that the interfacial heat transfer is in analogous to serial resistances in an electrical circuit. We can write  $1/G_{x,y} = 1/G_x + 1/G_y$ , where the  $x$ ,  $y$  can be any combination of s, w, and g, simply denoting the bulk (at nanoscale) contributions to the ITC from steam, water and gold. The saturated

steam is further assumed to possess ideal thermal conducting and interfacial coupling properties, leading to an infinite  $G_s$ . Then  $G_w = G_{s,w} = 146 \text{ MW}/(\text{m}^2\text{K})$  results, leading to  $G_{g,s} = G_g = (1/G_{g,w} - 1/G_w)^{-1} = 373 \text{ MW}/(\text{m}^2\text{K})$ . Both estimated value of  $G_{g,s}$  are close to each other, and the lesser value  $G_{g,s} = 292 \text{ MW}/(\text{m}^2\text{K})$  is chosen to reflect an imperfect interface. Finally, from Eq. 4.17,  $T_{NP} = 526 \text{ K}$  is calculated given  $R_{NP} = 50 \text{ nm}$ ,  $P_{abs} = 0.59 \text{ mW}$ , and  $T_s = 462 \text{ K}$ .

## 4.5 Conclusion

The studies we report here of plasmon-induced heating and steam generation nucleated by individual nanoparticles are among the first direct measurements that allow specific tests of theoretical modeling of thermal dissipation at the nanoscale. Our approaches for characterizing bubble formation at both the nanoscale and the macroscale may pave the way for the use of this type of localized remote heating in applications such as catalysis and other chemical or material processing, and biomedical applications that may include remote, intracellular diagnostic, delivery or therapy systems [206, 216, 126].

A novel effective medium method (EMM) for describing the near-field interaction between localized surface plasmon resonance and ambient dielectric material has been proposed. It has been applied in characterizing the plasmon-heated nanobubble around a gold nanosphere under CW excitation. Generally, the formation of nanobubble around a metal nanosphere decreases the average permittivity in local

dielectric and thus blueshifts the dipolar resonance, with respect to the pure water ambience. The bubble size is thus characterized by using an effective medium method to relate the peak shift to the existence of the bubble. To justify this approach, we plugged in observable shift and the bubble radius as a function of the shift ratio resulted from various EMM agrees qualitatively well with that from Mie calculations. In comparison with other conventional EMMs where the weighting function is only the volume fraction, our LFWEMM yields better results by benchmark testing with Mie calculations and exceeds the existing limit dictated by maximum screening EMM. It indicates that the inclusion of exponentially decaying nature of the local field in the weighting function is essential for describing the near-field interaction between surface plasmon, the origin of drastically changing field near the metal surface, and environmental dielectrics. Overall, our LFWEMM is shown to exceed the limits of conventional EMMs and may inspire further work of incorporating near field pattern into an EMM.

The pressure and temperature of the nanobubble were also determined by employing Clausius-Clapeyron Relation and surface-tension induced Laplace pressure. The surface temperature of the nanosphere was also analyzed. The hypothetically calculated result indicates that the saturated steam serves as an ideal thermal conductor at nanoscale.

## Chapter 5

### Four-wave mixing in nanocluster

#### 5.1 Introduction

Plasmonic nanoclusters, an ordered assembly of coupled metallic nanoparticles, support unique spectral features known as Fano resonances (FR) [234, 91, 235, 236] due to the coupling between their subradiant and superradiant plasmon modes. Within the Fano resonance, absorption is significantly enhanced, giving rise to highly localized, intense near fields with the potential to enhance nonlinear optical processes [237, 238]. Here we report a structure supporting the coherent oscillation of two distinct FRs within an individual plasmonic nanocluster. We show how this coherence enhances the optical Four-Wave Mixing (FWM) process, in comparison to other double-resonant plasmonic clusters that lack this specific property. A model that explains the observed FWM features is proposed, based on the intense local fields at the nanocluster surfaces, which is generally applicable to any third-order processes in plasmonic nanostructures. With a larger effective susceptibility  $\chi^{(3)}$  relative to existing nonlinear optical materials, this coherent double-resonant nanocluster offers a new strategy for designing high-performance third-order nonlinear optical media.

Traditionally, nonlinear optical phenomena have relied on crystalline media that

combine material susceptibilities and phase matching to optimize the nonlinear optical process. It has recently been shown that certain plasmonic nanostructures can produce an enhanced nonlinear response when excited at their resonant frequency [239, 120]. Phase-matching requirements [240, 241, 242] for nonlinear optics in macroscopic media are usually optimally fulfilled at nanoscale dimensions ( $\text{sinc}^2(\Delta kz/2) \sim 1$  for small  $z$ , where  $z$  is the propagation distance through the medium). For plasmonic nanostructures, the most important property for the enhancement of nonlinear properties is their increased local fields at their resonances, which can provide larger *effective* susceptibilities than their intrinsic material susceptibility.

In the third-order nonlinear process of four-wave mixing (FWM), two external fields  $E_0(\omega_1)$  and  $E_0(\omega_2)$  are simultaneously incident on the nanostructure, inducing local fields  $E(\omega_1)$  and  $E(\omega_2)$ ; absorbing two  $\omega_2$  and one  $\omega_1$  photons and emitting a photon at  $\omega_{FWM} = 2\omega_2 - \omega_1$  (Fig. 5.1a). The electromagnetic FWM enhancement  $G_{FWM} = |E(\omega_2)/E_0(\omega_2)|^4 \cdot |E(\omega_1)/E_0(\omega_1)|^2$  thus depends on the field enhancements at the input frequencies. Fano-resonant structures can exhibit very large local field enhancements<sup>1,5</sup>, making these structures prime candidates for nonlinear frequency generation through this third-order process. While previous studies of nonlinear plasmonics employed nanostructures with a single dipolar resonance [243, 244], in a multi-input process such as FWM, the conversion efficiency is expected to be further enhanced if the plasmon modes of the nanostructure are resonant with both



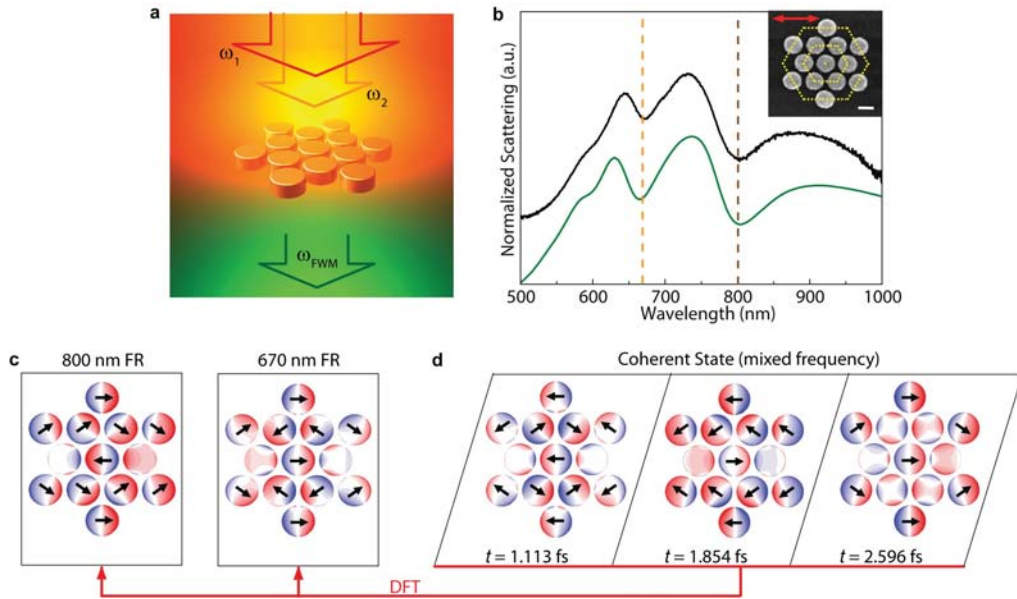


Figure 5.1 : FWM configuration and characterization of the double Fano resonant plasmonic nanocluster. (a) FWM configuration in a single nanocluster, where two coherent inputs at frequencies  $\omega_1$  and  $\omega_2$  generate a plasmon-enhanced FWM signal  $\omega_{FWM} = 2\omega_2 - \omega_1$ . (b) Experimental (black) and calculated (green) dark-field scattering spectra of the nanocluster obtained with horizontal (x-) polarization. Two prominent minima at 800 and 670 nm are labeled by brown and orange dashed lines. The inset shows an SEM image of the nanocluster. Scale bar, 100 nm. All disk diameters are 120 nm with 50 nm heights and  $\sim 18$  nm gaps. Superimposed yellow dashed lines denote the central disk, inner and outer disk rings of the nanocluster. Red arrow indicates the incident polarization. (c,d) Snapshots of simulated charge densities  $\rho(\mathbf{r}, t)$  on the top surface of the nanocluster for the 800 and 670 nm FRs at  $t = 0$  (c), and for the coherent state at 3 different times (d). Black arrows correspond to local E-field directions.

input frequencies [245].

In this study, we demonstrate highly efficient FWM from a plasmonic nanocluster that supports two distinct FRs. When excited by a coherent source, the FRs oscillate collectively, in a mixed frequency analog to a two-state quantum system, where the electric fields from the two modes add coherently, resulting in strong field enhance-

ments. In comparison, plasmonic nanostructures with resonances at the same two frequencies that lack coherence are found to give rise to significantly lower FWM efficiencies, although providing similar linear optical properties.

## 5.2 Double Fano-resonance structure

The geometry of the nanocluster was designed such that its FRs were tuned to the two excitation frequencies needed for FWM. The nanocluster, composed of a central disk, an inner ring of disks and a degenerate outer ring of disks (Fig. 5.1b, inset), belongs to the  $D_{6h}$  symmetry group<sup>3</sup>. Measured and calculated linear scattering spectra (Fig. 5.1b) reveal two prominent scattering minima. The origin of these spectral dips can be understood by examining the charge densities ( $r, t$ ) at the spectral minima (Fig. 5.1c), where the structure supports oscillations of the central disk and the inner and outer rings of disks. At the 800 nm minimum, the center particle dipole oscillates out-of-phase with both the inner and outer collective ring oscillations. However, at the 670 nm minimum, the center particle dipole oscillates out-of-phase with the inner ring but in-phase with the outer ring.

When both FRs of the nanocluster are excited simultaneously (by two coherent beams), the plasmons oscillate in a mixed frequency coherent state. In this mode, the charge oscillation of the central disk switches rapidly between an in-phase and out-of-phase motion with respect to the outer ring, in each case corresponding to the oscillatory behavior of one of the FRs (Fig. 5.1d ). By performing a discrete

Fourier transform [246] on the time series of charge densities  $\rho(\mathbf{r}, t)$  at each position  $\mathbf{r}$ , this coherent state, with a period  $T_{coherent} \sim 13.35$  fs, can be decomposed into two discrete FR eigenmodes with  $\rho(\mathbf{r}, t)$  at 800 ( $T_1 \sim 2.67$  fs) and 670 nm ( $T_2 \sim 2.23$  fs). The coherent mode has a period equal to the time when the two discrete FRs have the same phase ( $T_{coherent} \simeq 5T_1 \simeq 6T_2$ ), undergoing  $\sim 15$  periods during the pulse duration used in the experiment ( $\sim 200$  fs). For the coherent state, enhanced local fields at multiple resonant frequencies overlap not only in time but also in space, contributing to the nonlinear optical wave-mixing.

### 5.3 FWM measurements

FWM measurements on individual nanoclusters were performed using a specially designed optical microscope with a high-precision positioning stage that facilitates focusing. Two linearly (x-) polarized, collinear and coherent pulse trains (along the  $z$  direction) at  $\lambda_1=800$  nm and  $\lambda_2=670$  nm, resonant with both FRs were focused onto an individual nanocluster (in the x-y plane), resulting in a spot size of  $\sim 1$   $\mu\text{m}$ . The scattered radiation was collected by another focusing objective in transmission and analyzed with a CCD-coupled spectrometer. Only the case where both lasers were x-polarized was investigated, since this configuration generated the strongest FWM signal. The total average applied power ranged from  $1\sim 3$   $\mu\text{W}$  (peak intensities of  $0.13\text{--}0.4$   $\text{GW cm}^{-2}$ ), and measurements were performed on 6 different nanoclusters to ensure statistical validity. All nanoclusters underwent a pulsed laser annealing

procedure using  $3.8 \mu\text{W}$  total power for 4 minutes to stabilize the nanostructure prior to data collection.

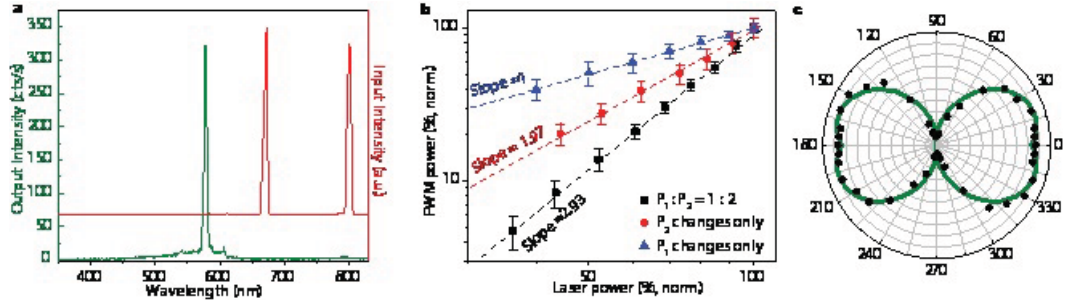


Figure 5.2 : FWM Experiments by individual nanoclusters. (a) Spectra of the two input laser beams (red), and a FWM output signal generated by  $P_1 = 1 \mu\text{W}$  and  $P_2 = 1.9 \mu\text{W}$  (green). The small spectral feature at  $\sim 615 \text{ nm}$  is the edge of the short pass filter used to block the excitation beams. (b) Normalized FWM power versus normalized total input power  $P_{\text{tot}}$  (black squares),  $P_2$  only (red circles) and  $P_1$  only (blue triangles) on a log-log scale. Dashed lines are linear fits of the experimental data. Error bars represent the standard deviations of signals from six individual nanoclusters, arising mainly from fabrication irregularities. (c) Polar plots show the measured (black circles) and calculated (green curve) FWM polarization by two x-polarized lasers. The latter is calculated based on Fig. 5.3c.

A characteristic output spectrum consists of a sharply peaked FWM signal centered at  $\lambda_{FWM} = 576 \text{ nm}$  with  $\Delta\lambda_{FWM} = 5.3 \text{ nm}$ , on top of a significantly weaker, broadband multiphoton luminescence (MPL) signal [247] (Fig. 5.2a, green). The Gaussian line shape FWHM of the incident beams was measured to be  $\Delta\lambda_1 = 5.3 \text{ nm}$  and  $\Delta\lambda_2 = 5.5 \text{ nm}$  (Fig. 5.2a, red). Additionally, we observed another FWM signal centered at  $\lambda_{FWM2} = 993 \text{ nm}$ , due to the complementary  $\omega_{FWM2} = 2\omega_1 - \omega_2$  process. Since this signal lies at the limit of our CCD detection range, we focused on the 576 nm FWM signal only.

The FWM power was observed to follow a cubic power law behavior as a function

of total input power ( $P_{tot} = 1.05\text{--}2.9\ \mu\text{W}$ , using  $P_1 : P_2 = 1:2$ ) (Fig. 5.2b). This response scales quadratically with the  $P_2$  input power ( $0.84\text{--}1.9\ \mu\text{W}$ , with  $P_1$  fixed at  $1.1\ \mu\text{W}$ ), and linearly with  $P_1$  ( $0.4\text{--}1\ \mu\text{W}$ , with  $P_2$  fixed at  $1.9\ \mu\text{W}$ ). All data points in this regime follow a simple power law behavior, indicating that we are NOT in a regime of plasmon saturation [248]. Increasing the input power further causes optical damage: when this occurs, the FWM signal gradually and irreversibly decreases. We calculated the nonlinear cross section for the nanocluster to be  $\sigma^{(3)} = 1.41 \times 10^{-12}\ \text{cm}^2$ , and its effective susceptibility  $\chi^{(3)}$  is  $4.65 \times 10^{-15}\ \text{m}^2\ \text{V}^{-2}$  ( $3.35\ \text{times}\ 10^{-7}\ \text{esu}$ ), taking into account the instrument efficiency<sup>9</sup>. This value is much larger than that of nonresonant dielectrics [240] ( $10^{-22} \sim 10^{-18}\ \text{m}^2\ \text{V}^{-2}$ ), semiconductors [249] ( $\sim 10^{-12}\ \text{esu}$ ) or nonlinear crystals [250] ( $10^{-14} \sim 10^{-13}\ \text{esu}$ ), and among the highest reported for metallic nanoparticles [251, 252, 253, 254] ( $10^{-12} \sim 10^{-7}\ \text{esu}$ ), which we attribute to the enhancement provided by the coherently coupled FRs in the nanostructure. The polarization dependence of the FWM signal has an unusual butterfly-like profile, with its maximum intensities near  $20^\circ$  and  $160^\circ$  (Fig. 5.2c, black circles). The FWM light has a nonzero y-component, despite the fact that both pump lasers are purely x-polarized. These results are distinct from previous studies [244, 255] where the FWM was linearly polarized for either parallel or oblique incidence.

## 5.4 FDTD-assisted modelling

We have developed a simple model to explain the origin and characteristics of FWM on a plasmonic nanocluster. In degenerate FWM, the two local fields  $\tilde{E}(\mathbf{r}, \omega_1, t)$  and  $\tilde{E}(\mathbf{r}, \omega_2, t)$  induce a nonlinear polarization

$$\mathbf{P}^{(3)}(\mathbf{r}, \omega_{FWM}) = \varepsilon_0 \overline{\chi^{(3)}}(-\omega_{FWM}; \omega_2, \omega_2, \omega_1) : \mathbf{E}(\mathbf{r}, \omega_2) \mathbf{E}(\mathbf{r}, \omega_2) \mathbf{E}^*(\mathbf{r}, \omega_1), \quad (5.1)$$

where  $\tilde{\mathbf{E}}(\mathbf{r}, \omega, t) = \mathbf{E}(\mathbf{r}, \omega) e^{-i\omega t}$  is the harmonic oscillating instant field with amplitude  $\mathbf{E}(\mathbf{r}, \omega)$ ; the susceptibility tensor  $\overline{\chi^{(3)}}$  accounts for the intrinsic third-order nonlinear response of the material(s), and in turn gives rise to a FWM field  $\mathbf{E}(\mathbf{r}, \omega_{FWM}) = \mathbf{P}^{(3)}(\mathbf{r}, \omega_{FWM}) / \varepsilon_0 n^2(\omega_{FWM})$  radiating at  $\omega_{FWM} = 2\omega_2 - \omega_1$ . When both incident frequencies are at FRs, enhanced local fields spatially overlap (with same  $\mathbf{r}$ ) at the nanocluster gap regions (Fig. 5.3a). These intense fields give rise to a large effective  $\overline{\chi^{(3)}}$  [243, 248]. At optical frequencies, plasmon-enhanced local fields are confined within a thin layer on each metal-dielectric surface, in the direction of the surface normal [120] with a dominant surface nonlinearity [256, 257], thus equation 5.1 can be transformed into the surface coordinate system where only the normal component is considered:

$$E_{s,n}(\omega_{FWM}) = \chi_{s,nnnn}^3 E_{s,n}^2(\omega_2) E_{s,n}(\omega_1) / n^2(\omega_{FWM}), \quad (5.2)$$

where  $\chi_{s,nnnn}^3$  is assumed to be a constant over the metal surfaces for simplicity.

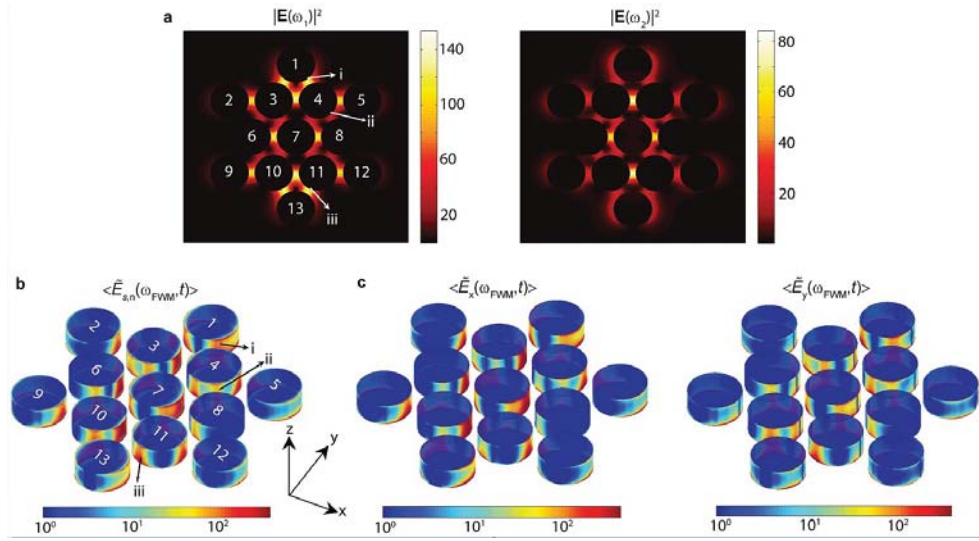


Figure 5.3 : FDTD calculated near-field maps of the nanocluster. (a) The field enhancement intensity ( $E^2$ ) evaluated at mid-height of the nanocluster at  $\lambda_1 = 800$  nm (left) and  $\lambda_2 = 670$  nm (right). (b) Time-averaged FWM fields generated on the Au nanocluster surfaces. The color scales assume unity incident fields and  $\chi_s^{(3)}/n^2$ . Most prominent hotspots reside on disk sides. Top and bottom disk surfaces exhibit minimal field enhancements. In (a) and (b), the overlaid disk indices are guides to the eye; i, ii and iii points to three hotspots. (c) Time-averaged x- (left) and y- (right) components of the FWM fields on the nanocluster surfaces.

Because the generated FWM field oscillates rapidly with time, the measured signal is the time-averaged intensity  $I(\omega_{FWM}) \propto E^2(\omega_{FWM})$ . A generalized formula is obtained for FWM fields enhanced by plasmonic nanostructures (Fig. 5.3b):

$$\begin{aligned}
 \langle \hat{E}_{s,n}(\omega_{FWM}, t) \rangle &= \left[ \frac{1}{T} \int_0^T E_{s,n}^2(\omega_{FWM}) \cos^2(\omega_{FWM}t) dt \right]^{1/2} \\
 &= \frac{\sqrt{2}}{2n^2(\omega_{FWM})} \chi_{s,nnnn}^3 E_{s,n}^2(\omega_2) E_{s,n}(\omega_1). \quad (5.3)
 \end{aligned}$$

Polarization of each FWM photon is perpendicular to the Au side walls (in the x-y plane), providing that the photon polarization is the same as its local fields. The FWM field map can be decomposed into x- and y- components (Fig. 5.3c), and then

the far field FWM polarization is obtained by integrating over the Au surfaces,

$$I_{FWM}(\theta) \propto \int [ \langle \hat{E}_x(\omega_{FWM}, t) \rangle |\cos\theta| + \langle \hat{E}_y(\omega_{FWM}, t) \rangle |\sin\theta| ]^2 ds \quad (5.4)$$

where  $\theta$  is the angle between the output polarizer and the  $x$ -axis. The calculated FWM polarization polar plot (Fig. 5.2c, green curve) has a small  $y$ -component at  $\theta = 90^\circ$  and a big  $x$ -component that is slightly reduced at  $\theta = 0^\circ$ . The degree of polarization,  $P_d = |I_x - I_y| / (I_x + I_y) = 0.64$ , is consistent with experimental results. Such unusual polarization behavior is because some FWM hotspot polarization are not parallel to either the  $x$ - or  $y$ -axis (e.g. i, ii and iii in Fig. 5.3b) and therefore contribute partially to each of the orthogonal components of the emitted light.

## 5.5 Control experiments

To further investigate the advantages of coherent FRs on the enhancement of optical FWM, two nanocluster controls with double-resonance feature were designed. (1) one with two coherent bright modes, where charges oscillate in dipole-dipole (antibonding) and dipole-quadrupole modes (Fig. 5.4a,c), and (2) one with incoherent (spatially decoupled) oscillations of a subradiant heptamer dark mode and a dipole bright mode supported by the corner disks (Fig. 5.4b,d). The plasmon resonant features were designed to correspond to the two FWM input frequencies. All structures are designed with the same volume of Au. The gap sizes [243, 245, 258] were also made identical in all three cases, except for the  $\sim 80$  nm decoupling spacing in case 2 (Fig. 5.4a and 5.4b, insets). Fig. 5.4e shows the time-averaged FWM fields. By integrating the



square modulus of the FWM field over the disk surfaces shown in Fig. 5.3b or 5.4e, relative FWM cross sections ( $\propto$  conversion efficiencies) can be calculated for these 3 structures, which agree well with the measured FWM intensities by  $P_1 = 1 \mu\text{W}$  and  $P_2 = 1.9 \mu\text{W}$  (Fig. 5.4f). The structure supporting two coherent FRs provides the highest FWM enhancement among these three types of double-resonant structures, due to the reduced light scattering and intense local fields of the coherently coupled (spatially overlapping) FRs. Control (2), where the two resonances are spatially decoupled, has the lowest FWM enhancement.

## 5.6 Conclusion

In conclusion, we have demonstrated for the first time a plasmonic nanocluster supports two FRs in a coherent state, a temporal evolution of two excited subradiant states in interference. Time-resolved field investigations reveal the ultrafast dynamics of this coherent state, suggesting that dynamical studies may lead to a greater understanding of coherence in plasmonic nanocomplexes. We have also shown that this nanostructure provides an outstanding resonant enhancement of optical four-wave mixing, providing significantly greater enhancement of this process than similarly sized nanoclusters with double resonances of different types. The extremely large effective  $\chi^{(3)}$  for this nanocluster strongly suggests its use in high-performance synthetic nonlinear optical materials, which would provide new strategies for optical information processing, sensors and detectors, and new types of optoelectronic devices.

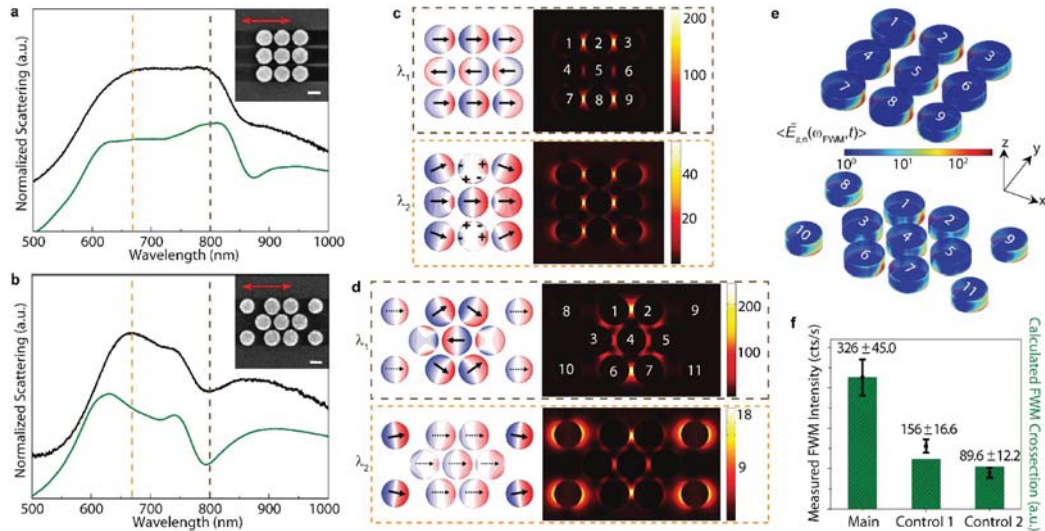


Figure 5.4 : FWM control experiments. (a,b) Experimental (black) and calculated (green) dark-field scattering spectra of two nanoclusters for control experiments, obtained with horizontal (x-) polarization. Both structures have double resonances, indicated by the brown (800 nm) and orange (670 nm) dashed lines. Insets are SEM images of these nanoclusters. Scale bars, 100 nm. Red arrows indicate the incident polarization. In a, all disk diameters are 144 nm with  $\sim 18$  nm gaps. In (b), the nanocluster is formed by a heptamer surrounded by four corner disks. Heptamer disks are 135 nm in diameters with  $\sim 18$  nm gap; corner disks are 124 nm with  $\sim 80$  nm spacing from heptamer disks along x direction. (c,d) Simulated charge distributions (left) and field enhancement intensities  $E^2$  (right) for two control cases at  $\lambda_1 = 800$  nm (brown dashed box) and  $\lambda_2 = 670$  nm (orange dashed box). Black arrows indicate local E-field directions. e, Time-averaged FWM fields on nanocluster surfaces. The color scales assume unity incident fields and  $\chi_s^{(3)}/n^2$ . In c, d and e, the overlaid disk indexes are guides to the eye. f, Measured FWM intensities (error bars) and calculated FWM crosssection (green bars) for all 3 structures.

## Chapter 6

### Conclusions

Several studies on the plasmonic properties and the relevant promising applications of various types of metallic nano-structures in one, two, or three dimensions have been presented. For 1D nanostructure, a near unity absorber operating at visible regime is realized on a hetero-layered nanofilm-based sandwich structure perforated by a periodic array of holes. The coupling mechanism from free space photon to SPP are studied. A theoretical perturbation approach is applied to explain the experimentally observed absorption peak splitting which is dependent on the hole size. Qualitative agreement is achieved between experiment and theory.

For 2D nanowires, a type of nanobelt having rectangular cross section and nanoscale width and height has recently been synthesized. The gold nanobelt, under epi-bright white-light illumination, exhibits a LSPR in the visible regime. The resonant wavelength redshifts with increasing aspect ratio approximately linearly. This dependence of LSPR on the aspect ratio is confirmed in FDTD simulations in excellent agreement, indicating a strong tunability of the LSPR by a 2D nanostructures which is a natural candidate for transporting energy and signal. The mode confinement and propagation is further investigated for the gold nanobelts. A cross-over of the propagating intensities of the  $m=0$  and  $m=1$  modes has been predicted in simulations and observed

in experiment. A Figure-of-Merit (FOM), which favors long propagation and strong confinement, is calculated to be around 1300 for the  $m=1$  mode propagating on a gold nanobelt with  $125 \times 40 \text{ nm}^2$  dimensions. To the author's best knowledge, this FOM has exceeded the performance of peer nanowire candidates with sub-wavelength form-factor that operate in visible or near infrared regime. This strong confinement while preserving the long propagation feature will benefit the future research, such as interaction between quantum emitter and nanobelt, localized energy transportation, etc.

In 3D nanostructures, electrons are further confined thus enabling another type of application: localized heat generator. The plasmon-heating-enabled nanobubble generation from an individual gold nanosphere has been investigated. When illuminated by a laser, a gold nanosphere is heated significantly by plasmon-induced electron-electron scattering, serving as a local heat source. The liquid surrounding the nanosphere is then heated up. At sufficient incident power that exceeds the threshold the heating power is so high that the surrounding water fails to conduct the heat outwards in time. The only consequence is that the surrounding liquid experiences an explosive phase transition and form a vapor bubble where the internal vapor pressure must be balanced out by the pressure outside the bubble, in addition to the surface-tension induced pressure, in a steady-state. Nanobubble generation by gold nanosphere embedded in water under laser illumination is evidenced by significant shift observed in optical spectra which can not be explained without bubble gener-

ated. Mie calculations are performed to search the bubble size that best matches the measured relative shift. A bubble layer thickness of 6.5 nm is resulted. On the other hand, effective medium methods (EMMs) are also employed for solving the bubble radius directly by using the measure shift as an input. A novel local field weighted effective medium method (LFWEMM) is proposed to include the exponentially decaying nature of the near field distribution. It is found that this LFWEMM outperforms other existing conventional EMMs by using Mie calculations as benchmark. The advantage of the LFWEMM over other EMMs indicates a new strategy of including the local field contribution into the weights of components in an EMM, so as to account for the effect of highly localized near field. After the bubble size is determined, under classical thermal equilibrium assumption, Clausius-Clapeyron Relation and surface tension at water-vapor interface are equalized to determine the vapor temperature and pressure. The further derived temperature of gold nanosphere surface agrees well with that from Raman spectroscopy. The evolution from nanobubble to microbubble is also investigated. An approximate linear dependence of the formed-bubble radius and the incident power is observed and explained. Our study has enriched the understanding of the nanoscale heat transfer process taken between nanoparticle and surrounding material, and can serve as the ground stone for future nanobubble research based on microscopic theory, such as molecular dynamics.

Plasmonic nanoclusters, an ordered assembly of coupled metallic nanoparticles, support unique spectral features known as Fano resonances (FR)[1-4] due to the cou-

pling between their subradiant and superradiant plasmon modes. Within the Fano resonance, absorption is significantly enhanced, giving rise to highly localized, intense near fields with the potential to enhance nonlinear optical processes [5,6]. A structure supporting the coherent oscillation of two distinct FRs within an individual plasmonic nanocluster has been reported. We show how this coherence enhances the optical Four-Wave Mixing (FWM) process, in comparison to other double-resonant plasmonic clusters that lack this specific property. A model that explains the observed FWM features is proposed, based on the intense local fields at the nanocluster surfaces, which is generally applicable to any third-order processes in plasmonic nanostructures. With a larger effective susceptibility  $\chi^{(3)}$  relative to existing nonlinear optical materials, this coherent double-resonant nanocluster offers a new strategy for designing high-performance third-order nonlinear optical media.

## Bibliography

- [1] Z. Fang, Y.-R. Zhen, L. Fan, X. Zhu, and P. Nordlander, “Tunable wide-angle plasmonic perfect absorber at visible frequencies,” *Phys. Rev. B*, vol. 85, p. 245401, Jun 2012.
- [2] L. J. E. Anderson, C. M. Payne, Y. R. Zhen, P. Nordlander, and J. H. Hafner, “A tunable plasmon resonance in gold nanobelts,” *Nano Letters*, vol. 11, no. 11, pp. 5034–5037, 2011.
- [3] Z. Fang, Y.-R. Zhen, O. Neumann, A. Polman, J. Garca de Abajo, P. Nordlander, and N. J. Halas, “Evolution of light-induced vapor generation at a liquid-immersed metallic nanoparticle,” *Nano Letters*, vol. 0, no. ja, p. null, 0.
- [4] E. Prodan, C. Radloff, N. J. Halas, and P. Nordlander, “A hybridization model for the plasmon response of complex nanostructures,” *Science*, vol. 302, no. 5644, pp. 419–422, 2003.
- [5] T. W. Ebbesen, H. J. Lezec, H. F. Ghaemi, T. Thio, and P. A. Wolff, “Extraordinary optical transmission through sub-wavelength hole arrays,” *Nature*, vol. 391, no. 6668, pp. 667–669, 1998.
- [6] W. L. Barnes, A. Dereux, and T. W. Ebbesen, “Surface plasmon subwavelength

- optics,” *Nature*, vol. 424, no. 6950, pp. 824–830, 2003.
- [7] J. B. Pendry, L. Martin-Moreno, and F. J. Garcia-Vidal, “Mimicking surface plasmons with structured surfaces,” *Science*, vol. 305, no. 5685, pp. 847–848, 2004.
- [8] M. W. Knight, H. Sobhani, P. Nordlander, and N. J. Halas, “Photodetection with active optical antennas,” *Science*, vol. 332, no. 6030, pp. 702–704, 2011.
- [9] S. Lal, S. E. Clare, and N. J. Halas, “Nanoshell-enabled photothermal cancer therapy: Impending clinical impact,” *Accounts of Chemical Research*, vol. 41, no. 12, pp. 1842–1851, 2008.
- [10] D. Lapotko, “Plasmonic nanoparticle-generated photothermal bubbles and their biomedical applications,” *Nanomedicine*, vol. 4, no. 7, pp. 813–845, 2009.
- [11] A. M. Gobin, M. H. Lee, N. J. Halas, W. D. James, R. A. Drezek, and J. L. West, “Near-infrared resonant nanoshells for combined optical imaging and photothermal cancer therapy,” *Nano Letters*, vol. 7, no. 7, pp. 1929–1934, 2007.
- [12] C. Loo, A. Lowery, N. J. Halas, J. West, and R. Drezek, “Immunotargeted nanoshells for integrated cancer imaging and therapy,” *Nano Letters*, vol. 5, no. 4, pp. 709–711, 2005.
- [13] C. Loo, A. Lin, L. Hirsch, M. H. Lee, J. Barton, N. J. Halas, J. West, and R. Drezek, “Nanoshell-enabled photonics-based imaging and therapy of cancer,”



- Technology in Cancer Research and Treatment*, vol. 3, no. 1, pp. 33–40, 2004.
- [14] K. J. K. Koerkamp, S. Enoch, F. B. Segerink, N. F. van Hulst, and L. Kuipers, “Strong influence of hole shape on extraordinary transmission through periodic arrays of subwavelength holes,” *Physical Review Letters*, vol. 92, no. 18, 2004.
- [15] K. L. van der Molen, F. B. Segerink, N. F. van Hulst, and L. Kuipers, “Influence of hole size on the extraordinary transmission through subwavelength hole arrays,” *Applied Physics Letters*, vol. 85, no. 19, pp. 4316–4318, 2004.
- [16] K. L. van der Molen, K. J. Klein Koerkamp, S. Enoch, F. B. Segerink, N. F. van Hulst, and L. Kuipers, “Role of shape and localized resonances in extraordinary transmission through periodic arrays of subwavelength holes: Experiment and theory,” *Physical Review B*, vol. 72, no. 4, 2005.
- [17] T. V. Teperik, F. J. G. de Abajo, V. V. Popov, and M. S. Shur, “Strong terahertz absorption bands in a scaled plasmonic crystal,” *Applied Physics Letters*, vol. 90, no. 25, 2007.
- [18] T. V. Teperik, F. J. G. de Abajo, A. G. Borisov, M. Abdelsalam, P. N. Bartlett, Y. Sugawara, and J. J. Baumberg, “Omnidirectional absorption in nanostructured metal surfaces,” *Nature Photonics*, vol. 2, no. 5, pp. 299–301, 2008.
- [19] S. H. Mousavi, A. B. Khanikaev, B. Neuner, Y. Avitzour, D. Korobkin, G. Ferro, and G. Shvets, “Highly confined hybrid spoof surface plasmons in ultrathin

- metal-dielectric heterostructures,” *Physical Review Letters*, vol. 105, no. 17, 2010.
- [20] M. Diem, T. Koschny, and C. M. Soukoulis, “Wide-angle perfect absorber/thermal emitter in the terahertz regime,” *Physical Review B*, vol. 79, no. 3, 2009.
- [21] N. Liu, M. Mesch, T. Weiss, M. Hentschel, and H. Giessen, “Infrared perfect absorber and its application as plasmonic sensor,” *Nano Letters*, vol. 10, no. 7, pp. 2342–2348, 2010.
- [22] P. Spinelli, M. A. Verschuuren, and A. Polman, “Broadband omnidirectional antireflection coating based on subwavelength surface mie resonators,” *Nature Communications*, vol. 3, 2012.
- [23] K. Aydin, V. E. Ferry, R. M. Briggs, and H. A. Atwater, “Broadband polarization-independent resonant light absorption using ultrathin plasmonic super absorbers,” *Nature Communications*, vol. 2, 2011.
- [24] K. Nakayama, K. Tanabe, and H. A. Atwater, “Plasmonic nanoparticle enhanced light absorption in gaas solar cells,” *Applied Physics Letters*, vol. 93, no. 12, 2008.
- [25] H. A. Atwater and A. Polman, “Plasmonics for improved photovoltaic devices,” *Nature Materials*, vol. 9, no. 3, pp. 205–213, 2010.

- [26] Y. Avitzour, Y. A. Urzhumov, and G. Shvets, “Wide-angle infrared absorber based on a negative-index plasmonic metamaterial,” *Physical Review B*, vol. 79, no. 4, 2009.
- [27] A. Tittl, P. Mai, R. Taubert, D. Dregely, N. Liu, and H. Giessen, “Palladium-based plasmonic perfect absorber in the visible wavelength range and its application to hydrogen sensing,” *Nano Letters*, vol. 11, no. 10, pp. 4366–4369, 2011.
- [28] V. Kotaidis, C. Dahmen, G. von Plessen, F. Springer, and A. Plech, “Excitation of nanoscale vapor bubbles at the surface of gold nanoparticles in water,” *Journal of Chemical Physics*, vol. 124, no. 18, 2006.
- [29] D. Lapotko, “Optical excitation and detection of vapor bubbles around plasmonic nanoparticles,” *Optics Express*, vol. 17, no. 4, pp. 2538–2556, 2009.
- [30] A. Plech, V. Kotaidis, S. Gresillon, C. Dahmen, and G. von Plessen, “Laser-induced heating and melting of gold nanoparticles studied by time-resolved x-ray scattering,” *Physical Review B*, vol. 70, no. 19, 2004.
- [31] A. O. Govorov and H. H. Richardson, “Generating heat with metal nanoparticles,” *Nano Today*, vol. 2, no. 1, pp. 30–38, 2007.
- [32] O. Neumann, A. S. Urban, J. Day, S. Lal, P. Nordlander, and N. J. Halas, “Solar vapor generation enabled by nanoparticles,” *ACS Nano*, vol. 7, no. 1, pp. 42–49, 2013.

- [33] Y. R. Fang, Z. P. Li, Y. Z. Huang, S. P. Zhang, P. Nordlander, N. J. Halas, and H. X. Xu, “Branched silver nanowires as controllable plasmon routers,” *Nano Letters*, vol. 10, no. 5, pp. 1950–1954, 2010.
- [34] D. Solis, W.-S. Chang, B. P. Khanal, K. Bao, P. Nordlander, E. R. Zubarev, and S. Link, “Bleach-imaged plasmon propagation (blipp) in single gold nanowires,” *Nano Letters*, vol. 10, no. 9, pp. 3482–3485, 2010.
- [35] A. Paul, D. Solis, K. Bao, W.-S. Chang, S. Nauert, L. Vidgerman, E. R. Zubarev, P. Nordlander, and S. Link, “Identification of higher order long-propagation-length surface plasmon polariton modes in chemically prepared gold nanowires,” *Acs Nano*, vol. 6, no. 9, pp. 8105–8113, 2012.
- [36] B. Wild, L. Cao, Y. Sun, B. P. Khanal, E. R. Zubarev, S. K. Gray, N. F. Scherer, and M. Pelton, “Propagation lengths and group velocities of plasmons in chemically synthesized gold and silver nanowires,” *ACS Nano*, vol. 6, no. 1, pp. 472–482, 2012.
- [37] S. Zhang and H. Xu, “Optimizing substrate-mediated plasmon coupling toward high-performance plasmonic nanowire waveguides,” *ACS Nano*, vol. 6, no. 9, pp. 8128–8135, 2012.
- [38] P. Kusar, C. Gruber, A. Hohenau, and J. R. Krenn, “Measurement and reduction of damping in plasmonic nanowires,” *Nano Letters*, vol. 12, no. 2, pp. 661–665, 2012.

- [39] R. M. Dickson and L. A. Lyon, “Unidirectional plasmon propagation in metallic nanowires,” *Journal of Physical Chemistry B*, vol. 104, no. 26, pp. 6095–6098, 2000.
- [40] Z. P. Li, K. Bao, Y. R. Fang, Z. Q. Guan, N. J. Halas, P. Nordlander, and H. X. Xu, “Effect of a proximal substrate on plasmon propagation in silver nanowires,” *Physical Review B*, vol. 82, no. 24, 2010.
- [41] H. Ditlbacher, A. Hohenau, D. Wagner, U. Kreibig, M. Rogers, F. Hofer, F. R. Aussenegg, and J. R. Krenn, “Silver nanowires as surface plasmon resonators,” *Physical Review Letters*, vol. 95, no. 25, p. 257403, 2005.
- [42] Z. Y. Fang, Y. M. Wang, Z. Liu, A. Schlather, P. M. Ajayan, F. H. L. Koppens, P. Nordlander, and N. J. Halas, “Plasmon-induced doping of graphene,” *Acs Nano*, vol. 6, no. 11, pp. 10222–10228, 2012.
- [43] Z. Y. Fang, Z. Liu, Y. M. Wang, P. M. Ajayan, P. Nordlander, and N. J. Halas, “Graphene-antenna sandwich photodetector,” *Nano Letters*, vol. 12, no. 7, pp. 3808–3813, 2012.
- [44] S. Mukherjee, F. Libisch, N. Large, O. Neumann, L. V. Brown, J. Cheng, J. B. Lassiter, E. A. Carter, P. Nordlander, and N. J. Halas, “Hot electrons do the impossible: Plasmon-induced dissociation of  $\text{H}_2$  on Au,” *Nano Letters*, vol. 13, no. 1, pp. 240–247, 2013.

- [45] J. J. Burke, G. I. Stegeman, and T. Tamir, “Surface-polariton-like waves guided by thin, lossy metal-films,” *Physical Review B*, vol. 33, no. 8, pp. 5186–5201, 1986.
- [46] E. N. Economou, “Surface plasmons in thin films,” *Physical Review*, vol. 182, no. 2, p. 539, 1969.
- [47] J. M. Pitarke, V. M. Silkin, E. V. Chulkov, and P. M. Echenique, “Theory of surface plasmons and surface-plasmon polaritons,” *Reports on Progress in Physics*, vol. 70, no. 1, pp. 1–87, 2007.
- [48] Y. Luo, J. B. Pendry, and A. Aubry, “Surface plasmons and singularities,” *Nano Letters*, vol. 10, no. 10, pp. 4186–4191, 2010.
- [49] A. Aubry, D. Y. Lei, S. A. Maier, and J. B. Pendry, “Conformal transformation applied to plasmonics beyond the quasistatic limit,” *Physical Review B*, vol. 82, no. 20, 2010.
- [50] A. Aubry, D. Y. Lei, S. A. Maier, and J. B. Pendry, “Broadband plasmonic device concentrating the energy at the nanoscale: The crescent-shaped cylinder,” *Physical Review B*, vol. 82, no. 12, 2010.
- [51] A. Aubry, D. Y. Lei, S. A. Maier, and J. B. Pendry, “Interaction between plasmonic nanoparticles revisited with transformation optics,” *Physical Review Letters*, vol. 105, no. 23, 2010.

- [52] P. Berini, “Plasmon-polariton modes guided by a metal film of finite width,” *Optics Letters*, vol. 24, no. 15, pp. 1011–1013, 1999.
- [53] P. Berini, “Plasmon-polariton waves guided by thin lossy metal films of finite width: Bound modes of symmetric structures,” *Physical Review B*, vol. 61, no. 15, pp. 10484–10503, 2000.
- [54] P. Berini, “Plasmon-polariton waves guided by thin lossy metal films of finite width: Bound modes of asymmetric structures,” *Physical Review B*, vol. 63, no. 12, pp. art. no.–125417, 2001.
- [55] R. Charbonneau, P. Berini, E. Berolo, and E. Lisicka-Shrzek, “Experimental observation of plasmon-polariton waves supported by a thin metal film of finite width,” *Optics Letters*, vol. 25, no. 11, pp. 844–846, 2000.
- [56] R. Charbonneau and N. Lahoud, “Demonstration of integrated optics elements based on long-ranging surface plasmon polaritons,” *Optics Express*, vol. 13, no. 3, pp. 977–984, 2005.
- [57] M. A. Noginov, G. Zhu, M. Mayy, B. A. Ritzo, N. Noginova, and V. A. Podolskiy, “Stimulated emission of surface plasmon polaritons,” *Physical Review Letters*, vol. 101, no. 22, p. 226806, 2008.
- [58] M. A. Noginov, V. A. Podolskiy, G. Zhu, M. Mayy, M. Bahoura, J. A. Adegoke, B. A. Ritzo, and K. Reynolds, “Compensation of loss in propagating sur-

- face plasmon polariton by gain in adjacent dielectric medium,” *Optics Express*, vol. 16, no. 2, pp. 1385–1392, 2008.
- [59] M. A. Noginov, “Compensation of surface plasmon loss by gain in dielectric medium,” *Journal of Nanophotonics*, vol. 2, 2008.
- [60] R. Marani, A. D’Orazio, V. Petruzzelli, S. G. Rodrigo, L. Martin-Moreno, F. J. Garcia-Vidal, and J. Bravo-Abad, “Gain-assisted extraordinary optical transmission through periodic arrays of subwavelength apertures,” *New Journal of Physics*, vol. 14, 2012.
- [61] X. L. Zhong and Z. Y. Li, “Plasmon enhanced light amplification in metal-insulator-metal waveguides with gain,” *Journal of Optics*, vol. 14, no. 5, 2012.
- [62] X. J. Zhang, Y. C. Li, T. Li, S. Y. Lee, C. G. Feng, L. B. Wang, and T. Mei, “Gain-assisted propagation of surface plasmon polaritons via electrically pumped quantum wells,” *Optics Letters*, vol. 35, no. 18, pp. 3075–3077, 2010.
- [63] X. Zhang, H. T. Liu, and Y. Zhong, “Compensation of propagation loss of surface plasmon polaritons with a finite-thickness dielectric gain layer,” *Journal of Optics*, vol. 14, no. 12, 2012.
- [64] S. C. Russev, G. G. Tsutsumanova, and A. N. Tzonev, “Conditions for loss compensation of surface plasmon polaritons propagation on a metal/gain medium boundary,” *Plasmonics*, vol. 7, no. 1, pp. 151–157, 2012.



- [65] R. J. Rao and T. T. Tang, “Study of an active hybrid gap surface plasmon polariton waveguide with nanoscale confinement size and low compensation gain,” *Journal of Physics D-Applied Physics*, vol. 45, no. 24, 2012.
- [66] I. P. Radko, M. G. Nielsen, O. Albrektsen, and S. I. Bozhevolnyi, “Stimulated emission of surface plasmon polaritons by lead-sulphide quantum dots at near infra-red wavelengths,” *Optics Express*, vol. 18, no. 18, pp. 18633–18641, 2010.
- [67] X. G. Luo and L. S. Yan, “Surface plasmon polaritons and its applications,” *Ieee Photonics Journal*, vol. 4, no. 2, pp. 590–595, 2012.
- [68] J. K. Kitur, V. A. Podolskiy, and M. A. Noginov, “Stimulated emission of surface plasmon polaritons in a microcylinder cavity,” *Physical Review Letters*, vol. 106, no. 18, 2011.
- [69] V. V. Ivanov, “Slow surface plasmons in amplifying media and ultrahigh-resolution nonlinear optical microscopy,” *Journal of Surface Investigation-X-Ray Synchrotron and Neutron Techniques*, vol. 3, no. 4, pp. 507–512, 2009.
- [70] S. M. Garcia-Blanco, M. Pollnau, and S. I. Bozhevolnyi, “Loss compensation in long-range dielectric-loaded surface plasmon-polariton waveguides,” *Optics Express*, vol. 19, no. 25, pp. 25298–25310, 2011.
- [71] C. Garcia, V. Coello, Z. Han, I. P. Radko, and S. I. Bozhevolnyi, “Partial loss compensation in dielectric-loaded plasmonic waveguides at near infra-red wavelengths,” *Optics Express*, vol. 20, no. 7, pp. 7771–7776, 2012.

- [72] A. R. Davoyan, I. V. Shadrivov, Y. S. Kivshar, and D. K. Gramotnev, “Optimal tapers for compensating losses in plasmonic waveguides,” *Physica Status Solidi-Rapid Research Letters*, vol. 4, no. 10, pp. 277–279, 2010.
- [73] I. De Leon and P. Berini, “Amplification of long-range surface plasmons by a dipolar gain medium,” *Nature Photonics*, vol. 4, no. 6, pp. 382–387, 2010.
- [74] F. J. G. de Abajo, “Multiple scattering of radiation in clusters of dielectrics,” *Physical Review B*, vol. 60, no. 8, pp. 6086–6102, 1999.
- [75] V. Myroshnychenko, J. Rodriguez-Fernandez, I. Pastoriza-Santos, A. M. Funston, C. Novo, P. Mulvaney, L. M. Liz-Marzan, and F. J. G. de Abajo, “Modelling the optical response of gold nanoparticles,” *Chemical Society Reviews*, vol. 37, no. 9, pp. 1792–1805, 2008.
- [76] P. K. Jain, K. S. Lee, I. H. El-Sayed, and M. A. El-Sayed, “Calculated absorption and scattering properties of gold nanoparticles of different size, shape, and composition: Applications in biological imaging and biomedicine,” *Journal Of Physical Chemistry B*, vol. 110, no. 14, pp. 7238–7248, 2006.
- [77] P. K. Jain and M. A. El-Sayed, “Universal scaling of plasmon coupling in metal nanostructures: Extension from particle pairs to nanoshells,” *Nano Letters*, vol. 7, no. 9, pp. 2854–2858, 2007.
- [78] C. Radloff and N. J. Halas, “Plasmonic properties of concentric nanoshells,” *Nano Letters*, vol. 4, no. 7, pp. 1323–1327, 2004.

- [79] R. Bardhan, S. Mukherjee, N. A. Mirin, S. D. Levit, P. Nordlander, and N. J. Halas, “Nanosphere-in-a-nanoshell: A simple nanomatryushka,” *Journal of Physical Chemistry C*, vol. 114, no. 16, pp. 7378–7383, 2010.
- [80] E. Hao and G. C. Schatz, “Electromagnetic fields around silver nanoparticles and dimers,” *Journal of Chemical Physics*, vol. 120, no. 1, pp. 357–366, 2004.
- [81] P. Nordlander, C. Oubre, E. Prodan, K. Li, and M. I. Stockman, “Plasmon hybridization in nanoparticle dimers,” *Nano Letters*, vol. 4, no. 5, pp. 899–903, 2004.
- [82] C. Sonnichsen, B. M. Reinhard, J. Liphardt, and A. P. Alivisatos, “A molecular ruler based on plasmon coupling of single gold and silver nanoparticles,” *Nature Biotechnology*, vol. 23, no. 6, pp. 741–745, 2005.
- [83] C. E. Talley, J. B. Jackson, C. Oubre, N. K. Grady, C. W. Hollars, S. M. Lane, T. R. Huser, P. Nordlander, and N. J. Halas, “Surface-enhanced raman scattering from individual au nanoparticles and nanoparticle dimer substrates,” *Nano Letters*, vol. 5, no. 8, pp. 1569–1574, 2005.
- [84] L. Gunnarsson, T. Rindzevicius, J. Prikulis, B. Kasemo, M. Kall, S. L. Zou, and G. C. Schatz, “Confined plasmons in nanofabricated single silver particle pairs: Experimental observations of strong interparticle interactions,” *Journal Of Physical Chemistry B*, vol. 109, no. 3, pp. 1079–1087, 2005.

- [85] P. K. Jain, S. Eustis, and M. A. El-Sayed, "Plasmon coupling in nanorod assemblies: Optical absorption, discrete dipole approximation simulation, and exciton-coupling model," *Journal Of Physical Chemistry B*, vol. 110, no. 37, pp. 18243–18253, 2006.
- [86] H. Wang, D. W. Brandl, P. Nordlander, and N. J. Halas, "Plasmonic nanostructures: Artificial molecules," *Accounts of Chemical Research*, vol. 40, no. 1, pp. 53–62, 2007.
- [87] D. W. Brandl, N. A. Mirin, and P. Nordlander, "Plasmon modes of nanosphere trimers and quadrumers," *Journal Of Physical Chemistry B*, vol. 110, no. 25, pp. 12302–12310, 2006.
- [88] P. K. Jain and M. A. El-Sayed, "Surface plasmon coupling and its universal size scaling in metal nanostructures of complex geometry: Elongated particle pairs and nanosphere trimers," *Journal of Physical Chemistry C*, vol. 112, no. 13, pp. 4954–4960, 2008.
- [89] J. A. Fan, K. Bao, C. H. Wu, J. M. Bao, R. Bardhan, N. J. Halas, V. N. Manoharan, G. Shvets, P. Nordlander, and F. Capasso, "Fano-like interference in self-assembled plasmonic quadramer clusters," *Nano Letters*, vol. 10, no. 11, pp. 4680–4685, 2010.
- [90] N. A. Mirin, K. Bao, and P. Nordlander, "Fano resonances in plasmonic nanoparticle aggregates," *Journal of Physical Chemistry A*, vol. 113, no. 16,

pp. 4028–4034, 2009.

- [91] J. A. Fan, C. H. Wu, K. Bao, J. M. Bao, R. Bardhan, N. J. Halas, V. N. Manoharan, P. Nordlander, G. Shvets, and F. Capasso, “Self-assembled plasmonic nanoparticle clusters,” *Science*, vol. 328, no. 5982, pp. 1135–1138, 2010.
- [92] S. Eustis and M. A. El-Sayed, “Why gold nanoparticles are more precious than pretty gold: Noble metal surface plasmon resonance and its enhancement of the radiative and nonradiative properties of nanocrystals of different shapes,” *Chemical Society Reviews*, vol. 35, no. 3, pp. 209–217, 2006.
- [93] A. J. Haes and R. P. Van Duyne, “A nanoscale optical biosensor: Sensitivity and selectivity of an approach based on the localized surface plasmon resonance spectroscopy of triangular silver nanoparticles,” *Journal of the American Chemical Society*, vol. 124, no. 35, pp. 10596–10604, 2002.
- [94] C. L. Haynes and R. P. Van Duyne, “Nanosphere lithography: A versatile nanofabrication tool for studies of size-dependent nanoparticle optics,” *Journal Of Physical Chemistry B*, vol. 105, no. 24, pp. 5599–5611, 2001.
- [95] K. L. Kelly, E. Coronado, L. L. Zhao, and G. C. Schatz, “The optical properties of metal nanoparticles: The influence of size, shape, and dielectric environment,” *Journal Of Physical Chemistry B*, vol. 107, no. 3, pp. 668–677, 2003.

- [96] L. M. Liz-Marzan, "Tailoring surface plasmons through the morphology and assembly of metal nanoparticles," *Langmuir*, vol. 22, no. 1, pp. 32–41, 2006.
- [97] A. D. McFarland and R. P. Van Duyne, "Single silver nanoparticles as real-time optical sensors with zeptomole sensitivity," *Nano Letters*, vol. 3, no. 8, pp. 1057–1062, 2003.
- [98] Z. Q. Tian, B. Ren, and D. Y. Wu, "Surface-enhanced raman scattering: From noble to transition metals and from rough surfaces to ordered nanostructures," *Journal Of Physical Chemistry B*, vol. 106, no. 37, pp. 9463–9483, 2002.
- [99] K. A. Willets and R. P. Van Duyne, "Localized surface plasmon resonance spectroscopy and sensing," *Annual Review of Physical Chemistry*, vol. 58, pp. 267–297, 2007.
- [100] A. Brioude and M. P. Pileni, "Silver nanodisks: Optical properties study using the discrete dipole approximation method," *Journal Of Physical Chemistry B*, vol. 109, no. 49, pp. 23371–23377, 2005.
- [101] C. Hagglund, M. Zach, G. Petersson, and B. Kasemo, "Electromagnetic coupling of light into a silicon solar cell by nanodisk plasmons," *Applied Physics Letters*, vol. 92, no. 5, 2008.
- [102] P. Hanarp, M. Kall, and D. S. Sutherland, "Optical properties of short range ordered arrays of nanometer gold disks prepared by colloidal lithography," *Journal Of Physical Chemistry B*, vol. 107, no. 24, pp. 5768–5772, 2003.

- [103] E. C. Hao, K. L. Kelly, J. T. Hupp, and G. C. Schatz, "Synthesis of silver nanodisks using polystyrene mesospheres as templates," *Journal of the American Chemical Society*, vol. 124, no. 51, pp. 15182–15183, 2002.
- [104] V. K. S. Hsiao, Y. B. Zheng, B. K. Juluri, and T. J. Huang, "Light-driven plasmonic switches based on au nanodisk arrays and photoresponsive liquid crystals," *Advanced Materials*, vol. 20, no. 18, pp. 3528–+, 2008.
- [105] M. Maillard, S. Giorgio, and M. P. Pileni, "Tuning the size of silver nanodisks with similar aspect ratios: Synthesis and optical properties," *Journal Of Physical Chemistry B*, vol. 107, no. 11, pp. 2466–2470, 2003.
- [106] M. Maillard, P. R. Huang, and L. Brus, "Silver nanodisk growth by surface plasmon enhanced photoreduction of adsorbed  $ag^+$ ," *Nano Letters*, vol. 3, no. 11, pp. 1611–1615, 2003.
- [107] Q. Yu, P. Guan, D. Qin, G. Golden, and P. M. Wallace, "Inverted size-dependence of surface-enhanced raman scattering on gold nanohole and nanodisk arrays," *Nano Letters*, vol. 8, no. 7, pp. 1923–1928, 2008.
- [108] Y. B. Zheng, Y.-W. Yang, L. Jensen, L. Fang, B. K. Juluri, A. H. Flood, P. S. Weiss, J. F. Stoddart, and T. J. Huang, "Active molecular plasmonics: Controlling plasmon resonances with molecular switches," *Nano Letters*, vol. 9, no. 2, pp. 819–825, 2009.

- [109] F. Hao, C. L. Nehl, J. H. Hafner, and P. Nordlander, “Plasmon resonances of a gold nanostar,” *Nano Letters*, vol. 7, no. 3, pp. 729–732, 2007.
- [110] C. G. Khoury and T. Vo-Dinh, “Gold nanostars for surface-enhanced raman scattering: Synthesis, characterization and optimization,” *Journal of Physical Chemistry C*, vol. 112, no. 48, pp. 18849–18859, 2008.
- [111] E. N. Esenturk and A. R. H. Walker, “Surface-enhanced raman scattering spectroscopy via gold nanostars,” *Journal of Raman Spectroscopy*, vol. 40, no. 1, pp. 86–91, 2009.
- [112] S. K. Dondapati, T. K. Sau, C. Hrelescu, T. A. Klar, F. D. Stefani, and J. Feldmann, “Label-free biosensing based on single gold nanostars as plasmonic transducers,” *Acs Nano*, vol. 4, no. 11, pp. 6318–6322, 2010.
- [113] S. Barbosa, A. Agrawal, L. Rodriguez-Lorenzo, I. Pastoriza-Santos, R. A. Alvarez-Puebla, A. Kornowski, H. Weller, and L. M. Liz-Marzan, “Tuning size and sensing properties in colloidal gold nanostars,” *Langmuir*, vol. 26, no. 18, pp. 14943–14950, 2010.
- [114] H. Wang, D. W. Brandl, F. Le, P. Nordlander, and N. J. Halas, “Nanorice: A hybrid plasmonic nanostructure,” *Nano Letters*, vol. 6, no. 4, pp. 827–832, 2006.
- [115] B. J. Wiley, Y. Chen, J. M. McLellan, Y. Xiong, Z.-Y. Li, D. Ginger, and



- Y. Xia, “Synthesis and optical properties of silver nanobars and nanorice,” *Nano Letters*, vol. 7, no. 4, pp. 1032–1036, 2007.
- [116] H. Wei, A. Reyes-Coronado, P. Nordlander, J. Aizpurua, and H. Xu, “Multipolar plasmon resonances in individual ag nanorice,” *Acs Nano*, vol. 4, no. 5, pp. 2649–2654, 2010.
- [117] N. S. King, Y. Li, C. Ayala-Orozco, T. Brannan, P. Nordlander, and N. J. Halas, “Angle- and spectral-dependent light scattering from plasmonic nanocups,” *Acs Nano*, vol. 5, no. 9, pp. 7254–7262, 2011.
- [118] J. B. Lassiter, M. W. Knight, N. A. Mirin, and N. J. Halas, “Reshaping the plasmonic properties of an individual nanoparticle,” *Nano Letters*, vol. 9, no. 12, pp. 4326–4332, 2009.
- [119] Y. Zhang, A. Barhoum, J. B. Lassiter, and N. J. Halas, “Orientation-preserving transfer and directional light scattering from individual light-bending nanoparticles,” *Nano Letters*, vol. 11, no. 4, pp. 1838–1844, 2011.
- [120] Y. Zhang, N. K. Grady, C. Ayala-Orozco, and N. J. Halas, “Three-dimensional nanostructures as highly efficient generators of second harmonic light,” *Nano Letters*, vol. 11, no. 12, pp. 5519–5523, 2011.
- [121] M. Durach, A. Rusina, and M. I. Stockman, “Toward full spatiotemporal control on the nanoscale,” *Nano Letters*, vol. 7, no. 10, pp. 3145–3149, 2007.

- [122] J. L. West and N. J. Halas, “Engineered nanomaterials for biophotonics applications: Improving sensing, imaging, and therapeutics,” *Annual Review of Biomedical Engineering*, vol. 5, pp. 285–292, 2003.
- [123] P. Nagpal, N. C. Lindquist, S. H. Oh, and D. J. Norris, “Ultrasmooth patterned metals for plasmonics and metamaterials,” *Science*, vol. 325, no. 5940, pp. 594–597, 2009.
- [124] N. J. Halas, S. Lal, W. S. Chang, S. Link, and P. Nordlander, “Plasmons in strongly coupled metallic nanostructures,” *Chemical Reviews*, vol. 111, no. 6, pp. 3913–3961, 2011.
- [125] J. B. Jackson and N. J. Halas, “Surface-enhanced raman scattering on tunable plasmonic nanoparticle substrates,” *Proceedings of the National Academy of Sciences of the United States of America*, vol. 101, no. 52, pp. 17930–17935, 2004.
- [126] K. Wang, E. Schonbrun, P. Steinvurzel, and K. B. Crozier, “Trapping and rotating nanoparticles using a plasmonic nano-tweezer with an integrated heat sink,” *Nature Communications*, vol. 2, 2011.
- [127] R. Buckley and P. Berini, “Figures of merit for 2d surface plasmon waveguides and application to metal stripes,” *Optics Express*, vol. 15, no. 19, pp. 12174–12182, 2007.

- [128] C. Tserkezis, G. Gantzounis, and N. Stefanou, “Collective plasmonic modes in ordered assemblies of metallic nanoshells,” *Journal of Physics-Condensed Matter*, vol. 20, no. 7, 2008.
- [129] Y. R. Zhen, K. H. Fung, and C. T. Chan, “Collective plasmonic modes in two-dimensional periodic arrays of metal nanoparticles,” *Physical Review B*, vol. 78, no. 3, 2008.
- [130] S. C. Kitson, W. L. Barnes, and J. R. Sambles, “Full photonic band gap for surface modes in the visible,” *Physical Review Letters*, vol. 77, no. 13, pp. 2670–2673, 1996.
- [131] Z. Y. Fang, C. F. Lin, R. M. Ma, S. Huang, and X. Zhu, “Planar plasmonic focusing and optical transport using us nanoribbon,” *Acs Nano*, vol. 4, no. 1, pp. 75–82, 2010.
- [132] C. H. Wu, B. Neuner, G. Shvets, J. John, A. Milder, B. Zollars, and S. Savoy, “Large-area wide-angle spectrally selective plasmonic absorber,” *Physical Review B*, vol. 84, no. 7, 2011.
- [133] S. I. Bozhevolnyi, J. Erland, K. Leosson, P. M. W. Skovgaard, and J. M. Hvam, “Waveguiding in surface plasmon polariton band gap structures,” *Physical Review Letters*, vol. 86, no. 14, pp. 3008–3011, 2001.
- [134] P. Lalanne, C. Sauvan, J. P. Hugonin, J. C. Rodier, and P. Chavel, “Perturbative approach for surface plasmon effects on flat interfaces periodically

- corrugated by subwavelength apertures,” *Physical Review B*, vol. 68, no. 12, 2003.
- [135] H. T. Liu and P. Lalanne, “Microscopic theory of the extraordinary optical transmission,” *Nature*, vol. 452, no. 7188, pp. 728–731, 2008.
- [136] S. G. Tikhodeev, A. L. Yablonskii, E. A. Muljarov, N. A. Gippius, and T. Ishihara, “Quasiguidded modes and optical properties of photonic crystal slabs,” *Physical Review B*, vol. 66, no. 4, 2002.
- [137] G. Gantzounis and N. Stefanou, “Cavity-plasmon waveguides: Multiple scattering calculations of dispersion in weakly coupled dielectric nanocavities in a metallic host material,” *Physical Review B*, vol. 74, no. 8, p. 085102, 2006.
- [138] G. Gantzounis and N. Stefanou, “Layer-multiple-scattering method for photonic crystals of nonspherical particles,” *Physical Review B*, vol. 73, no. 3, p. 035115, 2006.
- [139] Z. Q. Niu, Y. R. Zhen, M. Gong, Q. Peng, P. Nordlander, and Y. D. Li, “Pd nanocrystals with single-, double-, and triple-cavities: facile synthesis and tunable plasmonic properties,” *Chemical Science*, vol. 2, no. 12, pp. 2392–2395, 2011.
- [140] J. D. Joannopoulos, *Photonic crystals : molding the flow of light*. Princeton: Princeton University Press, 2nd ed., 2008.

- [141] P. B. Johnson and R. W. Christy, “Optical constants of noble metals,” *Physical Review B*, vol. 6, no. 12, pp. 4370–4379, 1972.
- [142] E. Verhagen, J. A. Dionne, L. Kuipers, H. A. Atwater, and A. Polman, “Near-field visualization of strongly confined surface plasmon polaritons in metal-insulator-metal waveguides,” *Nano Letters*, vol. 8, no. 9, pp. 2925–2929, 2008.
- [143] S. Link and M. A. El-Sayed, “Shape and size dependence of radiative, non-radiative and photothermal properties of gold nanocrystals,” *International Reviews in Physical Chemistry*, vol. 19, no. 3, pp. 409–453, 2000.
- [144] M. B. Cortie and A. M. McDonagh, “Synthesis and optical properties of hybrid and alloy plasmonic nanoparticles,” *Chemical Reviews*, vol. 111, no. 6, pp. 3713–3735, 2011.
- [145] M. Rycenga, C. M. Cobley, J. Zeng, W. Y. Li, C. H. Moran, Q. Zhang, D. Qin, and Y. Xia, “Controlling the synthesis and assembly of silver nanostructures for plasmonic applications,” *Chemical Reviews*, vol. 111, no. 6, pp. 3669–3712, 2011.
- [146] H. W. Liao, C. L. Nehl, and J. H. Hafner, “Biomedical applications of plasmon resonant metal nanoparticles,” *Nanomedicine*, vol. 1, no. 2, pp. 201–208, 2006.
- [147] L. R. Hirsch, A. M. Gobin, A. R. Lowery, F. Tam, R. A. Drezek, N. J. Halas, and J. L. West, “Metal nanoshells,” *Annals Of Biomedical Engineering*, vol. 34, no. 1, pp. 15–22, 2006.

- [148] S. E. Lee and L. P. Lee, “Biomolecular plasmonics for quantitative biology and nanomedicine,” *Current Opinion in Biotechnology*, vol. 21, no. 4, pp. 489–497, 2010.
- [149] S. Schlcker, “Sers microscopy: Nanoparticle probes and biomedical applications,” *ChemPhysChem*, vol. 10, no. 9-10, p. 1344, 2009.
- [150] R. S. Golightly, W. E. Doering, and M. J. Natan, “Surface-enhanced raman spectroscopy and homeland security: A perfect match?,” *Acs Nano*, vol. 3, no. 10, pp. 2859–2869, 2009.
- [151] V. Giannini, A. I. Fernandez-Dominguez, S. C. Heck, and S. A. Maier, “Plasmonic nanoantennas: Fundamentals and their use in controlling the radiative properties of nanoemitters,” *Chemical Reviews*, vol. 111, no. 6, pp. 3888–3912, 2011.
- [152] O. L. Muskens, V. Giannini, J. A. Sanchez-Gil, and J. G. Rivas, “Strong enhancement of the radiative decay rate of emitters by single plasmonic nanoantennas,” *Nano Letters*, vol. 7, no. 9, pp. 2871–2875, 2007.
- [153] A. Bouhelier, T. Huser, H. Tamaru, H. J. Guntherodt, D. W. Pohl, F. I. Baida, and D. Van Labeke, “Plasmon optics of structured silver films,” *Physical Review B*, vol. 63, no. 15, p. 155404, 2001.
- [154] A. W. Sanders, D. A. Routenberg, B. J. Wiley, Y. Xia, E. R. Dufresne, and

- M. A. Reed, "Observation of plasmon propagation, redirection, and fan-out in silver nanowires," *Nano Letters*, vol. 6, no. 8, pp. 1822–1826, 2006.
- [155] Z. P. Li, F. Hao, Y. Z. Huang, Y. R. Fang, P. Nordlander, and H. X. Xu, "Directional light emission from propagating surface plasmons of silver nanowires," *Nano Letters*, vol. 9, no. 12, pp. 4383–4386, 2009.
- [156] M. Z. Liu, T. W. Lee, S. K. Gray, P. Guyot-Sionnest, and M. Pelton, "Excitation of dark plasmons in metal nanoparticles by a localized emitter," *Physical Review Letters*, vol. 102, no. 10, p. 107401, 2009.
- [157] A. V. Akimov, A. Mukherjee, C. L. Yu, D. E. Chang, A. S. Zibrov, P. R. Hemmer, H. Park, and M. D. Lukin, "Generation of single optical plasmons in metallic nanowires coupled to quantum dots," *Nature*, vol. 450, no. 7168, pp. 402–406, 2007.
- [158] Y. Fedutik, V. V. Temnov, O. Schops, U. Woggon, and M. V. Artemyev, "Exciton-plasmon-photon conversion in plasmonic nanostructures," *Physical Review Letters*, vol. 99, no. 13, p. 136802, 2007.
- [159] D. E. Chang, A. S. Sorensen, P. R. Hemmer, and M. D. Lukin, "Strong coupling of single emitters to surface plasmons," *Physical Review B*, vol. 76, no. 3, p. 035420, 2007.
- [160] M. W. Knight, N. K. Grady, R. Bardhan, F. Hao, P. Nordlander, and N. J.

- Halas, “Nanoparticle-mediated coupling of light into a nanowire,” *Nano Letters*, vol. 7, no. 8, pp. 2346–2350, 2007.
- [161] N. Zhao, Y. Wei, N. J. Sun, Q. J. Chen, J. W. Bai, L. P. Zhou, Y. Qin, M. X. Li, and L. M. Qi, “Controlled synthesis of gold nanobelts and nanocombs in aqueous mixed surfactant solutions,” *Langmuir*, vol. 24, no. 3, pp. 991–998, 2008.
- [162] E. K. Payne, K. L. Shuford, S. Park, G. C. Schatz, and C. A. Mirkin, “Multipole plasmon resonances in gold nanorods,” *Journal of Physical Chemistry B*, vol. 110, no. 5, pp. 2150–2154, 2006.
- [163] G. W. Bryant, F. J. G. De Abajo, and J. Aizpurua, “Mapping the plasmon resonances of metallic nanoantennas,” *Nano Letters*, vol. 8, no. 2, pp. 631–636, 2008.
- [164] J. P. Berenger, “A perfectly matched layer for the absorption of electromagnetic waves,” *Journal of Computational Physics*, vol. 114, no. 2, pp. 185–200, 1994.
- [165] S. P. Zhang, H. Wei, K. Bao, U. Hakanson, N. J. Halas, P. Nordlander, and H. X. Xu, “Chiral surface plasmon polaritons on metallic nanowires,” *Physical Review Letters*, vol. 107, p. 096801, 2011.
- [166] L. J. Sherry, S. H. Chang, R. P. Van Duyne, G. C. Schatz, B. J. Wiley, and Y. N. Xia, “Localized surface plasmon resonance spectroscopy of single silver nanocubes,” *Nano Letters*, vol. 5, no. 10, pp. 2034–2038, 2005.



- [167] C. Sonnichsen, T. Franzl, T. Wilk, G. von Plessen, and J. Feldmann, “Plasmon resonances in large noble-metal clusters,” *New Journal of Physics*, vol. 4, 2002.
- [168] A. Brioude, X. C. Jiang, and M. P. Pileni, “Optical properties of gold nanorods: Dda simulations supported by experiments,” *Journal of Physical Chemistry B*, vol. 109, no. 27, pp. 13138–13142, 2005.
- [169] Z. Fang, L. Fan, C. Lin, D. Zhang, A. J. Meixner, and X. Zhu, “Plasmonic coupling of bow tie antennas with ag nanowire,” *Nano Letters*, vol. 11, no. 4, pp. 1676–1680, 2011.
- [170] J. A. Hutchison, S. P. Centeno, H. Odaka, H. Fukumura, J. Hofkens, and H. Uji-i, “Subdiffraction limited, remote excitation of surface enhanced raman scattering,” *Nano Letters*, vol. 9, no. 3, pp. 995–1001, 2009.
- [171] Y. Fang, H. Wei, F. Hao, P. Nordlander, and H. X. Xu, “Remote-excitation surface-enhanced raman scattering using propagating ag nanowire plasmons,” *Nano Letters*, vol. 9, no. 5, pp. 2049–2053, 2009.
- [172] J. R. Krenn, B. Lamprecht, H. Ditlbacher, G. Schider, M. Salerno, A. Leitner, and F. R. Aussenegg, “Non-diffraction-limited light transport by gold nanowires,” *Europhysics Letters*, vol. 60, no. 5, p. 663, 2002.
- [173] J. R. Krenn and J.-C. Weeber, “Surface plasmon polaritons in metal stripes and wires,” *Philosophical Transactions of the Royal Society of London A*, vol. 362, no. 1817, pp. 739–756, 2004.

- [174] Z. Jacob and V. M. Shalaev, “Plasmonics goes quantum,” *Science*, vol. 334, no. 6055, pp. 463–464, 2011.
- [175] R. Kolesov, B. Grotz, G. Balasubramanian, R. J. Stohr, A. A. L. Nicolet, P. R. Hemmer, F. Jelezko, and J. Wrachtrup, “Wave-particle duality of single surface plasmon polaritons,” *Nature Physics*, vol. 5, no. 7, pp. 470–474, 2009.
- [176] S. Fasel, F. Robin, E. Moreno, D. Erni, N. Gisin, and H. Zbinden, “Energy-time entanglement preservation in plasmon-assisted light transmission,” *Physical Review Letters*, vol. 94, no. 11, p. 110501, 2005.
- [177] A. Huck, S. Smolka, P. Lodahl, A. S. Sorensen, A. Boltasseva, J. Janousek, and U. L. Andersen, “Demonstration of quadrature-squeezed surface plasmons in a gold waveguide,” *Physical Review Letters*, vol. 102, no. 24, 2009.
- [178] D. E. Chang, A. S. Sorensen, E. A. Demler, and M. D. Lukin, “A single-photon transistor using nanoscale surface plasmons,” *Nature Physics*, vol. 3, no. 11, pp. 807–812, 2007.
- [179] G. Bracher, K. Schraml, C. Jakubeit, M. Kaniber, and J. J. Finley, “Direct measurement of plasmon propagation lengths on lithographically defined metallic waveguides on GaAs,” *Journal of Applied Physics*, vol. 110, no. 12, p. 123106, 2011.
- [180] M. Allione, V. V. Temnov, Y. Fedutik, U. Woggon, and M. V. Artemyev, “Sur-

- face plasmon mediated interference phenomena in low-q silver nanowire cavities,” *Nano Letters*, vol. 8, no. 1, pp. 31–35, 2008.
- [181] C. Rewitz, T. Keitzl, P. Tuchscherer, S. Goetz, P. Geisler, G. Razinskas, B. Hecht, and T. Brixner, “Spectral-interference microscopy for characterization of functional plasmonic elements,” *Opt. Express*, vol. 20, no. 13, p. 14632, 2011.
- [182] H. Wei, Z. P. Li, X. R. Tian, Z. X. Wang, F. Z. Cong, N. Liu, S. P. Zhang, P. Nordlander, N. J. Halas, and H. X. Xu, “Quantum dot-based local field imaging reveals plasmon-based interferometric logic in silver nanowire networks,” *Nano Letters*, vol. 11, no. 2, pp. 471–475, 2011.
- [183] A. Hohenau, P. Kusar, C. Gruber, and J. R. Krenn, “Analysis of damping-induced phase flips of plasmonic nanowire modes,” *Opt. Lett.*, vol. 37, no. 4, p. 746, 2012.
- [184] S. Coskun, B. Aksoy, and H. E. Unalan, “Polyol synthesis of silver nanowires: An extensive parametric study,” *Crystal Growth and Design*, vol. 11, no. 11, pp. 4963–4969, 2011.
- [185] D. E. Chang, A. S. Sorensen, P. R. Hemmer, and M. D. Lukin, “Quantum optics with surface plasmons,” *Physical Review Letters*, vol. 97, no. 5, 2006.
- [186] R. F. Oulton, G. Bartal, D. F. P. Pile, and X. Zhang, “Confinement and propagation characteristics of subwavelength plasmonic modes,” *New Journal of*

- Physics*, vol. 10, no. 10, p. 105018, 2008.
- [187] J. A. Schuller, E. S. Barnard, W. Cai, Y. C. Jun, J. S. White, and M. L. Brongersma, “Plasmonics for extreme light concentration and manipulation,” *Nat Mater*, vol. 9, no. 3, pp. 193–204, 2010.
- [188] D. K. Gramotnev and S. I. Bozhevolnyi, “Plasmonics beyond the diffraction limit,” *Nat Photon*, vol. 4, no. 2, pp. 83–91, 2010.
- [189] J. Dorfmueller, R. Vogelgesang, R. T. Weitz, C. Rockstuhl, C. Etrich, T. Pertsch, F. Lederer, and K. Kern, “Fabry-perot resonances in one-dimensional plasmonic nanostructures,” *Nano Letters*, vol. 9, no. 6, pp. 2372–2377, 2009.
- [190] H. Raether, *Surface Plasmons on Smooth and Rough Surfaces and on Gratings*. Tracts in Modern Physics, New York: Springer, 1988.
- [191] P. Berini and I. De Leon, “Surface plasmon-polariton amplifiers and lasers,” *Nat Photon*, vol. 6, no. 1, pp. 16–24, 2012.
- [192] J. Grandidier, G. C. des Francs, S. Massenot, A. Bouhelier, L. Markey, J.-C. Weeber, C. Finot, and A. Dereux, “Gain-assisted propagation in a plasmonic waveguide at telecom wavelength,” *Nano Letters*, vol. 9, no. 8, pp. 2935–2939, 2009.
- [193] M. C. Gather, K. Meerholz, N. Danz, and K. Leosson, “Net optical gain in a plasmonic waveguide embedded in a fluorescent polymer,” *Nature Photonics*,

- vol. 4, no. 7, pp. 457–461, 2010.
- [194] J. Seidel, S. Grafstrm, and L. Eng, “Stimulated emission of surface plasmons at the interface between a silver film and an optically pumped dye solution,” *Physical Review Letters*, vol. 94, no. 17, p. 177401, 2005.
- [195] M. Ambati, S. H. Nam, E. Ulin-Avila, D. A. Genov, G. Bartal, and X. Zhang, “Observation of stimulated emission of surface plasmon polaritons,” *Nano Letters*, vol. 8, no. 11, pp. 3998–4001, 2008.
- [196] R. F. Oulton, V. J. Sorger, T. Zentgraf, R.-M. Ma, C. Gladden, L. Dai, G. Bartal, and X. Zhang, “Plasmon lasers at deep subwavelength scale,” *Nature*, vol. 461, no. 7264, pp. 629–632, 2009.
- [197] M. A. Noginov, G. Zhu, A. M. Belgrave, R. Bakker, V. M. Shalaev, E. E. Narimanov, S. Stout, E. Herz, T. Suteewong, and U. Wiesner, “Demonstration of a spaser-based nanolaser,” *Nature*, vol. 460, no. 7259, pp. 1110–1112, 2009.
- [198] J. Y. Suh, C. H. Kim, W. Zhou, M. D. Huntington, D. T. Co, M. R. Wasielewski, and T. W. Odom, “Plasmonic bowtie nanolaser arrays,” *Nano Letters*, vol. 12, no. 11, pp. 5769–5774, 2012.
- [199] D. A. Boyd, J. R. Adleman, D. G. Goodwin, and D. Psaltis, “Chemical separations by bubble-assisted interphase mass-transfer,” *Analytical Chemistry*, vol. 80, no. 7, pp. 2452–2456, 2008.

- [200] G. Baffou, R. Quidant, and F. J. G. de Abajo, “Nanoscale control of optical heating in complex plasmonic systems,” *Acs Nano*, vol. 4, no. 2, pp. 709–716, 2010.
- [201] J. R. Adleman, D. A. Boyd, D. G. Goodwin, and D. Psaltis, “Heterogenous catalysis mediated by plasmon heating,” *Nano Letters*, vol. 9, no. 12, pp. 4417–4423, 2009.
- [202] A. S. Urban, M. Fedoruk, M. R. Horton, J. Radler, F. D. Stefani, and J. Feldmann, “Controlled nanometric phase transitions of phospholipid membranes by plasmonic heating of single gold nanoparticles,” *Nano Letters*, vol. 9, no. 8, pp. 2903–2908, 2009.
- [203] D. R. Ward, D. A. Corley, J. M. Tour, and D. Natelson, “Vibrational and electronic heating in nanoscale junctions,” *Nature Nanotechnology*, vol. 6, no. 1, pp. 33–38, 2011.
- [204] N. C. Dang, C. A. Bolme, D. S. Moore, and S. D. McGrane, “Femtosecond stimulated raman scattering picosecond molecular thermometry in condensed phases,” *Physical Review Letters*, vol. 107, no. 4, 2011.
- [205] M. Oron-Carl and R. Krupke, “Raman spectroscopic evidence for hot-phonon generation in electrically biased carbon nanotubes,” *Physical Review Letters*, vol. 100, no. 12, 2008.

- [206] P. Christopher, H. L. Xin, and S. Linic, “Visible-light-enhanced catalytic oxidation reactions on plasmonic silver nanostructures,” *Nature Chemistry*, vol. 3, no. 6, pp. 467–472, 2011.
- [207] D. A. Boyd, L. Greengard, M. Brongersma, M. Y. El-Naggar, and D. G. Goodwin, “Plasmon-assisted chemical vapor deposition,” *Nano Letters*, vol. 6, no. 11, pp. 2592–2597, 2006.
- [208] C. Li, Z. Wang, P. I. Wang, Y. Peles, N. Koratkar, and G. P. Peterson, “Nanostructured copper interfaces for enhanced boiling,” *Small*, vol. 4, no. 8, pp. 1084–1088, 2008.
- [209] S. Ibrahimkutty, J. Kim, M. Cammarata, F. Ewald, J. Choi, H. Ihee, and A. Plech, “Ultrafast structural dynamics of the photocleavage of protein hybrid nanoparticles,” *Acs Nano*, vol. 5, no. 5, pp. 3788–3794, 2011.
- [210] J. Lee, A. O. Govorov, and N. A. Kotov, “Nanoparticle assemblies with molecular springs: A nanoscale thermometer,” *Angewandte Chemie-international Edition*, vol. 44, no. 45, pp. 7439–7442, 2005.
- [211] Z. Z. J. Lim, J. E. J. Li, C. T. Ng, L. Y. L. Yung, and B. H. Bay, “Gold nanoparticles in cancer therapy,” *Acta Pharmacologica Sinica*, vol. 32, no. 8, pp. 983–990, 2011.
- [212] G. von Maltzahn, J. H. Park, K. Y. Lin, N. Singh, C. Schwoppe, R. Mesters, W. E. Berdel, E. Ruoslahti, M. J. Sailor, and S. N. Bhatia, “Nanoparticles that

- communicate in vivo to amplify tumour targeting,” *Nature Materials*, vol. 10, no. 7, pp. 545–552, 2011.
- [213] F. Huth, M. Schnell, J. Wittborn, N. Ocelic, and R. Hillenbrand, “Infrared-spectroscopic nanoimaging with a thermal source,” *Nature Materials*, vol. 10, no. 5, pp. 352–356, 2011.
- [214] H. H. Richardson, M. T. Carlson, P. J. Tandler, P. Hernandez, and A. O. Govorov, “Experimental and theoretical studies of light-to-heat conversion and collective heating effects in metal nanoparticle solutions,” *Nano Letters*, vol. 9, no. 3, pp. 1139–1146, 2009.
- [215] H. H. Richardson, Z. N. Hickman, A. O. Govorov, A. C. Thomas, W. Zhang, and M. E. Kordesch, “Thermooptical properties of gold nanoparticles embedded in ice: Characterization of heat generation and melting,” *Nano Letters*, vol. 6, no. 4, pp. 783–788, 2006.
- [216] D. Erickson, D. Sinton, and D. Psaltis, “Optofluidics for energy applications,” *Nature Photonics*, vol. 5, p. 8, 2011.
- [217] J. A. Schuller, T. Taubner, and M. L. Brongersma, “Optical antenna thermal emitters,” *Nature Photonics*, vol. 3, no. 11, pp. 658–661, 2009.
- [218] C. Sonnichsen, S. Geier, N. E. Hecker, G. von Plessen, J. Feldmann, H. Ditlbacher, B. Lamprecht, J. R. Krenn, F. R. Aussenegg, V. Z. H. Chan, J. P.



- Spatz, and M. Moller, "Spectroscopy of single metallic nanoparticles using total internal reflection microscopy," *Applied Physics Letters*, vol. 77, no. 19, pp. 2949–2951, 2000.
- [219] L. J. E. Anderson, K. M. Mayer, R. D. Fraleigh, Y. Yang, S. Lee, and J. H. Hafner, "Quantitative measurements of individual gold nanoparticle scattering cross sections," *Journal of Physical Chemistry C*, vol. 114, no. 25, pp. 11127–11132, 2010.
- [220] C. M. Galloway, E. C. Le Ru, and P. G. Etchegoin, "Single-molecule vibrational pumping in sers," *Physical Chemistry Chemical Physics*, vol. 11, no. 34, pp. 7372–7380, 2009.
- [221] P. K. Jain and M. A. El-Sayed, "Noble metal nanoparticle pairs: Effect of medium for enhanced nanosensing," *Nano Letters*, vol. 8, no. 12, pp. 4347–4352, 2008.
- [222] M. M. Miller and A. A. Lazarides, "Sensitivity of metal nanoparticle surface plasmon resonance to the dielectric environment," *Journal Of Physical Chemistry B*, vol. 109, no. 46, pp. 21556–21565, 2005.
- [223] J. B. Lassiter, H. Sobhani, J. A. Fan, J. Kundu, F. Capasso, P. Nordlander, and N. J. Halas, "Fano resonances in plasmonic nanoclusters: Geometrical and chemical tunability," *Nano Letters*, vol. 10, no. 8, pp. 3184–3189, 2010.

- [224] E. Prodan and P. Nordlander, “Plasmon hybridization in spherical nanoparticles,” *Journal of Chemical Physics*, vol. 120, no. 11, pp. 5444–5454, 2004.
- [225] D. E. Aspnes, “Local-field effects and effective-medium theory - a microscopic perspective,” *American Journal of Physics*, vol. 50, no. 8, pp. 704–709, 1982.
- [226] Y. Rao, J. M. Qu, T. Marinis, and C. P. Wong, “A precise numerical prediction of effective dielectric constant for polymer-ceramic composite based on effective-medium theory,” *Ieee Transactions on Components and Packaging Technologies*, vol. 23, no. 4, pp. 680–683, 2000.
- [227] K. Lichtenecker and K. Rother, “The derivation of the logarithmic compound law from general principles of the stationary current.,” *Physikalische Zeitschrift*, vol. 32, pp. 255–260, 1931.
- [228] G. A. Niklasson, C. G. Granqvist, and O. Hunderi, “Effective medium models for the optical-properties of inhomogeneous materials,” *Applied Optics*, vol. 20, no. 1, pp. 26–30, 1981.
- [229] J. E. Spanier and I. P. Herman, “Use of hybrid phenomenological and statistical effective-medium theories of dielectric functions to model the infrared reflectance of porous sic films,” *Physical Review B*, vol. 61, no. 15, pp. 10437–10450, 2000.
- [230] V. Myroshnychenko and C. Brosseau, “Effective complex permittivity and continuum percolation analysis of two-phase composite media,” *Ieee Transactions*

*on Dielectrics and Electrical Insulation*, vol. 16, no. 4, pp. 1209–1222, 2009.

- [231] A. H. Harvey, J. S. Gallagher, and J. M. H. L. Sengers, “Revised formulation for the refractive index of water and steam as a function of wavelength, temperature and density,” *Journal of Physical and Chemical Reference Data*, vol. 27, no. 4, pp. 761–774, 1998.
- [232] NIST, “The surface tension of the liquid water-water vapor interface at saturation pressure.” <http://chemweb.calpoly.edu/jhagen/446%20handout%204%20water%20surface%20tension.pdf>.
- [233] O. M. Wilson, X. Y. Hu, D. G. Cahill, and P. V. Braun, “Colloidal metal particles as probes of nanoscale thermal transport in fluids,” *Physical Review B*, vol. 66, no. 22, 2002.
- [234] B. Luk’yanchuk, N. I. Zheludev, S. A. Maier, N. J. Halas, P. Nordlander, H. Giessen, and C. T. Chong, “The fano resonance in plasmonic nanostructures and metamaterials,” *Nature Mater.*, vol. 9, pp. 707–715, 2010.
- [235] D. Dregely, M. Hentschel, and H. Giessen, “Excitation and tuning of higher-order fano resonances in plasmonic oligomer clusters,” *ACS Nano*, vol. 5, no. 10, pp. 8202–8211, 2011.
- [236] M. Hentschel, M. Saliba, R. Vogelgesang, H. Giessen, A. P. Alivisatos, and N. Liu, “Transition from isolated to collective modes in plasmonic oligomers,” *Nano Lett.*, vol. 10, no. 7, pp. 2721–2726, 2010.

- [237] J. Ye, F. Wen, H. Sobhani, J. B. Lassiter, P. V. Dorpe, P. Nordlander, and N. J. Halas, “Plasmonic nanoclusters: near field properties of the fano resonance interrogated with sers,” *Nano Lett.*, vol. 12, no. 3, pp. 1660–1667, 2012.
- [238] H. Liu, G. X. Li, K. F. Li, S. M. Chen, S. N. Zhu, C. T. Chan, and K. W. Cheah, “Linear and nonlinear fano resonance on two-dimensional magnetic metamaterials,” *Phys. Rev. B*, vol. 84, p. 235437, 2011.
- [239] M. W. Klein, C. Enkrich, M. Wegener, and S. Linden, “Second-harmonic generation from magnetic metamaterials,” *Science*, vol. 313, no. 5786, pp. 502–504, 2006.
- [240] R. W. Boyd, *Nonlinear optics*. Boston: Academic Press, 3rd ed., 2008.
- [241] T. Ellenbogen, N. Voloch-Bloch, A. Ganany-Padowicz, and A. Arie, “Nonlinear generation and manipulation of airy beams,” *Nature Photon.*, vol. 3, pp. 395–398, 2009.
- [242] B. Corcoran, C. Monat, C. Grillet, D. J. Moss, B. J. Eggleton, T. P. White, L. O’Faolain, and T. F. Krauss, “Green light emission in silicon through slow-light enhanced third-harmonic generation in photonic-crystal waveguides,” *Nature Photon.*, vol. 3, pp. 206–210, 2009.
- [243] N. K. Grady, M. W. Knight, R. Bardhan, and N. J. Halas, “Optically-driven collapse of a plasmonic nanogap self-monitored by optical frequency mixing,” *Nano Lett.*, vol. 10, no. 4, pp. 1522–1528, 2010.

- [244] P. Genevet, J.-P. Tetienne, E. Gatzogiannis, R. Blanchard, M. A. Kats, M. O. Scully, and F. Capasso, “Large enhancement of nonlinear optical phenomena by plasmonic nanocavity gratings,” *Nano Lett.*, vol. 10, pp. 4880–4883, 2010.
- [245] H. Harutyunyan, G. Volpe, R. Quidant, and L. Novotny, “Enhancing the nonlinear optical response using multifrequency gold-nanowire antennas,” *Phys. Rev. Lett.*, vol. 108, p. 217403, 2012.
- [246] A. V. Oppenheim, R. W. Schaffer, and J. R. Buck, *Discrete-time signal processing*. Upper Saddle River: Prentice-Hall, 2nd ed., 1998.
- [247] R. A. Farrer, F. L. Butterfield, V. W. Chen, and J. T. Fourkas, “Highly efficient multiphoton-absorption-induced luminescence from gold nanoparticles,” *Nano Lett.*, vol. 5, no. 6, pp. 1139–1142, 2005.
- [248] M. Pelton, M. Liu, S. Park, N. F. Scherer, and P. Guyot-Sionnest, “Ultrafast resonant optical scattering from single gold nanorods: Large nonlinearities and plasmon saturation,” *Phys. Rev. B*, vol. 73, p. 155419, 2006.
- [249] T. Gu, N. Petrone, J. F. McMillan, A. v. d. Zande, M. Yu, G. Q. Lo, D. L. Kwong, J. Hone, and C. W. Wong, “Regenerative oscillation and four-wave mixing in graphene optoelectronics,” *Nature Photon.*, vol. 6, pp. 554–559, 2012.
- [250] R. Ganeev, I. Kulagin, A. Ryasnyansky, R. Tugushev, and T. Usmanov, “Characterization of nonlinear optical parameters of kdp, linbo3 and bbo crystals,” *Opt. Commun.*, vol. 229, pp. 403–412, 2004.

- [251] R. d. Coso, J. Requejo-Isidro, J. G. J. Solis, and C. N. Afonso, “Third order nonlinear optical susceptibility of cu:al<sub>2</sub>o<sub>3</sub> nanocomposites: From spherical nanoparticles to the percolation threshold,” *J. Appl. Phys.*, vol. 95, pp. 2755–2762, 2004.
- [252] E. Xenogiannopoulou, K. Iliopoulos, S. Couris, T. Karakouz, A. Vaskevich, and I. Rubinstein, “Third-order nonlinear optical response of gold-island films,” *Adv. Funct. Mater.*, vol. 18, pp. 1281–1289, 2008.
- [253] H. A. Garcia, G. B. Correia, R. J. d. Oliveira, A. Galembeck, and C. B. d. Arajo, “Third- and fifth-order susceptibilities of cobalt oxide nanoparticles dispersed in n-heptane,” *J. Opt. Soc. Am. B*, vol. 29, no. 7, pp. 1613–1617, 2012.
- [254] J. B. Monteiro-Filho and L. A. Gmez-Malagn, “Resonant third order nonlinear optical susceptibility of gold nanoparticles,” *J. Opt. Soc. Am. B*, vol. 29, no. 7, pp. 1793–1798, 2012.
- [255] J. Renger, R. Quidant, N. v. Hulst, and L. Novotny, “Surface-enhanced nonlinear four-wave mixing,” *Phys. Rev. Lett.*, vol. 104, p. 046803, 2010.
- [256] S. Palomba and L. Novotny, “Nonlinear excitation of surface plasmon polaritons by four-wave mixing,” *Phys. Rev. Lett.*, vol. 101, p. 056802, 2008.
- [257] J. Renger, R. Quidant, N. v. Hulst, S. Palomba, and L. Novotny, “Free-space excitation of propagating surface plasmon polaritons by nonlinear four-wave mixing,” *Phys. Rev. Lett.*, vol. 103, p. 266802, 2009.

- [258] M. Danckwerts and L. Novotny, “Optical frequency mixing at coupled gold nanoparticles,” *Phys. Rev. Lett.*, vol. 98, p. 026104, 2007.